

Evaluating the Machinability of Titanium Alloys, Timetal 407 and Ti-6Al-4V

Christopher Dredge

Department of Materials Science and Engineering

The University of Sheffield



Thesis submitted for the degree of Doctor of Engineering

January 2021

Abstract

An industry focussed research project has been undertaken to evaluate the machinability of an emerging titanium alloy, Timetal 407 and offer a fundamental understanding for the chip control issues. This research identified two key stages in the life cycle of a titanium alloy where consideration of the machinability would provide economic opportunities for the aerospace manufacturing sector. First in the development of emerging alloys and secondly in optimising the cutting parameters during the machining of aerospace components.

To assess machinability in the developmental stage of an emerging alloy, a series of small scale experiments were utilised to assess the machinability outputs for Timetal 407 and Ti-6Al-4V, with the aim of drawing conclusions about each of the alloys limitations and strengths in regards to key machinability characteristics; tool wear, chip control, subsurface deformation and cutting forces. The key to these tests was to remain low cost, offering a quick turnaround of results relative to high speed machining, in order to filter out a large number of alloy chemistries and microstructural combinations.

For the second stage, *machinability maps* for Timetal 407 and Ti-6Al-4V were developed using data from high speed machining operations which determined for a range of cutting parameters (cutting speed and feed rate) where machinability outputs were acceptable and Material Removal Rate (MRR) was maximised. The *machinability map* again incorporated the key machinability characteristics: tool wear, chip control and subsurface deformation as primary points of consideration on the map, with cutting force as a secondary consideration. The map also identified a region of cutting parameters where improved chip management of Timetal 407 could be achieved. Using the high speed machining and small scale machinability experiments, mechanical twins and thermoplastic instability were identified as key determinants for chip control.

The outcomes of this research were an ability to characterise machinability using a small scale experimental framework, as well as fulfilling the industry requirements through improving chip management. The improvement of chip management had a number of concurrent benefits to manufacturing operations of large structural gas turbine engine components through reducing cutting time by 43% between Ti-6Al-4V and Timetal 407, whilst also reducing cleaning downtime between parts and reducing machine maintenance to fix issues with chip swarf conveyors. The risk of component rework due to tool breakage or surface finish defects have been reduced, offering potential savings of 300 minutes per part for 'on machine' rework, or 480 minutes per part for 'hand dressing' by an operator. Due to these operational improvements, the flow of parts through manufacturing facilities has been improved, reducing inventory stock and work in progress.

Acknowledgements

I would like to thank Prof. Martin Jackson for his help and guidance throughout the course of this research. I would also like to thank Dr. Sabino Ayvar-Soberanis (AMRC), Dr. Rachid M'saoubi (Seco Tools), Dr. Jamie McGourlay (Rolls-Royce), Dr. Andrew Mantle (Rolls-Royce), Josh Weston (Formally of Rolls-Royce), Iain Berment-Parr (Timet UK) and Dr Matthew Thomas (Formally of Timet UK) for their technical input into the project and expert knowledge.

I would also like to thank my family and friends whose help and support has helped me throughout the last few years.

Publications

Thesis chapters 3 and 4 have been previously published as the following publications:

[1] C. Dredge, R. M'Saoubi, B. Thomas, O. Hatt, M. Thomas, M. Jackson. 'A low cost machinability assessment to accelerate titanium alloy development'. In: Proceedings of the Institution of Mechanical Engineers, Part B: Journal of Engineering Manufacture, (2020)

[2] C. Dredge, I. Berment-Parr, R. M'Saoubi, M. Jackson. 'Machinability maps- Towards a mechanistic understanding of the machining of Ti-6Al-4V and Timetal 407' In: Advances in Industrial and Manufacturing Engineering, (2020)

Contents

<i>Abstract</i>	i
<i>Acknowledgements</i>	ii
<i>Publications</i>	iii
<i>Table of Contents</i>	iv
<i>List of Figures</i>	vii
<i>List of Tables</i>	xii
<i>Nomenclature</i>	xiv
1. Introduction	1
1.1 Thesis Motivation	2
1.2 Thesis Outline	3
References	4
2. Literature Review	6
2.1 Titanium Alloy Classification	6
2.1.1 α Alloys	9
2.1.2 Near α Alloys	9
2.1.3 $\alpha+\beta$ Alloys	9
2.1.4 Metastable β Alloys	10
2.1.5 β Alloys	10
2.2 Deformation Modes	10
2.2.1 Slip	11
2.2.2 Twins	12
2.2.2.1 <i>Texture Evolution</i>	13
2.2.2.2 <i>Work Hardening Behaviour</i>	13
2.2.2.3 <i>Grain Size Effect</i>	14
2.2.2.4 <i>Stacking Fault Energy</i>	14
2.2.2.5 <i>Effect of Aluminium on Deformation Twins</i>	15
2.3 Titanium Alloy Microstructure	15
2.3.1 Microstructure Types	16
2.3.2 Titanium Annealing Process	17
2.3.2.1 <i>Mill Annealing</i>	17
2.3.2.2 <i>Duplex Annealing</i>	17
2.3.2.3 <i>Recrystallisation</i>	17
2.3.2.4 <i>β Annealing</i>	17
2.3.2.5 <i>Solution Treatment and Age</i>	18
2.3.3 Microstructural Effects on Machining	18
2.3.4 Microstructural Effects on Twinning	19
2.4 Machining Titanium Alloys	19
2.4.1 Principles of Metal Cutting	19
2.4.2 Machinability	20
2.4.2.1 <i>Tool Life</i>	21
2.4.2.2 <i>Cutting Forces</i>	23
2.4.2.3 <i>Surface Integrity</i>	24
2.4.2.4 <i>Chip Formation</i>	25
2.5 Small Scale Machining Characteristics Techniques	26
2.6 Timetal 407	27
2.7 Summary	28
2.8 Experimental Methods and Analysis Techniques	29
2.8.1 Arbitrary Strain Path	29

2.8.2 Thermomechanical Compression Machine	30
2.8.3 Diffusion Couple Experiment	30
2.8.4 Finite Element Modelling	31
2.8.5 Specimen Preparation	31
2.8.6 Imaging and Analysis	32
2.8.6.1 Microstructure Optical Imaging	32
2.8.6.2 Scanning Electron Microscope (SEM) and X-EDS	32
2.8.6.3 Electron Backscatter Diffraction (EBSD)	32
References	33
3. A low Cost Machinability Approach to Accelerate Titanium Alloy Development	43
3.1 Introduction	43
3.2 Methodology	45
3.2.1 Small Scale Orthogonal Cutting	45
3.2.2 Diffusion Couple Experiment	47
3.2.3 Large Scale Turning Trials	48
3.3 Results and Discussion	50
3.3.1 Chip Formation	50
3.3.1.1 Uniaxial Compression- Analysis of the Deformation Characteristics for Ti-64 and Ti-407	50
3.3.1.2 Comparison of Ti-64 and Ti-407 Propensity for Mechanical Twinning	52
3.3.1.3 FE Model- Development of the FE Model to predict the Chip Formation of Titanium Alloys in each Microstructural Condition	53
3.3.1.4 Small Scale Cutting Experiments- Comparison of Chip Form for Ti-64 and Ti-407	56
3.3.1.5 Large Scale Turning Trials- Analysis of Chip Form for Ti-64 and Ti-407	58
3.3.2 Subsurface Deformation Characteristics for Small Scale Cutting and Large Scale Turning Trials	59
3.3.3 Comparison of the Cutting Forces for Small Scale Cutting and Large Scale Turning Trials	61
3.3.4 Tool Wear Analysis for Ti-64 and Ti-407 using Diffusion Couple Experiments, Small Scale Cutting and Large Scale Turning Trials	62
3.3.5 Contextualisation of the Small Scale Machinability Approach	64
3.4 Conclusions	66
References	67
4. Machinability Maps – Towards a Mechanistic Understanding of the Machining of Ti-6Al-4V and Timetal 407	71
4.1 Introduction	71
4.2 Methodology	73
4.2.1 Material Preparation	73
4.2.2 Machining Trials	74
4.2.3 Subsurface Deformation	75
4.2.4 Tool Wear	75
4.2.5 Chip Analysis	76
4.2.6 Development of the Machinability Map	76
4.3 Results	77
4.3.1 Section 1: Experimental Results	77
4.3.1.1 Comparison of subsurface mechanical twinning	77
4.3.1.2 Comparison of microstructural subsurface deformation	78

4.3.1.3 <i>Comparison of Tool Flank Wear</i>	80
4.3.1.4 <i>Comparison of chip morphology</i>	82
4.3.1.5 <i>Comparison of chip serration characteristics</i>	83
4.3.1.6 <i>Comparison of chip shear band characteristics</i>	85
4.3.2 Section 2: Machinability Maps	87
4.4 Discussion	91
4.4.1 Machinability Maps	91
4.4.2 Ti-407 Chip Control	91
4.5 Conclusion	93
References	94
5. Validation of Machinability Maps	100
5.1 Introduction	100
5.2 Methodology	101
5.2.1 Pre-Processing of Billet Material	101
5.2.2 Experimental Setup	103
5.3 Experimental Results	104
5.3.1 Investigating the Strain Rate Effects on the Machinability Map	104
5.3.2 Validating the Machinability Map at a Depth of Cut of 0.3 mm	110
5.3.3 Industrial Outputs of this Work	114
5.4 Conclusion	115
References	116
6. Summary and Future Work	118
6.1 Summary	118
6.2 Future Work	121

List of Figures

1. Introduction

- Figure 1.1** Half cross-section of “The Jet Engine, Rolls-Royce plc” colour coded with respect to the materials used for the main components. Modified from Anvari [3]. 1

2. Literature Review

- Figure 2.1** Crystal structures of alpha and beta phases of titanium. From ref [1]. 6
- Figure 2.2** The Burgers orientation relationship between the α (HCP) and the β (BCC) titanium alloy phases, showing $(0001)_\alpha // (101)_\beta$, $[11\bar{2}0]_\alpha // [11\bar{1}]_\beta$ and the relationship between HCP $\langle a \rangle$ type directions and the equivalent BCC directions adapted from [7]. 7
- Figure 2.3** Pseudo-binary titanium phase diagram. Redrawn from [11]. 8
- Figure 2.4** Schematic of a deformation twin causing rotation of the crystallographic lattice 12
- Figure 2.5** Plot showing the three stages of the normalised strain hardening rate against strain curve 14
- Figure 2.6** Effect of cooling rate from the β phase on the lamellar microstructure of Ti-6242. a) 1 °C/min b) 100 °C/min [50] 16
- Figure 2.7** Force diagram showing the relationship between component forces in the orthogonal cutting environment. Redrawn from [67]. 20
- Figure 2.8** Bar chart showing the relative machinability ratings for titanium alloys against B1112. 21
- Figure 2.9** Tool life curve based on the typical flank wear rate over time. 22
- Figure 2.10** Schematic illustration of a serrated chip formation. Redrawn from [114]. Alongside the schematic is an in-situ image showing the formation of the primary shear band [115]. 26
- Figure 2.11** Image showing the Arbitrary Strain Path (ASP) used for the small scale orthogonal cutting tests. 29
- Figure 2.12** a) An image of the Thermomechanical Compression (TMC) machine used during compression testing and b) image of the robot arms holding the compression sample prior to testing. 30
- Figure 2.13** An image of the diffusion couple rig used for the diffusion couple experiment. 30

3. A low Cost Machinability Approach to Accelerate Titanium Alloy Development

- Figure 3.1** Plot showing the combinations of the Johnson-Cook strain hardening parameters, B and n along with the associated chip morphologies from finite 44

element models reported in the literature.

- Figure 3.2** a) Photograph of the ASP rig used for the small scale cutting experiments, b) 3D model of the tool holder designed and developed using Autodesk and c) a photograph showing the negative 6° rake angle between the workpiece and the cutting insert. 46
- Figure 3.3** Micrographs of the titanium alloy test pieces used in this work post heat treatment, a) Ti-64 MA, b) Ti-407 STA Air Cooled, c) Ti-407 STA Oil Quenched and d) Ti-407 STA Water Quenched. 47
- Figure 3.4** a) Location of and geometry of the test samples used for the small scale orthogonal cutting tests and b) a photograph of the sample used for the small scale orthogonal cutting test. 47
- Figure 3.5** Photograph showing the setup for the industrial machining trials. Using a disk of material held inside a CNC machining centre; the cutting insert held into a dynamometer to record the cutting forces and the coolant provided through an external pipe. 49
- Figure 3.6** a) 3D CAD illustration of the workpiece after grooving the disk to form a 4 mm wide ring for orthogonal machining trials, b) Photograph of the 4 mm wide ring for orthogonal cutting trials and c) photograph of the modified tool holder, Wire EDM'd to meet the requirements for orthogonal machining. 49
- Figure 3.7** Flow stress curves produced from the uniaxial compression tests at strain rates of a) 0.1 s^{-1} , b) 1.0 s^{-1} and c) 10 s^{-1} . 51
- Figure 3.8** Map of photographs showing the cross-section of the titanium alloys, from a strain rate of $0.1 - 100 \text{ s}^{-1}$, after testing has been completed. 51
- Figure 3.9** Curve of normalised strain hardening rate against true strain, calculated from flow stress data, which was determined from compression tests of Ti-64 and Ti-407 at a strain rate of 1.0 s^{-1} . 52
- Figure 3.10** DEFORMTM compression simulations showing the effective strain across the cross section of the test pieces at the point of fracture at a strain rate of 0.1 s^{-1} . The material data used is as shown in Table 3.2. a) Ti-64 MA, b) Ti-407 STA Air Cooled, c) Ti-407 STA Oil Quenched and d) Ti-407 STA Water Quenched. 54
- Figure 3.11** DEFORMTM orthogonal 2D simulations showing the chip forming characteristics for each of the corresponding alloys based on material data modelled in the DEFORMTM compression simulations at a cutting speed of 6.0 m.min^{-1} . a) Ti-64 MA, b) Ti-407 STA Air Cooled, c) Ti-407 STA Oil Quenched and d) Ti-407 STA Water Quenched. 54
- Figure 3.12** Figure of DEFORMTM 2D orthogonal cutting simulations showing the cutting forces required to form a chip for a) Ti-64 MA, b) Ti-407 STA Air Cooled, c) Ti-407 STA Oil Quenched, d) Ti-407 STA Water Quenched. 55
- Figure 3.13** In-situ photographs taken with a Nikon D5000 camera of the chip forming process from the small scale orthogonal cutting tests, a) Ti-64 MA, b) Ti-407 STA Air Cooled, c) Ti-407 STA Oil Quenched and d) Ti-407 STA Water Quenched. 56

Figure 3.14	Cross sectional light micrographs of the chip formation from the small scale orthogonal cutting tests for a) Ti-64 MA, b) Ti-407 STA Air Cooled, c) Ti-407 STA Oil Quenched and d) Ti-407 STA Water Quenched.	56
Figure 3.15	Experimental cutting forces measured from the small scale orthogonal cutting for a) Ti-64 MA, b) Ti-407 STA Air Cooled, c) Ti-407 STA Oil Quenched and d) Ti-407 STA Water Quenched.	57
Figure 3.16	Cross sectional light micrographs of the chip formation from the industrial cutting tests for a) Ti-64 MA, b) Ti-407 STA Water Quenched.	58
Figure 3.17	Photographs showing the comparable chip formation at cutting speeds (6, 40, and 70 m.min ⁻¹) from the industrial orthogonal cutting tests of Ti-64 MA and Ti-407 STA Water Quenched. Feed Rate = 0.3 mm.rev ⁻¹ .	58
Figure 3.18	Light micrographs of the depth of subsurface features from the small scale orthogonal cutting tests, a) Ti-64 MA, b) Ti-407 STA Air Cooled, c) Ti-407 STA Oil Quenched and d) Ti-407 STA Water Quenched	59
Figure 3.19	Light micrographs of the depth of the subsurface features from the industrial cutting trials, a) Ti-64 MA and b) Ti-407 STA Water Quenched.	60
Figure 3.20	Bar plot showing the average cutting force in comparison to the cutting speed for the small scale orthogonal cutting tests for Ti-64 MA and Ti-407 STA Water Quenched Cooled.	61
Figure 3.21	Bar plot showing the average cutting force in comparison to the cutting speed for the large scale cutting tests for Ti-64 MA and Ti-407 STA Water Quenched.	61
Figure 3.22	Scanning electron micrographs of the TiC interface between WC-6% Co cutting insert and workpiece material from diffusion couple experiments a) Ti-64 MA, b) Ti-407 STA Air Cooled, c) Ti-407 STA Oil Quenched and d) Ti-407 STA Water Quenched.	62
Figure 3.23	X-EDS analysis showing the titanium, tungsten and carbon across the tool and workpiece, including diffusion bond region. a) Ti-64 MA, b) Ti-407 STA Air Cooled, c) Ti-407 STA Oil Quenched and d) Ti-407 STA Water Quenched.	62
Figure 3.24	Alicona 3D scans of the tools from the small scale orthogonal cutting tests showing the build-up of workpiece material across the edge of the tool for a) Ti-64 MA, b) Ti-407 STA Air Cooled, c) Ti-407 STA Oil Quenched and d) Ti-407 STA Water Quenched.	63
Figure 3.25	Photographs of the flank wear and rake face wear from tool life trials for Ti-64 MA and Ti-407 STA Water Quenched from large scale turning trials at 80 m.min ⁻¹ .	63
Figure 3.26	A schematic showing the suggested order for completion of the small scale tests and modelling to filter out undesirable alloy combinations and conditions.	65

4. Machinability Maps – Towards a Mechanistic Understanding of the Machining of Ti-6Al-4V and Timetal 407

Figure 4.1	Light optical micrographs of the titanium alloys post-heat treatment a) Ti-64	73
-------------------	---	----

(Mill Annealed), b) Ti-407 (Solution Treated and Aged).

- Figure 4.2** a) 3D CAD drawing of the workpiece after grooving the disk with a 4 mm wide ring for orthogonal axial plunge turning trials, b) Photograph of the setup for the orthogonal turning trials. A red box around the tool edge indicates the 4mm wide section of the tool used to perform the orthogonal cutting operation. The red arrow shows the direction of movement of the tool. 74
- Figure 4.3** Light optical micrographs showing the depth of subsurface twins after machining Ti-64 at different cutting speeds and feeds in the orthogonal cutting tests. 77
- Figure 4.4** Light optical micrographs showing the depth of subsurface twins after machining Ti-407 at different cutting speeds and feeds in the orthogonal cutting tests. 78
- Figure 4.5** Following machining, EBSD scans of the subsurface shows imparted deformation in the surface of the Ti-64 (a-c) and Ti-407 (d-f) samples. The black dotted lines represent the maximum depth of SPD. 79
- Figure 4.6** The change in LAGB density vs depth beneath the machined surface a) Ti-64 and b) Ti-407. The labels correlate with the qualitatively measured depth of SPD from Figure 4.5 which provide a visual comparison to the quantitatively measured depth of SPD using the LAGB in this figure. The arrow on the Fig 5d LAGB density line indicates that the depth of SPD extends further than was able to be imaged using EBSD. 80
- Figure 4.7** Photographs of the flank wear after (replicating plunge turning) machining Ti-64 and Ti-407 at the cutting speeds (6, 40 and 70 m.min⁻¹) and at a feed rate of 0.30 mm.rev⁻¹. 81
- Figure 4.8** Flank wear measurements for a) Ti-64 and b) Ti-407. The black dotted line indicates the flank wear boundary condition set for the machinability map. 81
- Figure 4.9** Photographs illustrating the change of Ti-64 chip morphology for a range of cutting speeds and feed rates from the orthogonal cutting tests. 82
- Figure 4.10** Photographs illustrating the change in Ti-407 chip morphology for a range of cutting speeds and feed rates from the orthogonal cutting tests. 83
- Figure 4.11** Cross-sectional light optical micrographs of the chip formation of Ti-64 at a range of cutting speeds and feed rates from the orthogonal cutting tests. 84
- Figure 4.12** Cross-sectional light optical micrographs of the chip formation of Ti-407 at a range of cutting speeds and feed rates from the orthogonal cutting tests. 84
- Figure 4.13** Light optical micrographs of the severely plastically deformed shear band region in the chip of Ti-64 for a range of cutting speeds and feed rates from the orthogonal cutting tests. Filled white arrows indicate the shear band region. The unfilled white arrows point to the mechanical twins which have nucleated around the ASB of the chip. 86
- Figure 4.14** Light optical micrographs of the severely plastically deformed shear band region in the chip of Ti-407 for a range of cutting speeds and feed rates from the orthogonal cutting tests. Filled white arrows indicate the shear band region. 86

The unfilled white arrows point to the mechanical twins which have nucleated around the ASB of the chip.

Figure 4.15 Machinability maps based on three criteria; chip form, tool wear and subsurface features in order to directly determine the relative machinability of a) Ti-64 and b) Ti-407. c) A summary and example of the pass/fail assessment of the three key machinability criteria at four different positions on the machinability maps in a) and b). 88

5. Validation of Machinability Maps

Figure 5.1 Light micrographs of Ti-407, taken from a coupon sectioned from the outer 20 mm of the billet cross section, a) in an as-forged condition, b) after the STA heat treatment. 102

Figure 5.2 a) Light micrograph of Ti-407 at the outer 20 mm of the billet after a STA heat treatment. b) ImageJ contrasting used to ascertain the volume fraction of primary alpha and lamellar within the microstructure of Ti-407. 102

Figure 5.3 Composite image comprising of a quarter cross-section taken of the Ti-407 billet and the corresponding light micrographs at 0°, 45° and 90°. 103

Figure 5.4 Photograph showing the setup for industrial machining trials. Use of a large billet of material held inside a CNC machining centre by chuck and tailstock; the cutting insert and shank held into a Kistler dynamometer to record the cutting forces. The image has been taken after completing all experiments to indicate how the post machining surface analysis samples recorded. 104

Figure 5.5 Machinability map with the three sets of machining parameters (Table 5.1) conducted at a depth of cut of 0.5 mm. The results have been presented below in Table 5.3. 106

Figure 5.6 Shows the machinability map with the four points where machining experiments were conducted at a depth of cut of 0.3 mm. The results have been presented below in Table 5.4. 111

List of Tables

Table 2.1	Slip systems in the HCP α phase [10]	12
Table 2.2	Summary of the metallographic preparation steps for titanium alloys	32
Table 2.3	Summary of the operating parameters used for the SEM	32
Table 3.1	Comparison of the toughness of each titanium alloy, measured as the area under the flow stress curve.	51
Table 3.2	Norton Hoff Model Material Parameters from flow stress curves at a strain rate of 0.1 s^{-1} . C-L Refers to Cockroft-Latham Damage Criterion.	53
Table 3.3	Measured depth of subsurface features including mechanical twins and severe plastic deformation from the small scale orthogonal cutting tests.	59
Table 3.4	Cost comparison for the testing Ti-64 MA and Ti-407 STA Water Quenched for the industrial cutting tests and the small scale tests.	60
Table 4.1	The cutting parameters used in the orthogonal experiments to turn Ti-64 and Ti-407 billet (in Figure 4.2)	75
Table 4.2	Measured depth of subsurface twins within the machined surface of Ti-64 and Ti-407 over the range of cutting parameters.	78
Table 4.3	Measured depth of severe plastic deformation (SPD) within the machined surface of Ti-64 and Ti-407 over the range of cutting parameters.	80
Table 4.4	The classification of chips into acceptable chip morphology =1, unacceptable chip morphology = 0 and transitioning chips = 0.5.	84
Table 4.5	The classification of chips into chip mechanical twins observed = 1, no chip mechanical twins observed = 0.	87
Table 4.6	The boundary conditions set for the machinability map	87
Table 4.7	Ti-64 machinability map parameters (β_0 , β_1 and a) used for each of machinability outputs along with the statistical significance, p and the Adjusted R ² value of each line.	89
Table 4.8	Ti-64 machinability map parameters (β_0 , β_1 and a) for the chip mechanical twins line found using the Linear SVM model and the corresponding accuracy of the model.	89
Table 4.9	Ti-407 machinability map parameters (β_0 , β_1 and a) used for each of machinability outputs along with the statistical significance, p, and the Adjusted R ² value of each line.	89
Table 4.10	Ti-407 machinability map parameters (β_0 , β_1 and a) for the chip mechanical twins line found using the Linear SVM model and the corresponding accuracy of the model.	89
Table 5.1	Table presenting the cutting parameters used to turn Ti-407 STA billet (in Figure 5.4)	104

Table 5.2	The boundary conditions set for each factor applied in the machinability model.	105
Table 5.3	Shows the results from the machining trials conducted at a depth of cut of 0.5 mm. The first column shows the chip form resulting from the experiments. The second column shows the chip geometry. The third column shows the adiabatic shear band, with filled white arrows to represent the thickness of the shear band and the unfilled white arrows representing the formation of mechanical twins. Fourth column shows the depth of mechanical twins. The fifth column shows the 3D scans of the tool edge. The sixth column presents the average cutting force and the standard deviation for the test.	107
Table 5.4	Shows the results from the machining trials conducted at a depth of cut of 0.3 mm. The first column shows the chip form resulting from the experiments. The second column shows the chip geometry. The third column shows the adiabatic shear band, with filled white arrows to represent the thickness of the shear band and the unfilled white arrows representing the formation of mechanical twins. Fourth column shows the depth of mechanical twins. The fifth column shows the 3D scans of the tool edge. The sixth column presents the average cutting force and the standard deviation for the test.	112
Table 5.5	Series of photographs and micrographs of the chips before and after the completion of this PhD. The filled white arrows in c) and f) are indicating the width of the shear bands. The unfilled white arrows in c) are pointing to the formation of the mechanical twins surrounding adiabatic shear band	115

Nomenclature

AISI	American Iron and Steel Institute
AMRC	Advanced Manufacturing Research Centre
ANFIS	Adaptive Neuro-Fuzzy Inference System
ASB	Adiabatic Shear Band
ASP	Arbitrary Strain Path
BCC	Body Centred Cubic
BOR	Burgers Orientation Relationship
BUE	Build up Edge
CAD	Computer Aided Design
CP-Ti	Commercially Pure Titanium
CRSS	Critically Resolved Shear Stress
EBSD	Electron Backscattered Diffraction
EDM	Electrical Discharge Machined
FAST	Field Assisted Sintering technique
FCC	Face Centred Cubic
FEM	Finite Element Modelling
HCF	High Cycle Fatigue
JC	Johnson Cook
LAGB	Low Angle Grain Boundary
m	Schmid Factor
MA	Mill Annealed
$M_{s/f}$	Martensite (Start/Finish)
RSM	Response Surface Methodology
SFE	Stacking Fault Energy
SHPB	Split Hopkinson Pressure Bar
SPD	Severe Plastic Deformation
STA	Solution Treatment and Aged
SVM	Support Vector Machine
TiC	Titanium Carbide
α	Hexagonal Close Packed Alpha Phase
β	Body Centred Cubic Beta Phase
σ	Stress
ε	Strain

Tool Parameters and Cutting Coefficients

DOC	Depth of Cut
f	Feed Rate
F	Friction Force
F_c	Cutting Force
F_n	Normal Force
F_s	Shear Force
F_t	Thrust Force
MRR	Material Removal Rate
N	Normal Pressure Force
R	Resultant Force
t	Uncut Chip Thickness
v	Cutting Speed
v_c	Chip Speed
α	Rake Angle
β	Friction Angle
τ_s	Shear Stress
φ	Shear Angle

Modelling

C-L	Cockroft-Latham
k	Constant
m	Strain Rate Sensitivity
Q	Activation Energy
R	Ideal Gas Constant
T	Temperature
β_0	Slope Coefficient for the Cutting Speed Variable
β_1	Slope Coefficient for the Feed Rate Variable
ε_0	Strain

Key Terms Used Within This Thesis

Crater Wear	Chemical diffusion wear commonly observed on the rake face of the tool
Flank Wear	Abrasive wear on the flank of the tool caused by the rubbing of the tool against the machined surface.
Notch Wear	A small ‘V-shaped’ cut on both the rake and flank face commonly caused by adhesion and subsequent breaking of chips from the tool edge
White Layer	Also known as alpha case. Observed as an oxygen-enriched layer created when the material is exposed to excessive heat and oxygen during machining.

Introduction

The aerospace industry is the leading user of titanium alloys. High strength-to-weight ratio at elevated temperatures, along with improved fracture and corrosion resistance make them desirable for front of engine aerospace applications such as discs, blades, shafts and casings, where alloys have to be capable of working at temperatures up to 550°C [1]. Titanium alloys also account for 10% of the airframe weight [2], used in applications including landing gears and large wing beams.

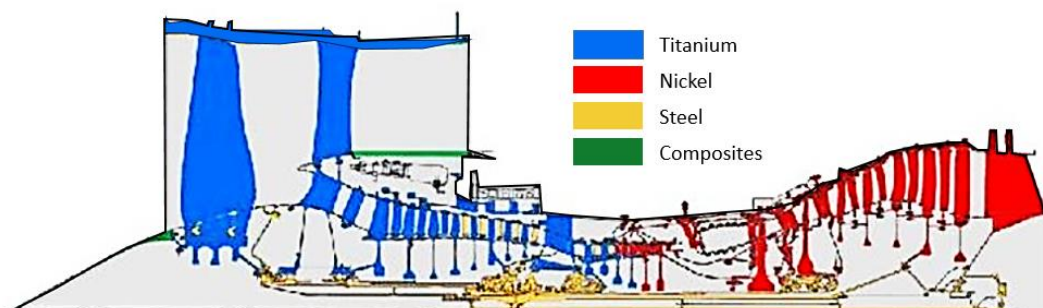


Figure 1.1: Half cross-section of “The Jet Engine, Rolls-Royce plc” colour coded with respect to the materials used for the main components. Modified from Anvari [3].

In 1988, titanium alloys accounted for 7.2 % of the total airframe usage in the Airbus A320, while aluminium accounted for 65.5 %. Today the Airbus A350 XWB is estimated to contain 14 % titanium by weight; 7 % more than steel and 6 % less than aluminium. The improved fatigue properties of titanium alloys compared to aluminium alloys has boosted the range of applications of the alloy and has helped to bring down the cost of non-routine component replacements [4]. However despite its excellent properties, the greater cost associated with processing and manufacturing has limited the use of titanium alloys across other industries such as the automotive industry. Up to now, titanium has only been incorporated into luxury and sports cars, a wider distribution of titanium in the industry would only be made possible with a radical reduction in the cost of processing and manufacturing. With the development in Field Assisted Sintering Technique (FAST) as a low cost titanium alloy processing route, the mainstream use of titanium within other industries could become reality [5]. Conventional wrought processing and machining costs of titanium alloys are significantly higher than the equivalent aluminium and steel parts in the order of 20 and 40 times more, respectively [6], [7]. Of this, machining generally accounts for nearly 60 % of the overall manufacturing costs [8].

Poor machinability attributed to excessive tool wear at low material removal rates, is the response to several inherent properties: (1) High chemical reactivity, which increases the tendency for the alloy to both weld itself to the tool as build-up-edge (BUE) and/ or crater wear across the rake face of the tool- putting the tool at risk of chipping and premature tool fracture, (2) low thermal conductivity- which increases the localised cutting temperatures at the tool-workpiece interface, affecting tool life and chip breakability and (3) the low modulus of elasticity- causing material deflection during machining, limiting the ability to cut at high metal removal rates especially for thin walled components [9].

This work aims to understand some of the key machining characteristics of an emerging titanium alloy, Timetal 407, which was developed for improved ductility, to reduce manufacturing costs and increase machining cutting speeds [10]. The alloy will be a direct replacement for the long considered workhorse alloy Ti-6Al-4V in applications where energy absorption during fracture and high cycle fatigue (HCF) limit are critical, such as a large structural gas turbine engine components.

The large structural gas turbine engine component in question surrounds the compressor section of the engine, and its design serves two purposes. Firstly to provide a casing to encase the fan, helping to funnel air through and around the engine, and secondly to protect the passengers in the event of a catastrophic failure of a fan blade. This component has typically been made from titanium alloy Ti-6Al-4V (Ti-64), due to the high strength and moderate ductility of the alloy, however in an attempt to reduce manufacturing costs and save weight, development of emerging alloy Timetal 407 has been completed to replace Ti-64 in this application. Ti-407 has been developed with improved machinability.

1.1 Thesis Motivation

This research was completed to investigate three areas of development relating to the machining of titanium alloys. The first was to improve and demonstrate the feasibility of the small-scale machinability approach developed at the University of Sheffield, presenting a series of preliminary tests to identify key machining characteristics of emerging titanium alloys. This work follows on from previous research by Marshall et al. [11] and Hatt et al. [12] utilising their experimental methods. Development of the Arbitrary Strain Path was conducted to improve the reliability and accuracy of the methodology used for the orthogonal cutting experiments. This work also utilises a uniaxial compression test rig to learn about material deformation properties and diffusion couple experiments to learn of the chemical reactivity of the materials investigated in this work. The second part of this research calls for an understanding of the machinability of emerging alloy, Timetal 407; in particular why chip control issues exist and what methods can be explored to improve this. The third part of this research is around the development of a simple-to-visualise machinability map to directly compare the

machining performance of different alloys during the early stages of material development, and to guide machine operators in exploiting the optimal cutting parameters to maximise material removal rate and reduce costs, through lower tool wear, better chip evacuation and minimal subsurface integrity issues. For the purpose of satisfying the requirements of the industrial sponsors, the scope of the second and third part of this research was limited to turning operations using CNC machine centres.

1.2 Thesis Outline

Chapter 2: Literature Review

Provides a background into the classification of titanium alloys and the effect of composition on properties. This is followed by an overview of the key deformation modes in titanium alloys. A review of the methods to achieve different microstructures and how the microstructure affects machining characteristics. An evaluation of the mechanics of metal cutting and how alloy machinability is assessed, before finally reviewing the literature on work currently completed surrounding the new emerging alloy, Timetal 407.

Chapter 3: A Low Cost Machinability Approach to Accelerate Titanium Alloy Development

Chapter 3 focusses on the first objective of this research, to develop the methodology for the series of early stage, small scale tests to identify key machinability characteristics for emerging titanium alloys. The results are correlated with high speed machining experiments to validate the small-scale test results and demonstrate the commercial incentive of such testing methods.

Chapter 4: Machinability Maps – Towards a Mechanistic Understanding of the Machining of Ti-6Al-4V and Timetal 407

Chapter 4 presents results on understanding the issues of chip control during machining of Timetal 407, which have been presented in an easy-to-visualise *machinability map*. *Machinability maps* were developed to present machinability in a new way incorporating the main factors tool wear, subsurface deformation and chip form. The maps demonstrate that machinability can be quantified and an optimal region of cutting parameters can be identified for these two alloys.

Chapter 5: Validation of “Machinability Map” Approach: Improving Chip Control During the Machining of Titanium Alloy Ti-407

Chapter 5 explores the results from a set of experimental trials planned and conducted to validate the machinability maps presented in Chapter 4, and secondly to improve the chip control of Timetal 407 during machining with a strong overall understanding of the implications of improved chip control on the other key factors of machinability, tool wear, subsurface deformation and cutting forces. The experimental trials were designed to closely mimic the operational set up utilised during the commercial machining of aerospace components.

Chapter 6: Summary and Future Work

Chapter 6 summarises the main outcomes and how this research adds to the literature. The future work section provides a clear outline for the direction of continuing research utilising the methods developed in this research and encouraging those to take full advantage of the commercial applicability.

References

- [1] H. J. Maier, “High-temperature fatigue of titanium alloys,” *Mater. High Temp.*, vol. 15, no. 1, pp. 3–14, 1998.
- [2] G. Lütjering and J. C. Williams, *Titanium*, 2nd ed. Springer, 2007.
- [3] Anvari, “Failure of Nickel-based super alloy (ME3) in aerospace gas turbine engines,” *J. Chem. Eng. Mater. Sci.*, vol. 8, no. 6, pp. 46–65, Oct. 2017.
- [4] S. M. O. Tavares, “Design and Advanced Manufacturing of Aircraft Structures using Friction Stir Welding,” University of Porto, 2011.
- [5] N. S. Weston and M. Jackson, “FAST-forge – A new cost-effective hybrid processing route for consolidating titanium powder into near net shape forged components,” *J. Mater. Process. Technol.*, vol. 243, pp. 335–346, 2017.
- [6] C. Cui, B. M. Hu, L. Zhao, and S. Liu, “Titanium alloy production technology, market prospects and industry development,” *Mater. Des.*, vol. 32, no. 3, pp. 1684–1691, 2011.
- [7] S. Sikirica and Z. Fang, “Low-Cost Titanium Alloy Production,” Utah, 2016.

- [8] M. Jackson and R. R. Boyer, "Titanium and its Alloys: Processing, Fabrication and Mechanical Performance," *Encycl. Aerosp. Eng.*, vol. 9, no. 6, p. 689, Dec. 2010.
- [9] H. Hong, A. T. Riga, J. M. Gahoon, and C. G. Scott, "Machinability of steels and titanium alloys under lubrication," *Wear*, vol. 162–164, no. PART A, pp. 34–39, 1993.
- [10] S. James, Y. Kosaka, R. Thomas, and P. Garratt, "Timetal® 407: A Titanium Alloy to Enable Cost Reduction," in *Proceedings of the 13th World Conference on Titanium*, 2016, pp. 721–725.
- [11] L. Marshall, "The influence of aluminium additions on titanium during machining through the application of a novel orthogonal cutting test method." Sheffield, 2014.
- [12] O. Hatt, H. Larsson, F. Giuliani, P. Crawforth, B. Wynne, and M. Jackson, "Predicting Chemical Wear in Machining Titanium Alloys Via a Novel Low Cost Diffusion Couple Method," *Procedia CIRP*, vol. 45, pp. 219–222, 2016.

Literature Review

2.1 Titanium Alloy Classification

Titanium is a two phase alloy consisting of the hexagonal-close-packed (HCP) alpha phase at low temperatures and the body centred cubic (BCC) beta phase at high temperatures illustrated in Figure 2.1. The transformation between the two phases is known as the β transus temperature and occurs at approximately 882 °C, depending on alloy purity.

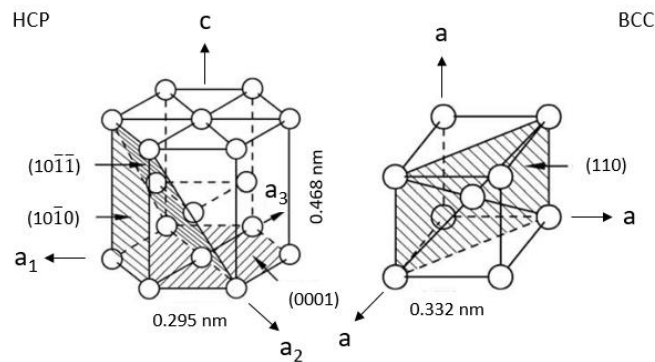


Figure 2.1: Crystal structures of alpha and beta phases of titanium. From ref [1].

When titanium alloys are cooled from the β phase, two important observations occur, firstly the phase transformation follows the Burgers orientation relationship (BOR), so the most densely packed $\{110\}_\beta$ planes of the BCC phase transform to the $(0001)_\alpha$ basal planes of the HCP phase, and secondly the distance between the closest packed planes in each phase increase.

Discussing the first point, the nucleated α phase during the cooling process is related to the β phase, such that $(0001)_\alpha$ is parallel to $(101)_\beta$ and in those planes the $\langle a \rangle$ type $[11\bar{2}0]_\alpha$ is parallel to $[11\bar{1}]_\beta$ direction. Alignment of the $\langle a \rangle$ direction in both the HCP and the BCC phase is important to control the effective slip length. In the HCP phase there are three directions $\langle a_1 \rangle$, $\langle a_2 \rangle$ and $\langle a_3 \rangle$, which as shown in Figure 2.2 range from perfectly aligned, with the (101) direction in the β phase to misaligned by 35.26° with the $(10\bar{1})$ direction.

The cooling process can lead to twelve $(0001)_\alpha$ variants from a single prior β grain, which are made up of the six $\{110\}_\beta$ planes, each of which have two directions. A number of studies have been conducted to determine the preferential orientations to nucleate from the β phase to α phase for the purpose of managing the performance of an alloy, through control of the effective slip length [2], reducing the propensity of basal cleavage facet fatigue [3] and the heterogeneity of elastic and thermal expansion of α sub-units [4]. If a limited number of α variants nucleate during cooling, macrozones containing large regions of similar orientation can form. These macrozones are well known to facilitate slip, acting as crack nucleation sites, ultimately being detrimental to the fatigue resistance [5], [6].

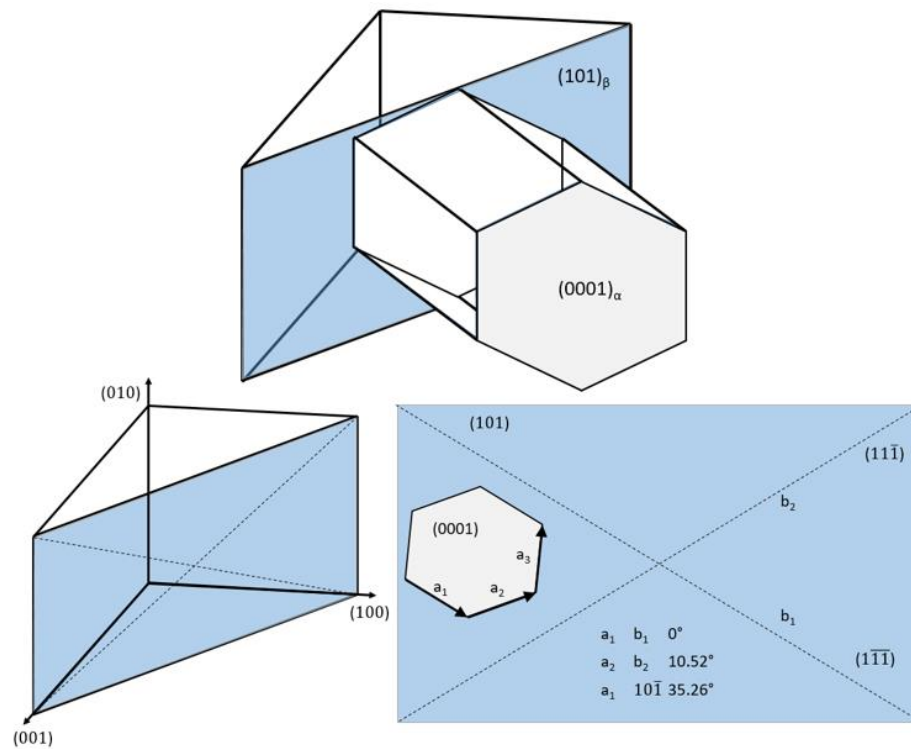


Figure 2.2: The Burgers orientation relationship between the α (HCP) and the β (BCC) titanium alloy phases, showing $(0001)_\alpha // (101)_\beta$, $[11\bar{2}0]_\alpha // [11\bar{1}]_\beta$ and the relationship between HCP $\langle a \rangle$ type directions and the equivalent BCC directions adapted from [7]

Another effect of cooling from the β to α phase is an effect of atomic distortion. Atomic distortion reduces the c-axis relative to the a-axis, thus reducing the c/a ratio to 1.587 ($a = 0.295$ nm and $c = 0.468$ nm), less than the ideal of 1.633. The ratio of the close-packed planes is too tight to slip, but causes the spacing between the prism planes to increase, preferentially causing slip to occur on planes such as $\{10\bar{1}0\}$ ‘prism’ plane [8]. However the ratio can be increased slightly by inserting interstitially

dissolved atoms such as carbon, nitrogen and oxygen atoms or by incorporating substitutional atoms with smaller atomic radius, such as aluminium [1], [9].

The addition of solute alloying elements to titanium has a number of effects including; increasing or decreasing the β transus temperature, and affecting the material properties. The elements carbon, nitrogen, oxygen and aluminium are soluble in the α phase and raise the β transus temperature whereas molybdenum, vanadium, iron and silicon are examples of β stabilising alloying elements that lower the β transus temperature. In general the α stabilising elements are used in titanium alloys to increase high temperature creep strength.

The β stabilisers can be categorised as either isomorphous or eutectoid. Above a concentration threshold the β isomorphous elements are capable of retaining the β phase down to room temperature whereas the β eutectoid formers will produce some form of intermetallic phase under equilibrium conditions. The β stabilising elements are used to lower resistance to deformation, which increases the workability of the alloy.

Of the α stabilising elements, aluminium is the most widely used as it has a good solid solubility in both phases and is in high abundance. The use of aluminium in titanium is limited up to an amount of about 6 wt.% in order to minimise the formation of the intermetallic compound Ti_3Al (α_2) which leads to the embrittlement of the alloy negatively affecting fatigue performance [10]. Oxygen can also be used to increase strength, whilst simultaneously reducing the ductility of the alloy, however its presence is controlled to minimise the risk of oxygen diffusion at high temperatures, which can form an alpha rich layer at the surface, leading again to alloy embrittlement [10].

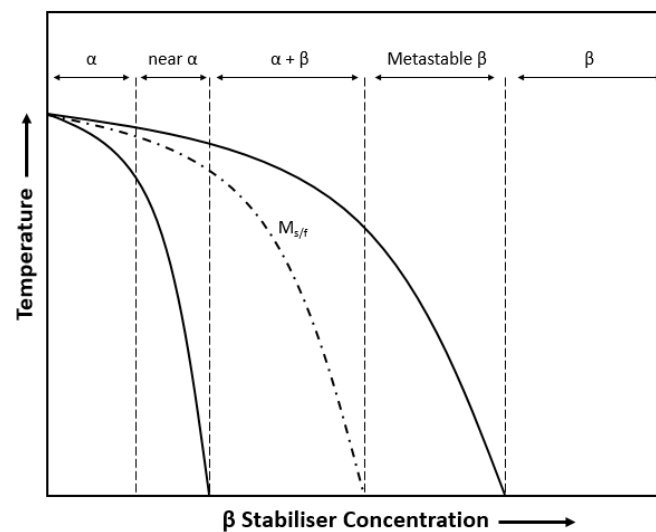


Figure 2.3: Pseudo-binary titanium phase diagram. Redrawn from [11].

The pseudo-binary phase diagram in Figure 2.3 categorises titanium alloys as a function of their β stabilising concentration. The martensite start/finish line (denoted by $M_{s/f}$) identifies the position below which, alloy compositions will transform martensitically when cooled rapidly to room temperature. A brief overview of each class is presented below.

2.1.1 α Alloys

The α -alloys include the numerous grades of commercially pure titanium (CP-Ti) which are strengthened by oxygen in solid solution. The oxygen content in CP-Ti typically varies between 0.18-0.40 wt.% with high oxygen content increasing the tensile strength, consequently limiting the plastic strain accommodation [12]. α alloys are generally more resistant to creep and possess good strength at high temperatures, however they do not respond to heat treatments, and possess limited room temperature strength compared to β alloys, owing to their single crystal composition. It should also be noted that CP-Ti exhibits high rates of work hardening [12]. The work hardening effect as discussed later, offers the unique deformation properties of titanium alloys and is one of the reasons for the considered, poor machinability of alloys. Aerospace applications for CP-Ti include water supply systems which require good corrosion resistance and good formability [13].

2.1.2 Near α Alloys

The near α alloys contain small amounts of β stabilising elements intended to widen the $\alpha + \beta$ phase field to enable titanium to operate at higher temperatures. Due to the β stabilising additions, a small volume fraction of β phase is retained at room temperature. With the addition of alloying elements such as silicon, the creep resistance and strength capabilities can be exploited for applications up to an elevated temperature of 600 °C [14]. The small amount of β phase improves the workability of the alloy during the forging process. Ti-834 is an example of a near α alloy with a tensile strength of 1025 MPa and an elongation of 5%. The alloy possesses a great balance of fatigue resistance, ductility, creep resistance, fracture toughness and temperature stability, making it ideal for applications such as compressor discs and blades [15].

2.1.3 $\alpha+\beta$ Alloys

The $\alpha + \beta$ alloys contain alloying elements to strengthen the α phase but also retain some of the β phase at room temperature. The most widely used alloy in the $\alpha + \beta$ category is Ti-6Al-4V (Ti-64) [1], developed in the 1950s and used in applications ranging from rotating discs and fan blades in the aerospace sector to joint replacement implants in the medical industry. The tensile strength of Ti-64 is in the region of 895 MPa with an elongation of around 10 % [13]. The extensive applicability of this

alloy across multiple industries is made possible by the variety of properties that can be achieved with the two phase microstructure. Thermo-mechanical processing routes are necessary to exploit these properties, providing one of three types of microstructure: fully lamellar, bi-modal and fully equiaxed [10].

2.1.4 Metastable β Alloys

The metastable β alloys have compositions to the right of the $M_{s/f}$ line in Figure 2.3. The concentration of β stabilising solutes is sufficiently high to suppress the ' $M_{s/f}$ ' to below room temperature resulting in a material that retains the β content at room temperature [10]. The high volume fraction of β phase allows hot working at lower temperatures than the $\alpha+\beta$ alloys, and age hardening by the precipitation of fine α particles yielding high fracture toughness and high strength. Ti-10V-2Fe-3Al alloy is used for landing gear applications, given its hardenability, high strength and high fatigue strength. It has a tensile strength of 1240 MPa or higher, and elongation of 4% at room temperature [13].

2.1.5 β Alloys

The β alloys which are to the right of the metastable β alloys on the pseudo-binary phase diagram in Figure 2.3 are heavily β stabilised alloys. In general β alloys are not considered thermodynamically stable, as they can undergo α precipitation on aging. These alloys do not possess the same high strength properties of the metastable β alloys, but do offer great cold workability and can be recrystallised at low temperatures, to form fine grained β structures. Compared to $\alpha + \beta$ alloys they have higher density and improved fracture toughness but lower creep resistance and ductility in an aged condition [10]. Ti-15V-3Cr-3Al-3Sn is an example of a β alloy, in a solution treated and aged condition the tensile strength is roughly 1000 MPa and the elongation is about 7% for applications such as welded pipes and ducts [13].

2.2 Deformation Modes

The plastic deformation behaviour of titanium is very closely related to its crystal structure. The HCP crystal structure of the α titanium exhibits anisotropic deformation behaviour [1], [10]. Depending on the crystallographic orientation, the Young's modulus of titanium can vary considerably, from 100 GPa vertical to the basal plane to 145 GPa across the basal plane [1], [16], [17].

Plastic deformation in α titanium occurs by two modes, slip and twinning. Both mechanisms contribute to the accommodation of plastic strain and are fundamental to understanding the process of chip forming and subsurface damage from machining. Plastic deformation is a phenomenon whereby a material exhibits a permanent change to shape as a response to an applied force or a change in temperature. The force can be applied in any one of, or multiple of tensile, compressive, shearing or bending which provides energy in the form of work done. Temperature, provides the material with heat energy enabling microstructural features such as grain boundaries, dislocations, stacking faults and twins to become mobile. The movement of the microstructural features is dictated by the strain, strain rate and temperature.

2.2.1 Slip

Slip is the process by which deformation occurs through dislocation motion. The schematic of the HCP crystal in Figure 2.1 illustrates the slip planes and directions available for titanium. Titanium primarily slips in the three close packed directions of the basal, prismatic and pyramidal planes. Since von Mises criterion states that a minimum of five independent slip systems are required to accommodate plastic deformation, the activation of the $\bar{c} + \bar{a}$ Burgers vector or twinning is required for titanium to accommodate its strain. [18].

As the activation of slip in a stressed material is dependent on the grain orientation of the material, the Schmid factor can be used to calculate the critically resolved shear stress (CRSS) in relation to the loading axis. Titanium alloys will plastically deform, when the applied stress is more than or equal to the CRSS. The CRSS represents the minimum shear stress required to initiate the dislocation slip and is generally regarded as a material property [19]. The calculation for CRSS is, $\tau_{CRSS} = \sigma m$, where σ is the applied stress and m is the Schmid factor. The CRSS values are strongly dependent on the alloy composition and the temperature at which deformation occurs. At room temperature the required CRSS for the $\langle a \rangle$ type slip systems to become activated, from low to high are: $\{10\bar{1}0\} < \{10\bar{1}1\} < (0001)$. The CRSS for $\langle c + a \rangle$ slip systems are significantly higher in single crystals such as Ti-6.6Al [10] and in polycrystalline materials such as Ti-64 [20]. In compression tests performed by Partridge [21], the $\langle a \rangle \{10\bar{1}0\}$ slip plane was activated at 392 MPa, followed by $\{10\bar{1}1\}$ at 404 MPa and (0001) at 444 MPa. Pyramidal $\langle c + a \rangle$ slip activated at 631 MPa.

Table 2.1: Slip systems in the HCP α phase [10]

Slip system	Burgers vector	Slip direction	Slip plane	No. of slip systems	
				Total	Independent
1	\bar{a}	$\langle 11\bar{2}0 \rangle$	(0001)	3	2
2	\bar{a}	$\langle 11\bar{2}0 \rangle$	$\{10\bar{1}0\}$	3	2
3	\bar{a}	$\langle 11\bar{2}0 \rangle$	$\{10\bar{1}1\}$	6	4
4	$\bar{c} + \bar{a}$	$\langle 11\bar{2}3 \rangle$	$\{10\bar{1}1\}$	12	5

2.2.2 Twins

Slip in HCP structures is limited due to the low symmetry and insufficient independent slip systems. Twinning is therefore required in combination with slip to accommodate strain. Twinning causes a reorientation of a small part of the crystal lattice as illustrated in Figure 2.4, and allows further slip to occur in the structure. Further slip is achieved as twins may place new slip systems in orientations favourable to the stress axis allowing slip to occur.

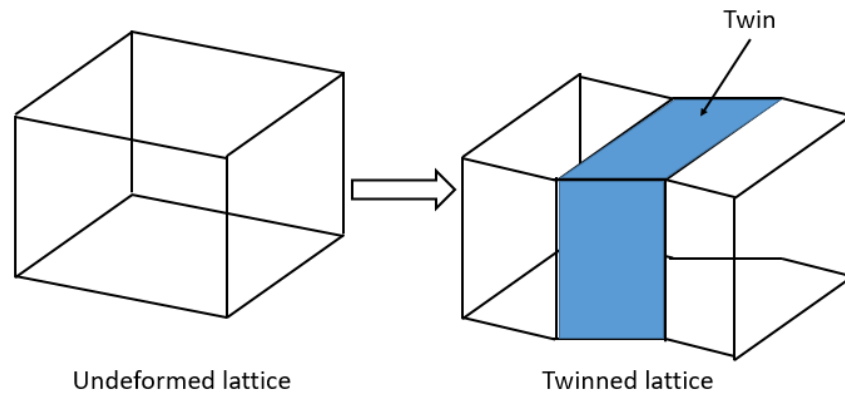


Figure 2.4: Schematic of a deformation twin causing rotation of the crystallographic lattice

Like dislocation slip, deformation twins proceed in order to minimise the work done in a material in response to an external stress [22]. The activation of deformation twins results in grain fragmentation caused by the intersection of twins. The twins quickly saturate the microstructure leading to a decline in the twinning activity, which allows dislocation slip to dominate [23]. Twinning modes can be split into two distinct groups, namely, compression twins and tension twins. At room temperature $\{10\bar{1}2\} \langle \bar{1}011 \rangle$ extension twin and $\{10\bar{2}2\} \langle 11\bar{2}3 \rangle$ compression twin are the most commonly

observed in pure titanium [24]–[26] because they have the smallest twinning shear. Twin activity is very high in CP-Ti during the deformation of the material, however it has been reported to be absent in Ti-6Al-4V [10]. The reasons for this are not entirely clear however it is suggested to be related to the smaller grain size, high aluminium content and the presence of Ti_3Al precipitates in Ti-6Al-4V [10]. Aside from accommodating plastic deformation, twinning contributes to the refinement in the microstructure of the deformed titanium [27] and the work hardening behaviour of the α titanium [28], [29]. Twins are strain rate sensitive, often forming under very high strain rates. Ti-64, which was suggested by Lütjering [10] to be unable to form twins due to the high aluminium content of 6 wt. % was observed to form twins during shock loading experiments [30], or when deformation takes place at cryogenic temperatures [31].

2.2.2.1 Texture Evolution

Polycrystalline materials consist of grains of different sizes, shapes and crystal orientations. The preferred orientation of the crystals within the material are referred to as the texture of the material [32]. Texture has a direct effect on mechanical properties of a material, including tensile strength, ductility, toughness and Young's modulus [26]. Gurao et al. [33] investigated deformation behaviour of CP-Ti in different crystallographic orientations, and revealed that a material with a preferred texture towards the basal plane exhibits higher yield strength but less twinning under loading, hence, lower strain hardening rate, whereas a prismatic orientation exhibits lower yield strength but higher strain hardening rate. Therefore the processing of a material is essential to develop the texture of the material through methods including annealing, plastic deformation and phase transformation.

2.2.2.2 Work Hardening Behaviour

Work hardening or strain hardening rate, refers to the increasing stress required to continue deformation at any instance during plastic strain. Work hardening typically increases the capacity for a material to carry a load before fracturing. It is vital to understand the work hardening due to its influence on the fracture and deformation properties in a material. Strain hardening arises from the interaction of dislocations with each other, which over time build up to a point where they become immobilised. Without greater stresses the grains are unable to deform any further [34]. Salem et al. [28], [29] studied the strain hardening behaviour of α titanium under compression, identifying three distinct phases as depicted in Figure 2.5. Stage I was identified as the region of decreasing work hardening rate, where deformation is accommodated predominantly by slip, whereas Stage II, a region of increasing work hardening rate, is dominated by twin formation and slip. During this stage the effective slip distance is reduced due to the grains being divided by the existence of twin boundaries, thus, the stress required

for continuous plastic deformation is increased. Stage III exhibits a decreasing work hardening rate, which is theorised to be driven by a saturated twin density, making twin formation more difficult. The strain is accommodated by slip, similar to stage I. The work hardening behaviour of titanium proposed by Salem has also been reported in a number of other studies including those conducted by Nasser et al., Becker et al., Fitzner et al. and Marshall et al. [35]–[38].

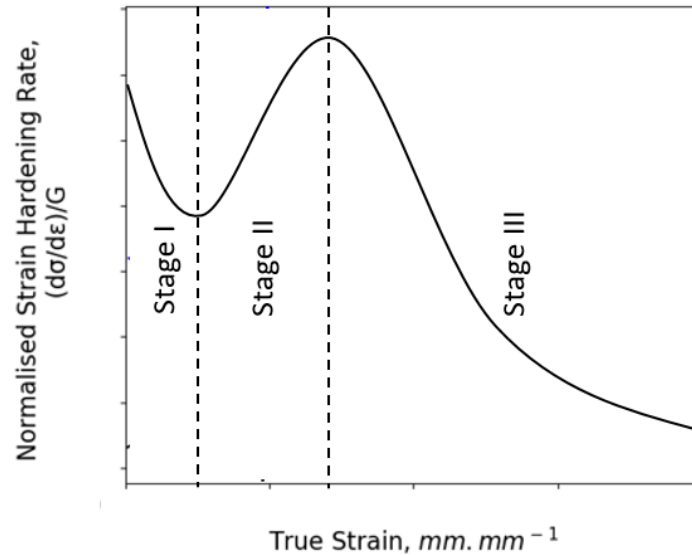


Figure 2.5: Plot showing the three stages of the normalised strain hardening rate against strain curve

2.2.2.3 Grain Size Effect

The effects of grain size on deformation in titanium has been studied by numerous authors. A number of studies have shown that titanium follows the Hall-Petch relationship [39], [40] where decreasing grain size, increases the yield strength of titanium. In addition to yield strength, the effect of grain size on twinning has been investigated. One paper by Ghaderi & Barnett [41] studied the grain size effect on twinning in magnesium and titanium. Their results revealed that the twin density increased with increasing grain size in magnesium and titanium, though the effects were stronger in titanium. Similar results for titanium were presented by Gupta et al. [34] and Salishchev & Mironov [42], who found that reducing the grain size beyond a point, limited the work hardening behaviour.

2.2.2.4 Stacking Fault Energy

For metals with an FCC crystal structure, it has been long established that the propensity for twin nucleation is related to the stacking fault energy (SFE), as the stacking fault can act as a nucleation site for twin activity [43], [44]. In the absence of ordering, aluminium does lower the SFE on the basal

plane in titanium [45], this should limit the mobility of dislocations in a material, thus requiring greater stress to enable grains to deform, hence making twin nucleation easier. Ordinarily this should increase the work hardening rate however studies by Marshall et al. and Fitzner et al. [37], [38], demonstrate that this is not the case.

2.2.2.5 Effect of Aluminium on Deformation Twins

As previously mentioned aluminium is widely used in titanium alloys as an α stabiliser. Numerous studies have presented work on the influence of aluminium on the deformation characteristics of titanium alloys, in particular on the propensity for slip or the formation of deformation twins. Leyens [1] and Levine [9] revealed that to encourage slip and reduce the propensity to twin formation during the deformation of titanium alloys, aluminium could be used to increase the c/a ratio. Lütjering [10] published work suggesting that concentrations above 6 wt.% would completely suppress the formation of twins. Through comparisons of the deformation mechanisms of CP-Ti and Ti-64 it has been revealed that CP-Ti is more preferential to twin than Ti-64, however the reasons surrounding this are unclear as it is argued that it could be due to a number of variables including, the smaller grain size or, higher aluminium content or the presence of Ti_3Al precipitates in the Ti-64 [10]. In order to establish what the effect of aluminium is in titanium, authors including Marshall et al., [37] and Fitzner et al. [38] have concentrated their efforts on analysing the deformation mechanisms using different Ti-Al binaries.

Marshall et al. [37] observed the three regions suggested by Salem [28], [29] in Ti-Al binaries from room temperature compression tests, showing that the greatest region II work hardening rate occurred in Ti-Al 4 wt. % indicating that it has undergone the highest amount of deformation by mechanical twinning. The lowest region II work hardening rate occurred in the Ti-Al 8 wt. %. Fitzner et al. [38] also determined that decreasing aluminium content suppressed some twin types, but encouraged other types to form. In particular the $\{11\bar{2}2\}$ compression twins and the $\{10\bar{1}2\}$ tensile twins, both occurred less frequently with increasing aluminium content, however, the $\{11\bar{2}1\}$ tensile twins, occurred more frequently with increasing aluminium content. Battaini [46] also studied the effect of chemistry on deformation and found that the CRSS for the $\{10\bar{1}2\}$ tensile twin increases as the purity of the alloy decreased.

2.3 Titanium Alloy Microstructure

As previously mentioned, in the category of $\alpha + \beta$ alloys there are three categories of microstructure. The two extreme microstructural types include: the lamellar structure- formed by

cooling from the beta phase, and the equiaxed structure- formed during the process of recrystallization [11].

2.3.1 Microstructure Types

The equiaxed microstructure is characterised by high ductility and resistance to fatigue crack initiation and low cycle fatigue resistance [47]. It consists of primary grains embedded in a beta matrix. The key to processing an equiaxed microstructure is through cooling at a sufficiently slow rate that the α_p grains are able to grow, inhibiting the lamellae formation inside β grains [10].

The lamellar microstructures from Figure 2.6, are achieved through an annealing treatment in the β phase field before being cooled rapidly to room temperature. The lamellar microstructure consists of parallel α plates separated by β plates. The lamellar microstructure offers a few advantages to the equiaxed microstructure, [48], [49] including enhanced creep properties, lower oxygen diffusivity, and fatigue crack growth resistance. It has been proposed that fracture properties are strongly influenced by the α -colony size and the α/β interface thickness. Increasing the size of the α -colonies, increases the resistance to crack propagation [10].

The bimodal microstructure consists of equiaxed primary α in a lamellar of an α/β matrix. This type of microstructure offers a balance of strength and ductility, two properties considered to be mutually exclusive [47]. There is an increased number of processing variables to consider, including volume fraction of the phases, grain size and alloying element segregation, each will affect the final properties of the material [10].

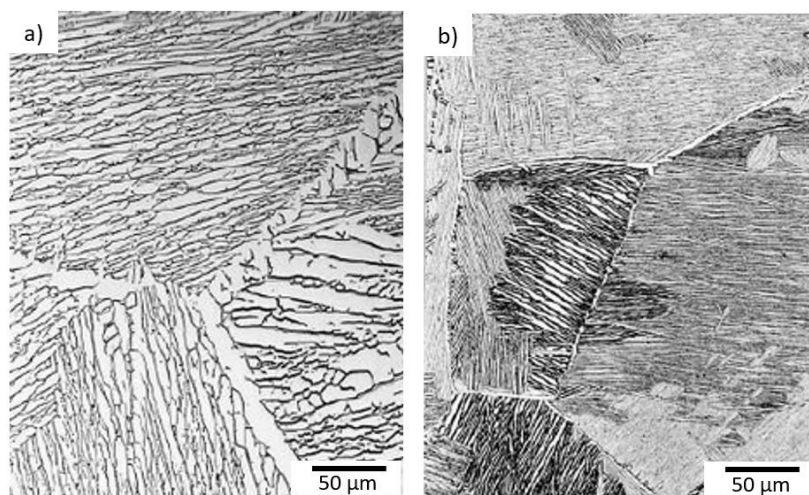


Figure 2.6: Effect of cooling rate from the β phase on the lamellar microstructure of Ti-6242. a) 1 °C/min b) 100 °C/min [50]

2.3.2 Titanium Annealing Process

Annealing is a heat treatment process which alters the microstructure of a material, with the purpose of changing mechanical properties. The annealing of titanium alloy's serves to improve fracture toughness, reduce hardness and eliminate internal stresses. The most common annealing treatments are: mill anneal, duplex anneal, recrystallisation and beta anneal.

2.3.2.1 Mill Annealing

Mill annealing is a treatment given to all mill products. It is not considered a full anneal as it has the potential to leave traces of cold or warm working in the microstructure.

2.3.2.2 Duplex Annealing

Duplex annealing is the process of heating quickly, holding for a certain time and air cooling [51] to alter the shapes, sizes and distributions of phases to those required for improved creep resistance or fracture toughness.

2.3.2.3 Recrystallisation

Recrystallisation is used to improve fracture toughness. In this process the alloy is heated into the upper end of the α/β range, held for a time, and then cooled very slowly. In recent years, recrystallisation has replaced β -annealing for fracture critical airframe components.

2.3.2.4 β Annealing

β annealing is used to improve fracture toughness and the resistance to fatigue crack propagation [52]. β annealing is completed at temperatures above the β transus to prevent excessive grain growth [53]. The time spent at temperatures in the β transus should be kept to a minimum to control beta grain growth. After primary β annealing, a stabilisation anneal is completed to prevent the formation of the ω phase, although the effects of this phase on high cycle fatigue and tensile properties have been found to be negligible [54]. Armendia et al. [55] found that β -annealed alloys generally produce higher cutting forces than other treatments such as mill annealed or solution treatment and age (STA), which has a negative impact on tool life. The effects of β annealing with respect to other heat treatments and other factors of machinability such as subsurface features and chip formation was not

conducted. Kosaka et al. [56] conducted drilling trials in both Ti-64 and Ti54M and found that a β -annealed and recrystallisation annealed workpiece were the most difficult to drill.

2.3.2.5 Solution Treating and Age

Following the annealing, a solution treatment and age is required to improve the strength of the $\alpha+\beta$ and the β -alloys, with the exception of the Ti-2.5Cu alloy. Heating an $\alpha+\beta$ titanium alloy to the solution treating temperature produces a higher ratio of β -phase. The partitioning of α - and β - phases is maintained by quenching. Quenching is conducted at a controlled rate in one of a number of available mediums including: oil, water and air. The alloy is subsequently aged, removing the unstable β -phase, increasing the overall strength of the alloy. The solution treatment temperature for α alloys is based on the desired combination of mechanical properties. A change in the solution-treatment temperature affects the fraction of β -phase which consequently changes the response upon aging. To obtain high strength with adequate ductility, it is necessary to solution treat at a temperature high in the α/β field, normally between 25 to 85°C below the β transus of the alloy. If $\alpha+\beta$ alloys are heat treated in the beta range they would lose significant ductility [10].

2.3.3 Microstructural Effects on Machining

Microstructure has been established to have a great effect on the machinability of an alloy. Kosaka & Fox [56] and Kosaka et al. [57], investigated the machinability of Ti-64 and Ti54M in different heat treated conditions. Their work established that the machinability was influenced by the microstructure, alloys with a coarse microstructure were more difficult to machine than those with a finer microstructure. It was learnt that Ti-54M had a better machinability than Ti-64 owing to its microstructure. This was further supported by Armendia [55] reporting that, Ti-54M could be machined at cutting speeds 20% higher than Ti-64, and that both Ti-64 and Ti-54M had improved machinability when machining the alloys processed towards a finer microstructure. The authors referred to the tool life and cutting force coefficients when discussing machinability. Khanna & Sangwan [58] studied the influence of microstructure between Ti-54M and Ti-1023. It was shown very clearly that the cutting forces and the coefficient of friction was higher for both alloys in the STA condition over the annealed condition. The effect of microstructure on the measured interface temperature was not so clearly defined at different cutting speeds and feed rates. Though overall the machinability of Ti-54M was considered better than Ti-1023 in general. Egorova et al. [59] investigated the effect of beta grain size. Decreasing the size of the beta grains improved the machinability. Sun et al. [60], investigated differences between the equiaxed, bi-modal and lamellar microstructures. They revealed that the lamellar morphology was most conducive to form a serrated chip during high speed machining, with the bi-modal morphology

being the least, at cutting speeds less than $100 \text{ m}\cdot\text{min}^{-1}$. On the flip side, Nguyen et al. [61] showed that when machining Ti-64 the lamellar microstructure was of greater detriment to tool life than the other microstructural types.

Lee et al. [62], [63] conducted ballistic impact tests to investigate the dynamic torsional properties of Ti-64 of different microstructures. The use of ballistic impact testing can be directly related to machining, informing specifically on the chip forming characteristics such as adiabatic shear bands, failure mechanisms and crack propagation, as the tests are naturally conducted at very high strain rates. The results revealed that the greatest number of adiabatic shear bands and cracks formed in the impacted area of an equiaxed microstructure followed by the lamellar microstructure, and finally the bimodal microstructure, which produced the least. This was also confirmed by Zheng et al. [64] who added that the failure mechanism for equiaxed microstructure was associated with a ductile failure, whereas for the lamellar microstructure, this was a brittle failure. Seo et al. [65] showed through uniaxial compression tests that the strain at failure was higher for the equiaxed microstructure and lowest for the lamellar microstructure, agreeing with Zheng et al. [64] of lamellar being more brittle than an equiaxed microstructure. Additionally, it was observed that the deformation of the bi-modal microstructure was sensitive to lamellar and equiaxed microstructure content, where greater adiabatic shear bands were formed in the sample with higher equiaxed content.

2.3.4 Microstructural Effects on Twinning

Very little work has focussed on studying the effect of microstructure on deformation twin density. Ma et al. [48] conducted research investigating the differences in deformation mechanism between widmanstätten, bimodal and equiaxed. They concluded, that the widmanstätten microstructure exhibits much fewer slip systems per unit volume compared to an equiaxed or bimodal microstructure and therefore relies on the $\{10\bar{1}2\}$ twins to accommodate strain. However this work was not quantified by any means for the relative density of twins between each of the microstructures.

2.4 Machining Titanium Alloys

2.4.1 Principles of Metal Cutting

Following on from the titanium alloy processing, the forgings are typically machined to a desired shape through a number of different operations including: turning, milling and drilling to name a few. Metal cutting or machining, is a time consuming and expensive process, with a high percentage of material wastage, typically in the region of 80-90% [47]. Despite the huge demands for machining, it is one of the least understood manufacturing processes due to the high stresses and strains that occur

[66]. Research has tried to improve our understanding of this complex system through modelling of chip formation. This has been accomplished through simple orthogonal models similar to Merchant's [67] force diagram illustrated in Figure 2.7. Important machining variables include, feed rate, cutting speed and depth of cut, each of which influence machining outputs, such as chip type, tool wear, surface damage and cutting forces. Together these variables are widely considered the primary outputs of machinability [68], [69].

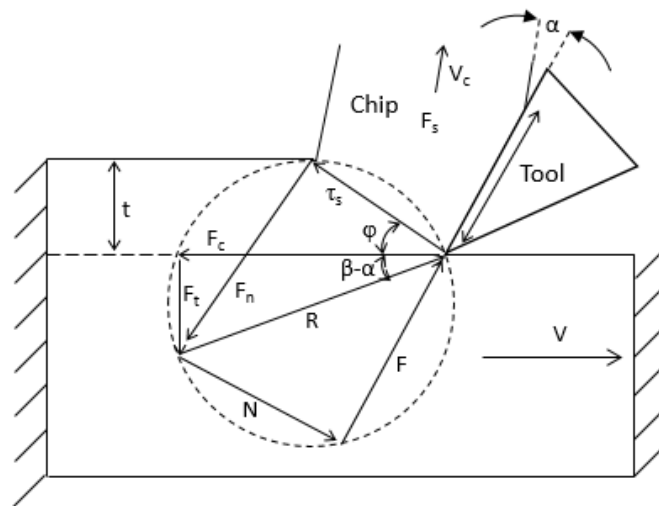


Figure 2.7: Force diagram showing the relationship between component forces in the orthogonal cutting environment. Redrawn from [67].

2.4.2 Machinability

Machinability is an ambiguous term used to describe the relative ease to cut a material. It has a number of meanings depending upon the production engineer's requirements. As mentioned above the machinability is evaluated from a number of criteria, including: tool life, surface integrity, ease of chip disposal and cutting forces.

Assessing machinability of a material can be accomplished by a number of different tests. Non-machining tests include: 1) chemical composition tests and 2) physical properties test. These type of tests are conducted prior to machining taking place, but require specialist laboratory equipment for metallographic investigation. The machining tests, which are either "short tests" or "long tests" are expensive and require large amounts of material to complete. Examples of the "short tests" include: 1) rapid facing test and 2) accelerated cutting tool wear test. The "long tests" include: 1) step turning tests, 2) variable-rate machining test and 3) taper turning test. For the "long tests" the tool is engaged for significant periods of time allowing the Taylor constants to be calculated and the tool life for different conditions to be discovered [70]. Taylor's machinability work [71] produced the foundations for

understanding how the interactions at the tool-workpiece interface controlled the tool wear rate. Taylor’s work investigated effects of tool material and cutting parameters on tool life, which was paramount to increasing the output at the Bethlehem Steel Company by 500% [70]. It is therefore common for machinability studies to focus heavily on tool wear such as by Ref [72]–[75]. Machinability should be considered with respect to the full range of machinability factors, as it is common for an alloy to exhibit good machinability by one feature but poor machinability by another.

Attempts to describe the relative machinability of different alloys was suggested by the American Iron and Steel Institute (AISI), with focus on cutting speed, tool life and surface finish, against a base steel alloy, B1112. Alloys more machinable than B1112 were rated above 1.00, those less machinable were rated less than 1.00. As shown in Figure 2.8, titanium alloys score very poorly with a machinability rating between 0.2-0.5. However this type of approach offers no guidance for how to machine these materials in order to maximise the machining output. To understand why titanium alloys are difficult to machine, the key machinability outputs have been discussed further.

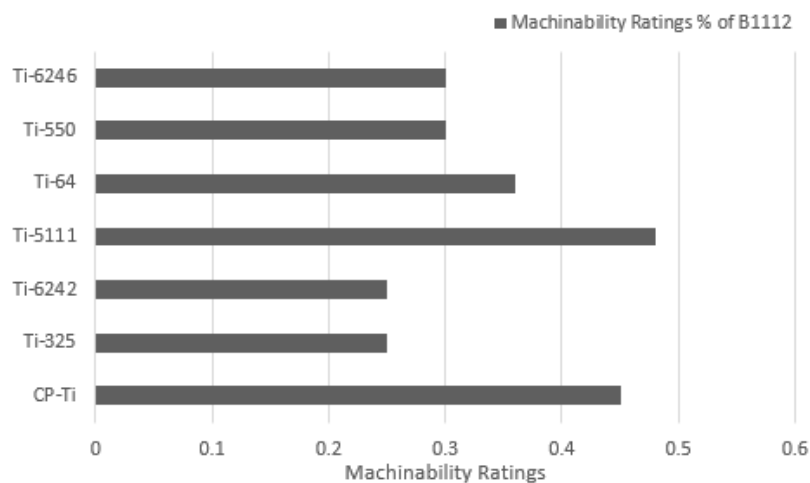


Figure 2.8: Bar chart showing the relative machinability ratings for titanium alloys against B1112.

2.4.2.1 Tool Life

Titanium alloys have high strength at elevated temperatures, low thermal conductivity, and high chemical affinity which are responsible for the high rate of tool wear during machining [76]. Ezugwu et al. [77] summarised that tool wear is the combined effect of abrasion, adhesion, plastic deformation and chemical reactivity between the workpiece and the cutting tool. The factors influencing tool wear summarised by Ezugwu et al. [77] lead to a number of tool wear types including crater wear, BUE, flank wear, chipping, plastic deformation, notch wear and thermal cracking.

Flank wear is typically used as the standard for assessing the tool life. It is the most desirable type of wear due to its predictability, often following a wear rate curve similar to that shown in Figure 2.9. An average measurement of between 0.2 and 0.3 mm of flank wear (depending on manufacturing organisation) is used as the standard limit at which point a tool change is required [78]. The reasons for this limit include, 1) a greater risk of catastrophic tool failure, 2) a component being machined out of tolerance and 3) significant damage to the machined surface.

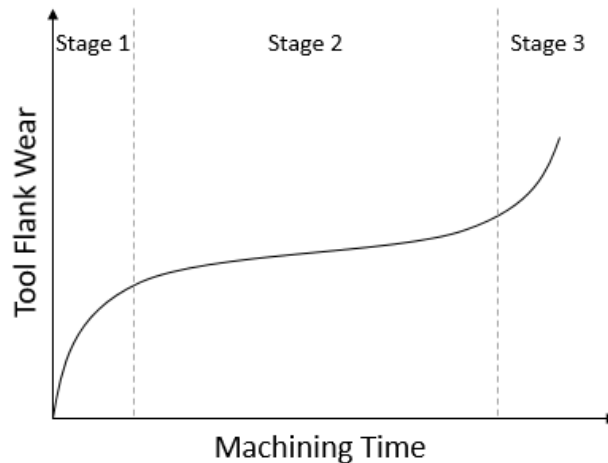


Figure 2.9: Tool life curve based on the typical flank wear rate over time.

It is necessary to set up a stable cutting area to control the tool wear, ideally to produce only flank wear. This remains a challenge as other tool wear types are unavoidable, and affect the longevity of the tool, in some cases causing tool failure before the flank wear limit has even been reached. Selection of cutting parameters becomes very individual to the material being machined, so a machinist requires experience and guidance to ensure that the tool life can be maximised.

Cutting speed plays an important role in determining the longevity of a cutting tool. At low cutting speeds mechanical wear dominates whilst at high cutting speeds, chemical reactivity plays a more critical role. The chemical wear increases exponentially with cutting speed, typically causing rapid cratering across the rake face of the tool. The friction between the tool and the workpiece causes a rapid increase in the localised temperature at the tool tip, which leads to the adhesion of a titanium carbide layer on the rake face of the tool [79]. The high temperature and pressure at the tool-chip interface creates the ideal conditions for diffusion of tool material (W, Co, C) to the workpiece [80]. The diffusion of Co from the cutting tool weakens the bond between the carbide grains allowing them to be “plucked” from the tool, thus encouraging further tool attrition. The loss of cobalt and carbon to the interface results in the formation of two important layers TiC and $\text{Co}_3\text{W}_3\text{C}_y$ (W_2C) which is also known as the η -phase which is brittle and prone to fracturing [81]. The diffusion mechanism during machining has been

studied previously [81]–[83], by applying a compressive load between the titanium alloys and a carbide tool. A further effect of high temperatures on the cutting tool is plastic deformation which softens and changes the shape of the tool edge [84]. This can be a sign of imminent tool failure, and is the result of the low thermal conductivity of titanium alloys. Another type of tool wear common with titanium alloys is BUE across the cutting edge and adhesion of workpiece material to the flank face. Wang & Zhang [85] observed adhesion, and attributed it to the high temperatures and chemical reactivity of titanium alloys. BUE is most prominent at lower cutting speeds, when the workpiece has time to weld itself to the tool edge. It is argued that BUE acts as a protective layer across the cutting edge [86], however due to the high temperatures it can contribute to the overall tool failure, by enhancing diffusion mechanisms along the rake face [87], whilst also encouraging chipping to occur every time the BUE is removed from the cutting edge. It is more common to observe BUE whilst machining ductile materials. Mills & Redford [68] discussed the impact of BUE on machinability factors and concluded that BUE especially if it was unstable would have a marked effect on surface finish, arguing that the only method for producing good surface finish was by using cutting fluid to prevent BUE. Trent [84] discussed the relationship of BUE to chip breakability, finding that there is insufficient evidence to conclude whether it benefits or hinders chip breakage.

The low modulus of elasticity of titanium alloys, causes the workpiece to push away from the cutting tool. This effect can change the relationship between the tool and workpiece causing the tool to rub rather than performing a cutting action. This increases the friction, raising the temperature, putting the tool at risk of plastic deformation, crater wear and flank wear [88]. The workpiece “springback”, caused by a low modulus of elasticity has also been shown to encourage chatter during machining. This not only affects the workpiece surface integrity, but it puts the tool at risk of chipping and fracture [89].

As well as cutting parameters, significant research in the area of tool development has been encouraging, with numerous geometries, materials and chip breakers being developed in recent years to increase productivity during machining. Typically, machining of titanium alloys is carried out using tungsten carbide cutting tools. Tungsten carbide offers a good balance of properties for machining titanium alloys including, hardness and wear resistance, especially at elevated temperatures, which is important considering that temperatures can reach in excess of 1100°C [90], [91]. Though the brittleness of the tool leaves it vulnerable to fracture, especially when dealing with the cyclic loading caused by serrated chips.

2.4.2.2 *Cutting Forces*

Cutting forces have been long established as a machinability output as they directly relate to the cost of running machines and on the tool life through the stresses exerted on the tool. The cutting

forces offer an indication of the cutting stability. With high cutting forces, excessive heat can be produced at the cutting zone which not only affects the tool life, but also the surface integrity of the component and chip formation [92]. Hou et al. [93] investigated the cutting forces of Ti-64 at a range of cutting speeds. The cutting forces appeared to decrease up to a cutting speed of 125 m.min⁻¹, before increasing above this cutting speed. This effect was attributed to the dominance of work hardening over thermal softening effects above 125 m.min⁻¹, which increased the resistance to machining. Cutting forces are affected by the underlying chemistry and microstructure of the alloy. Increasing the annealing temperature has the effect of increasing the average forces during machining [94]. To offset the negative effects of titanium's low modulus of elasticity and the subsequent "springback" reducing the cutting forces will help to improve the geometric accuracy of the finished component. Cutting forces can be an indication of tool wear, system vibrations and chip breaking. Sun et al. [95] witnessed an increase in cutting forces during machining as a result of vibration during machining. The vibrations were attributed to the low modulus of elasticity of the material and the high cutting temperatures. In the same study, the authors concluded that the cyclic force signature could be attributed to the serrated chips formed during the cutting operation. An effect which other authors [96] have concluded have a negative effect on tool life.

2.4.2.3 Surface Integrity

Surface integrity is an important measure of machinability which can be controlled by careful selection of cutting parameters. Koster et al. [97] defined surface integrity as the enhanced surface condition of a machined surface. There are two categories to surface integrity, surface roughness and subsurface microstructural features. Surface roughness is commonly the first inspection method used to ensure conformity to standards. The accessibility and simplicity of surface roughness measurements allow it to be examined whilst the component is in the machining centre. A number of other studies [98]–[101] investigated the effect of cutting parameters on surface roughness finding that increasing the cutting speed and depth of cut reduced the surface roughness, conversely feed rate was determined to increase surface roughness [98]. An unstable system, increased the surface roughness according to Sun et al. [95], this has a direct effect on the tool life, by causing delamination of tool coatings and tool failure [102]. It is therefore in the interest of the machinist to control the cutting parameters to minimise surface roughness in an effort to also reduce the rate of tool wear.

For critical components it is necessary to evaluate the extent of any machining induced subsurface features in the upper layers of the microstructure, such as: grain distortion, twinning, residual stress and white layer.

During the machining of Ti-64 Che-Haron [103] attributed tool wear to the increased grain distortion and plastic deformation in the subsurface of the alloy. As the tool wear increased, a thin white layer forms on top of the machined surface. White layer is a feature where the uppermost layer becomes a region of high hardness. The tendency to form white layer during machining has been identified by Xu et al. [104] as the result of plastic deformation and phase transformation, with greater prominence at higher cutting speeds where heat generation in the workpiece is uncontrolled.

Residual stresses in the machined surface are typically tensile in nature [105]. The magnitude of tensile residual stress sharply decreases with the increasing depth of cut. Microstructural alterations and temperature effects are believed to dominate the factors influencing residual stress distribution. Increasing feed rate makes the residual stresses more tensile at the surface. Tool flank wear, increases the tensile stresses due to increased heat generation. Chen et al. [106] investigated this for Ti-64 finding that stresses are mainly compressive in a machined surface when using a fresh unworn tool, though transitioned to tensile stresses as the tool became more worn.

Wang & Liu, [107] found that at lower cutting speeds, the main deformation mode of Ti-64 is slip, with compression twins dominating at higher cutting speeds $\{10\bar{1}1\}$. The higher strain rate imposed on the machined surface reduced the CRSS, thus making it easier to twin. Microstructural features such as slip bands and mechanical twins are inherent features of the plastic deformation process. The incidence of any of these features strongly depends on the type of crystal lattice, the grain's crystallographic orientation and the relative CRSS for basal, prism, or pyramidal slip versus shear stress required for twinning to occur. These features are found to be detrimental during in-service operation and strongly active in the failure mechanisms during fatigue [108], [109].

2.4.2.4 Chip Formation

Chip formation affects machining forces, cutting temperature, tool life and surface integrity of the workpiece. Manageable chip forms are described as those which are short and with tight curls. Less manageable chips on the other hand generally form large nests around the tool edge which can be damaging to the tool, workpiece and the operator. Looking at the influence of cutting parameters on chip formation Komanduri et al. [110] found that increasing the cutting speed induced more thermoplastic instability, - the relationship between thermal softening and work hardening is responsible for forming adiabatic shear bands in the primary shear band. An alloy is considered more machinable than another alloy if it has a wide range of cutting speeds, feeds and depths of cuts which can obtain short curled chips. The adiabatic shear bands are formed in between each chip serration as shown in Figure 2.10 and are characterised by the cyclic forces typical of this type of chip. The adiabatic shear band is a region of plastic deformation which can easily break apart into separate pieces. It is

widely accepted that serrated chips, are associated with shorter tool-chip contact length, and dynamic loading on the cutting tool which can both lead to premature tool failure [111]. The serrated chips according to Groover et al. [112] also negatively affect the surface finish. Another type of common chip type is the continuous chips which are undesirable as they can negatively affect tool life by blocking the coolant flow to the tool- workpiece interface increasing the localised temperature at the tool tip and encouraging formation of BUE on the tool. The BUE can be deposited on the machined surface, risking failure of the component during inspection or damage to the tool [113]. Therefore striking the right balance in chip form is necessary to maximise the life of the tool and surface integrity.

In order to improve the chip breakability chip breakers can be employed. Significant research goes into developing novel breakers which can improve breakability of chips and help to improve productivity. Though the success of chip breakers is through careful implementation of cutting parameters. A feed rate too low, will not make use of the chip breaker geometry. If the feed rate is too high, the chip can become compressed, resulting in high pressure and risk of tool breakage.

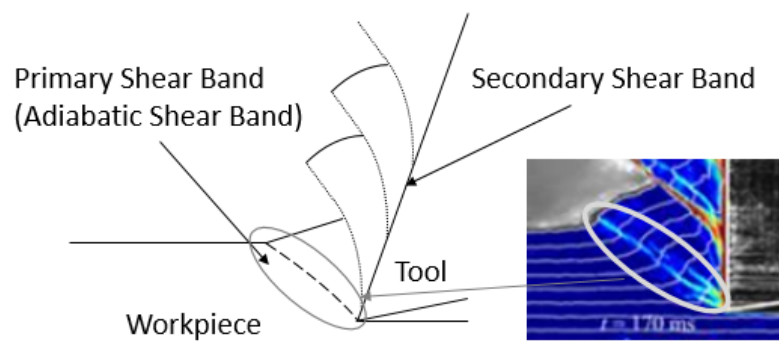


Figure 2.10: Schematic illustration of a serrated chip formation. Redrawn from [114]. Alongside the schematic is an in-situ image showing the formation of the primary shear band [115].

2.5 Small Scale Machining Characteristic Techniques

Various tests have been developed to understand the deformation properties of materials including compression testing equipment such as the split Hopkinson pressure bar (SHPB) and the Arbitrary Strain Path (ASP) test.

The SHPB test was developed for dynamic fracture experiments. It works on the principle of one-dimensional wave propagation. It is typical to analyse the deformation history of the specimen from the signals in the strain gauges mounted on the incident and transmission bars. The SHPB is used to test a range of materials from concrete to metals to observe the dynamic properties of materials at high

strain rates of between 100–2000 s⁻¹ [116]. The limitation of the SHPB is that it is expensive to operate. Sutter [117] attempted to use the SHPB to conduct orthogonal cutting test, by modifying the design by removing the striker bar and replacing it with cutting tool inserts. This method had the advantage of making in-situ imaging possible and being able to produce cutting speeds of between 1020–3600 m.min⁻¹, however came with the disadvantage that it could not facilitate any load measuring capabilities.

Marshall et al. [37] developed the Arbitrary Strain Path (ASP) test to produce a low cost orthogonal cutting rig to obtain cutting performance characteristics of different alloys. The method required two cutting tool inserts and a small sample of 15 x 15 x 50 mm³. The test was limited to a maximum of 6 m.min⁻¹ due to limitations in hydraulic pressure available. But the main issue encountered was reliability and accuracy. In using two cutting inserts it was very difficult to determine the true cutting force for each tool, again reliability producing the same depth of cut on each side of the sample was equally challenging. The method was as such limited and required work to improve accuracy and reliability.

2.6 Timetal 407

In recent years new $\alpha + \beta$ titanium alloys have been developed to reduce manufacturing costs of aerospace components. Ti-0.85Al-3.9V-0.25Si-0.25Fe, (Ti-407) was one such alloy designed for improved manufacturability and energy absorption during fracture. The alloy was developed to replace Ti-64 in applications where energy absorption during fracture and high cycle fatigue (HCF) were important properties [118]. Davey et al. [119] investigated the fatigue performance of Ti-407 finding that the alloy offered superior HCF fatigue strength to Ti-64. The HCF strength was greater than that measured under low cycle fatigue (LCF) loading, suggesting that Ti-407 may be subject to dwell sensitivity. This was confirmed later by Bache et al. [120], who identified the reason was a result of the presence of macro-zones in Ti-407. However this is something which Bache et al. [120] thinks can be improved through an optimised thermo-mechanical processing route to generate a random distribution of α_p grains. The deformation characteristics of Ti-407 were assessed in greater detail by Kloenne et al. [121], through the use of a split Hopkinson pressure bar testing rig. The work demonstrated that $\langle c + a \rangle$ type dislocation slip within the equiaxed grains was present as well as a high density of $\{10\bar{1}2\}$ deformation twins. The $\langle c + a \rangle$ dislocation was an unusual observation as this type of slip observation usually occurs in titanium alloys with an aluminium content greater than 4 wt. %. It was also established to be difficult to achieve catastrophic failure in Ti-407. The absence of such failure was speculated to be due to unstable shear, most likely the effect of the increased deformation along the c-axis. Previous unpublished work on the machining performance of Ti-407 has demonstrated the challenge in controlling chip evacuation, whereby formation of long, nest like chips was common. However the alloy did demonstrate capabilities in machining at higher cutting speeds with reduced tool

wear as well as lower cutting forces compared to Ti-64. The challenge of chip control is correlated to the inability to fracture and raises questions of how best to machine this alloy to enable chip breakage. As there is no published work on this subject it remains for this work to publish findings relating to the machining performance of this new alloy.

2.7 Summary

This chapter presents a review of manufacturing, deformation mechanisms and machinability of titanium alloys. The literature has identified key areas where further research is required. The first being in developing small scale machinability experiments to streamline the development of titanium alloys. Given the great costs of machining, this research has identified a number of more economical, machinability experiments, which could prove crucial in informing industry on a materials machinability. It is the aim of this research to link the outputs from the small scale experiments with machinability outputs from high speed machining. The second area of development is on understanding how can the chip evacuation of Ti-407 be controlled and why chip evacuation is so challenging to control. The literature has highlighted challenges in machining Ti-407 from the conflicting effects during the deformation of the material. Through high speed machining experiments it is the aim of this research to understand what is happening to the material during deformation and identify how chips can be managed. Additionally, it is understood from the literature that machining is sensitive to changing cutting parameters and therefore to improve one machinability output will be to the detriment of another. To date there is no research to bring together all the machinability outputs in a simple map allowing machinists and researchers to visualise the effects of changing parameters on each of the machinability outputs. In order to understand the implications of improving chip control of Ti-407 on other machinability outputs the author aims to produce a machinability map showing the machinability outputs over a range of cutting speeds and feed rates to identify the optimal regions for machining to maximise metal removal rate whilst attaining low costs.

2.8 Experimental Methods and Analysis Techniques

This research employs a variety of experimental methods and a number of different metallographic preparation techniques, optical imagery, scanning electron microscopy (SEM) and electron backscatter diffraction (EBSD). This section details the various procedures used within this research.

2.8.1 Arbitrary Strain Path

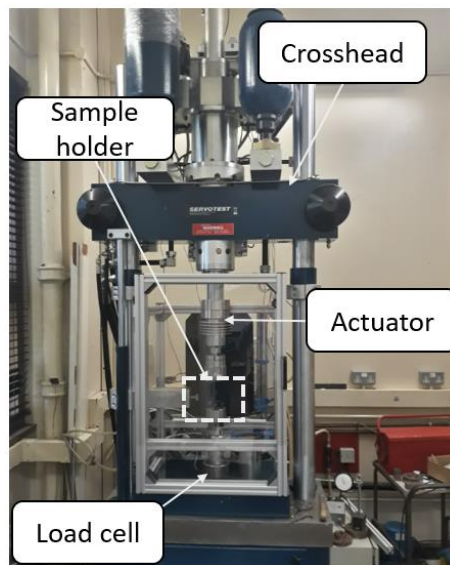


Figure 2.11: Image showing the Arbitrary Strain Path (ASP) used for the small scale orthogonal cutting tests.

The Arbitrary Strain Path (ASP) was used as the small scale orthogonal cutting rig. The ASP has been designed to produce loads in compression, tension or torsion. The ASP consists of a lower tool fixture and a ram driven upper section. The upper section moves vertically providing the compressive capabilities for the orthogonal cutting. The ASP was limited to a tool displacement of 10 mm at a speed of $100 \text{ mm}\cdot\text{s}^{-1}$, up to a load capacity of 100 kN. The linear displacement was measured using a linear variable differential transformer (LVDT) positioned above the upper crosshead. The lower tool was secured to a load cell, which recorded the load exerted on the tool during cutting. The ASP was used to provide data on the chip formation characteristics during cutting as well as surface/ sub-surface deformation and tool life related predictions for different materials.

2.8.2 Thermomechanical Compression Machine

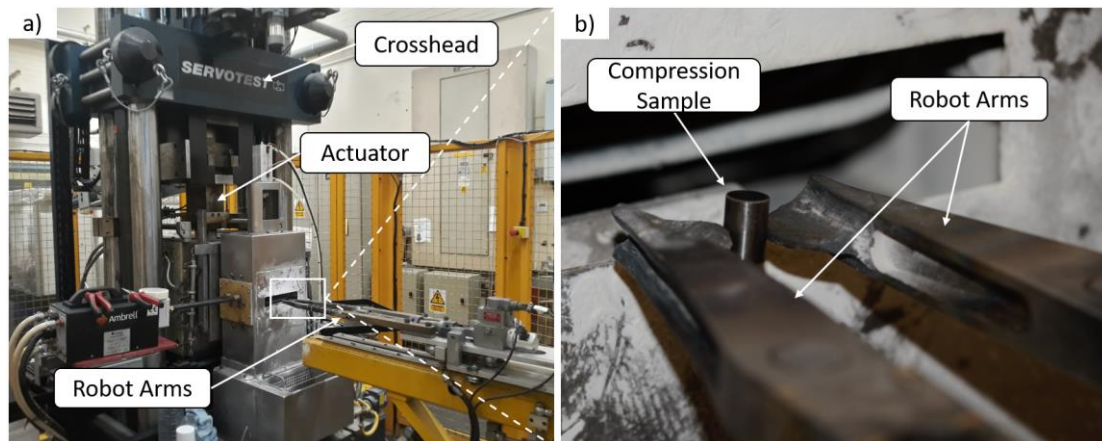


Figure 2.12: a) An image of the Thermomechanical Compression (TMC) machine used during compression testing and b) image of the robot arms holding the compression sample prior to testing

In order to understand the deformation mechanisms and record the flow stress data of the materials investigated in this research, compression samples of a cylinder were conducted using the Thermomechanical Compression (TMC) machine. The TMC consists of an upper and lower tool post. The lower post remained stationary and upper was ram driven. The tests were performed at room temperature and were completed at a range of strain rates: 0.1 s^{-1} , 1 s^{-1} , 10 s^{-1} and 100 s^{-1} , up to a strain of 0.7 mm.mm^{-1} . The cylindrical samples, were 10 mm diameter by 15 mm height, to a tolerance of $\pm 0.1 \text{ mm}$.

2.8.3 Diffusion Couple Experiment



Figure 2.13: An image of the diffusion couple rig used for the diffusion couple experiment.

The diffusion couple experimental rig was utilised for the purpose of investigating the chemical reactivity of a material with a cutting tool. A tool was placed on top of a polished to mirror finish titanium coupon of 20 x 20 x 5 mm with an Inconel weight on top of both to promote intimate contact. The titanium, tool, Inconel “sandwich” was placed inside the vacuum furnace where the chamber was pumped to a pressure of 10^{-5} mbar before being heated slowly at a steady rate of 3°C/min, and held for two hours at 1000°C before being cooled down to room temperature. After the heating process, the titanium alloy and the insert were set in an epoxy resin mould to protect the bond, before being carefully sectioned. Metallographic preparation was conducted again to achieve a mirror finish. The samples were analysed in a scanning electron microscope to reveal the thickness of the chemical diffusion bond.

2.8.4 Finite Element Modelling

Using the flow stress data collected from the TMC compression tests, Finite Element (FE) DEFORMTM software models were produced to make predictions about the chip forming characteristics of each of the materials. For the FE models, it has been typical to use the Johnson Cook (JC) relationship [122], however due to limitations in predicting the adiabatic phenomenon during deformation this research used the Norton Hoff relationship. The Norton Hoff relationship assumes perfect viscoplasticity so is more appropriate for investigating the deformation characteristics of highly ductile materials. It does therefore fail to examine the effect of the elastic behaviour of the material. Further information on the FE models can be found in section 3.3.1.3.

2.8.5 Specimen Preparation

A standard procedure was used to prepare the samples for optical microscopy, SEM and EBSD. These techniques remained the same for both material types investigated. In preparation for microstructure analysis, each sample was individually mounted within a 32 mm diameter conductive bakelite resin mount. This was followed by a three step polishing process as detailed in Table 2.2 using a Struers Tegramin automatic polishing machine.

Table 2.2: Summary of the metallographic preparation steps for titanium alloy

Procedure	SiC Grinding paper/ polishing pad	Medium	Force, N	Plate Speed, RPM	Head Speed, RPM	Rotation	Time, mins	No. of pads
Grinding	P400 grit SiC	Water	20	170	120	Comp	1	1
	P800 grit SiC						1	2
	P1200 grit SiC						0.5	4
	P2500 grit SiC						0.5	4
Polishing	MD-Chem porous neoprene disc from Streuers	0.05 μm colloidal silica, 10% reagent grade H_2O_2	30	170	60	Contra	15	1
Clean	MD-Chem porous neoprene disc from Streuers	0.05 μm colloidal silica, 10% reagent grade H_2O_2	20	170	60	Contra	10	1

2.8.6 Imaging and Analysis

2.8.6.1 Microstructure Optical Imaging

After grinding and polishing, the initial microstructural images were produced using light optical microscopy. A Nikon Eclipse LV150 optical microscope with cross-polarised light filters was used.

2.8.6.2 Scanning Electron Microscope (SEM) and X-EDS

To study microstructural features and to obtain quantitative elemental analysis a Zeiss EVO LS25 SEM was used. This was most valuable for looking at the chemical composition at the interface of the tool workpiece specimens after diffusion couple experiments. The operating parameters have been outlined in Table 2.3.

Table 2.3: Summary of the operating parameters used for the SEM

Parameter	Typical Value
Accelerating Voltage	20KeV
Spot Size	3
Working Distance	9-13 mm
Detector	Backscatter and secondary Electron

2.8.6.3 Electron Backscatter Diffraction (EBSD)

Electron Backscatter Diffraction (EBSD) imaging was employed to reveal the depth of the severe plastic deformation (SPD) by measuring the crystallographic orientation of the α phase in the machined surface, using an FEI Sirion field emission gun scanning electron microscope with a 20 keV accelerating voltage and a step size of 0.1 μm . Automated indexing and post processing of the electron diffraction data was performed using Oxford Instruments HKL Channel 5 software.

References

- [1] C. Leyens and M. Peters, *Titanium and Titanium Alloys*. Wiley-VCH, 2003.
- [2] D. Rugg, M. Dixon, and F. P. E. Dunne, “Effective structural unit size in titanium alloys,” *J. Strain Anal. Eng. Des.*, vol. 42, no. 4, pp. 269–279, May 2007.
- [3] V. Sinha, M. J. Mills, J. C. Williams, and J. E. Spowart, “Observations on the faceted initiation site in the dwell-fatigue tested Ti-6242 alloy: Crystallographic orientation and size effects,” *Metall. Mater. Trans. A*, vol. 37, no. 5, pp. 1507–1518, May 2006.
- [4] Z. Li, J. Li, Y. Zhu, X. Tian, and H. Wang, “Variant selection in laser melting deposited $\alpha + \beta$ titanium alloy,” *J. Alloys Compd.*, vol. 661, pp. 126–135, 2016.
- [5] N. Gey, P. Bocher, E. Uta, L. Germain, and M. Humbert, “Texture and microtexture variations in a near- α titanium forged disk of bimodal microstructure,” *Acta Mater.*, vol. 60, no. 6, pp. 2647–2655, 2012.
- [6] K. Zhang, K. V. Yang, S. Lim, X. Wu, and C. H. J. Davies, “Effect of the presence of macrozones on short crack propagation in forged two-phase titanium alloys,” *Int. J. Fatigue*, vol. 104, pp. 1–11, Nov. 2017.
- [7] T. B. Britton, F. P. E. Dunne, and A. J. Wilkinson, “On the mechanistic basis of deformation at the microscale in hexagonal close-packed metals,” *Proc. R. Soc. A Math. Phys. Eng. Sci.*, vol. 471, no. 2178, 2015.
- [8] D. R. Askeland, P. P. Fulay, and W. J. Wright, *The Science and Engineering of Materials*, Sixth. Global Engineering, 1984.
- [9] E. Levine, “Deformation mechanisms in titanium at low temperatures,” *AIME MET SOC TRANS*, vol. 236, no. 11, pp. 1558–1565, 1966.
- [10] G. Lütjering and J. C. Williams, *Titanium*, 2nd ed. Springer, 2007.
- [11] M. Donachie Jr., *Titanium – A Technical Guide*, 2nd ed. 2000.
- [12] I. J. Polmear, “Titanium alloys,” in *Light Alloys*, Elsevier, 2005, pp. 299–365.
- [13] I. Inagaki, T. Takechi, Y. Shirai, and N. Ariyasu, “Application and Features of Titanium for the Aerospace Industry,” 2014.
- [14] H. M. Flower, “Microstructural development in relation to hot working of titanium alloys,” vol. 6, no. 11, pp. 1082–1092, 1990.
- [15] P. Davies, R. Thomas, P. Garratt, N. Green, M. Coleman, and S. Biroasca, “The Effect of Elevated Temperature Exposure on the Mechanical Properties of Ti834,” in *Proceedings of the*

13th World Conference on Titanium, Hoboken, NJ, USA: John Wiley & Sons, Inc., 2016, pp. 1625–1630.

- [16] D. Tromans, “Elastic Anisotropy of HCP Metal Crystals and Polycrystals,” *Int. J. Res. Rev. Appl. Sci.*, vol. 6, no. 4, pp. 462–483, 2011.
- [17] F. Barlat, O. Cazacu, M. Życzkowski, D. Banabic, and J. W. Yoon, “Yield Surface Plasticity and Anisotropy,” in *Continuum Scale Simulation of Engineering Materials*, Weinheim, FRG: Wiley-VCH Verlag GmbH & Co. KGaA, 2005, pp. 145–183.
- [18] R. V. Mises, “Mechanik der plastischen Formänderung von Kristallen,” *ZAMM - Zeitschrift für Angew. Math. und Mech.*, vol. 8, no. 3, pp. 161–185, 1928.
- [19] W. D. Callister and D. G. Rethwisch, *Materials Science and Engineering: An Introduction*, 8th ed. Wiley, 2009.
- [20] R. Ding, J. Gong, A. J. Wilkinson, and I. P. Jones, “ $\langle c+a \rangle$ Dislocations in deformed Ti–6Al–4V micro-cantilevers,” *Acta Mater.*, vol. 76, pp. 127–134, 2014.
- [21] P. G. Partridge, “The crystallography and deformation modes of hexagonal close-packed metals,” *Metall. Rev.*, vol. 12, no. 1, pp. 169–194, Jan. 1967.
- [22] D. Kuhlmann-Wilsdorf, “Theory of plastic deformation: - properties of low energy dislocation structures,” *Mater. Sci. Eng. A*, vol. 113, pp. 1–41, Jul. 1989.
- [23] D. K. Yang, P. Cizek, P. D. Hodgson, and C. E. Wen, “Microstructure evolution and nanograin formation during shear localization in cold-rolled titanium,” *Acta Mater.*, vol. 58, no. 13, pp. 4536–4548, 2010.
- [24] J. W. Won, D. Kim, S. G. Hong, and C. S. Lee, “Anisotropy in twinning characteristics and texture evolution of rolling textured high purity alpha phase titanium,” *J. Alloys Compd.*, vol. 683, pp. 92–99, 2016.
- [25] M. Arul Kumar, M. Wroński, R. J. McCabe, L. Capolungo, K. Wierzbanski, and C. N. Tomé, “Role of microstructure on twin nucleation and growth in HCP titanium: A statistical study,” *Acta Mater.*, vol. 148, pp. 123–132, 2018.
- [26] O. Engler and V. Randle, *Introduction to Texture Analysis; Macrotecture, microtexture, and orientation mapping*. CRC Press, 2009.
- [27] Y. B. Chun, S. H. Yu, S. L. Semiatin, and S. K. Hwang, “Effect of deformation twinning on microstructure and texture evolution during cold rolling of CP-titanium,” *Mater. Sci. Eng. A*, vol. 398, no. 1, pp. 209–219, 2005.

- [28] A. A. Salem, S. R. Kalidindi, and R. D. Doherty, "Strain hardening of titanium: role of deformation twinning," *Acta Mater.*, vol. 51, no. 14, pp. 4225–4237, Aug. 2003.
- [29] A. A. Salem, S. R. Kalidindi, and R. D. Doherty, "Strain hardening regimes and microstructure evolution during large strain compression of high purity titanium," *Scr. Mater.*, vol. 46, no. 6, pp. 419–423, 2002.
- [30] A. J. Wagoner Johnson, C. W. Bull, K. S. Kumar, and C. L. Briant, "The influence of microstructure and strain rate on the compressive deformation behavior of Ti-6Al-4V," *Metall. Mater. Trans. A*, vol. 34, no. 2, pp. 295–306, Feb. 2003.
- [31] M. Aceves-Lopez, "Subsurface deformation micro-mechanisms induced during machining of titanium alloys at low temperatures, and a new method to examine their machining behaviour," University of Sheffield, 2018.
- [32] H. J. Bunge, "The basic concepts of texture investigation in polycrystalline materials," *Steel Res.*, vol. 62, no. 12, pp. 530–541, Dec. 1991.
- [33] N. P. Gurao, R. Kapoor, and S. Suwas, "Deformation behaviour of commercially pure titanium at extreme strain rates," *Acta Mater.*, vol. 59, no. 9, pp. 3431–3446, 2011.
- [34] R. K. Gupta, C. Mathew, and P. Ramkumar, "Strain Hardening in Aerospace Alloys," *Front. Aerosp. Eng.*, vol. 4, no. 1, pp. 1–13, 2015.
- [35] S. Nemat-Nasser, W. G. Guo, and J. Y. Cheng, "Mechanical properties and deformation mechanisms of a commercially pure titanium," *Acta Mater.*, vol. 47, no. 13, pp. 3705–3720, Oct. 1999.
- [36] H. Becker and W. Pantleon, "Work-hardening stages and deformation mechanism maps during tensile deformation of commercially pure titanium," *Comput. Mater. Sci.*, vol. 76, pp. 52–59, 2013.
- [37] L. Marshall, "The influence of aluminium additions on titanium during machining through the application of a novel orthogonal cutting test method." PhD Thesis, Uni. of Shef., 2014, <https://etheses.whiterose.ac.uk/7352/>
- [38] A. Fitzner, M. Thomas, J. Q. Fonseca, S. Y. Zhang, J. Kelleher, and M. Preuss, "The Effect of Aluminium on Deformation and Twinning in Alpha Titanium: The ND Case," in *Proceedings of the 13th World Conference on Titanium*, Hoboken, NJ, USA: John Wiley & Sons, Inc., 2016, pp. 1051–1055.
- [39] E. O. Hall, "The Deformation and Ageing of Mild Steel: III Discussion of Results," *Proc. Phys. Soc. Sect. B*, vol. 64, no. 9, pp. 747–753, Sep. 1951.
- [40] N. J. Petch and J. Iron, "The cleavage strength of polycrystals," *Steel Inst.*, vol. 173, pp. 25–28, 1953.

- [41] A. Ghaderi and M. R. Barnett, "Sensitivity of deformation twinning to grain size in titanium and magnesium," *Acta Mater.*, vol. 59, no. 20, pp. 7824–7839, Dec. 2011.
- [42] G. A. Salishchev and S. Y. Mironov, "Effect of Grain Size on Mechanical Properties of Commercially Pure Titanium," *Russ. Phys. J.*, vol. 44, no. 6, pp. 596–601, 2001.
- [43] J. A. Venables, "The electron microscopy of deformation twinning," *J. Phys. Chem. Solids*, vol. 25, no. 7, pp. 685–692, 1964.
- [44] A. Rohatgi, K. S. Vecchio, and G. T. Gray, "The influence of stacking fault energy on the mechanical behavior of Cu and Cu-Al alloys: Deformation twinning, work hardening, and dynamic recovery," *Metall. Mater. Trans. A*, vol. 32, no. 1, pp. 135–145, Jan. 2001.
- [45] B. Davis, D. Dabrow, P. Ifju, G. Xiao, S. Y. Liang, and Y. Huang, "Study of the Shear Strain and Shear Strain Rate Progression During Titanium Machining," *J. Manuf. Sci. Eng.*, vol. 140, no. 5, May 2018.
- [46] M. Battaini, "Deformation Behaviour and Twinning Mechanisms of Commercially Pure Titanium Alloys," Monash University, 2008.
- [47] M. Jackson and R. R. Boyer, "Titanium and its Alloys: Processing, Fabrication and Mechanical Performance," *Encycl. Aerosp. Eng.*, vol. 9, no. 6, p. 689, Dec. 2010.
- [48] R. Y. Y. Ma, Q. Xue, H. Wang, S. Huang, J. Qiu, X. Feng, J. Lei, "Deformation Twinning in Fatigue Crack Tip Plastic Zone of Ti-6Al-4V Alloy with Widmanstätten Microstructure," *Mater. Charact.*, vol. 132, pp. 338–347, 2017.
- [49] T. Sugahara et al., "The effect of Widmanstätten and equiaxed microstructures of Ti-6Al-4V on the oxidation rate and creep behavior," *Mater. Sci. Forum*, vol. 636–637, no. June 2014, pp. 657–662, 2010.
- [50] G. Lütjering, "Influence of processing on microstructure and mechanical properties of ($\alpha+\beta$) titanium alloys," *Mater. Sci. Eng. A*, pp. 32–45, 1998.
- [51] J. Lindemann and L. Wagner, "Microtextural effects on mechanical properties of duplex microstructures in ($\alpha+\beta$) titanium alloys," *Mater. Sci. Eng. A*, vol. 263, no. 2, pp. 137–141, May 1999.
- [52] D. Jeong, J. Park, S. Ahn, H. Sung, Y. Kwon, and S. Kim, "Effect of stabilization annealing on SCC susceptibility of β -annealed Ti-6Al-4V alloy in 0.6 M NaCl solution," *Met. Mater. Int.*, vol. 24, no. 1, pp. 101–111, Jan. 2018.
- [53] R. Wanhill and S. Barter, *Fatigue of Beta Processed and Beta Heat-treated Titanium Alloys*. Dordrecht: Springer Netherlands, 2012.

- [54] W. Seo, D. Jeong, D. Lee, H. Sung, Y. Kwon, and S. Kim, "Effects of cooling rate and stabilization annealing on fatigue behavior of β -processed Ti-6Al-4V alloys," *Met. Mater. Int.*, vol. 23, no. 4, pp. 648–659, Jul. 2017.
- [55] M. Armendia, P. Osborne, A. Garay, J. Belloso, S. Turner, and P. Arrazola, "Influence of Heat Treatment on the Machinability of Titanium Alloys," *Mater. Manuf. Process.*, vol. 27, no. 4, pp. 457–461, 2012.
- [56] Y. Kosaka and S. P. Fox, "Influence of alloy chemistry and microstructure on the machinability of titanium alloys," in *Cost-Affordable Titanium: A Symposium Dedicated to Professor Harvey Flower as held at the 2004 TMS Annual Meeting*, 2004, pp. 169–176.
- [57] Y. Kosaka, J. C. Fanning, and S. P. Fox, "Development of low cost high strength alpha/ beta alloy with superior machinability," in *Proceedings of the 10th World Conference on Titanium*, 2004, pp. 3028–3034.
- [58] N. Khanna and K. S. Sangwan, "Machinability analysis of heat treated Ti64, Ti54M and Ti10.2.3 titanium alloys," *Int. J. Precis. Eng. Manuf.*, vol. 14, no. 5, pp. 719–724, May 2013.
- [59] Y. B. Egorova, A. A. Il'in, B. A. Kolachev, V. K. Nosov, and A. M. Mamonov, "Effect of the Structure on the Cutability of Titanium Alloys," *Met. Sci. Heat Treat.*, vol. 45, no. 4, pp. 16–21, 2003.
- [60] S. J. Sun, M. Brandt, and J. P. T. Mo, "Effect of Microstructure on Cutting Force and Chip Formation during Machining of Ti-6Al-4V Alloy," *Adv. Mater. Res.*, vol. 690–693, pp. 2437–2441, May 2013.
- [61] D. Nguyen, D. Kang, T. Bieler, K. Park, and P. Kwon, "Microstructural impact on flank wear during turning of various Ti-6Al-4V alloys," *Wear*, vol. 384–385, pp. 72–83, Aug. 2017.
- [62] D. G. Lee, Y. H. Lee, S. Lee, C. S. Lee, and S. M. Hur, "Dynamic deformation behavior and ballistic impact properties of Ti-6Al-4V alloy having equiaxed and bimodal microstructures," *Metall. Mater. Trans. A*, vol. 35, no. 10, pp. 3103–3112, Oct. 2004.
- [63] D. G. Lee, S. Kim, S. Lee, and C. Soo Lee, "Effects of microstructural morphology on quasi-static and dynamic deformation behavior of Ti-6Al-4V alloy," *Metall. Mater. Trans. A*, vol. 32, no. 2, pp. 315–324, Feb. 2001.
- [64] C. Zheng et al., "Effect of microstructures on ballistic impact property of Ti-6Al-4V targets," *Mater. Sci. Eng. A*, vol. 608, pp. 53–62, Jul. 2014.
- [65] Y. Seo, S. C. Woo, T. W. Kim, and Y. S. Lee, "Influence of heat treated microstructures on the dynamic deformation characteristics of Ti-6Al-4V alloy," *J. Mech. Sci. Technol.*, vol. 29, no. 12, pp. 5223–5232, Dec. 2015.

- [66] A. P. Markopoulos, *Finite Element Method in Machining Processes*. London: Springer London, 2013.
- [67] M. E. Merchant, "Mechanics of the metal cutting process. I. Orthogonal cutting and a type 2 chip," *J. Appl. Phys.*, Vol. 16, no. 5, 1945, <https://doi.org/10.1063/1.1707586>.
- [68] B. Mills and A. H. Redford, *Machinability of Engineering Materials*. Applied Science Publishers, 1983.
- [69] J. P. Davim, *Machinability of Advanced Materials*. Hoboken, NJ, USA: John Wiley & Sons, Inc., 2014.
- [70] G. T. Smith, *Cutting Tool Technology: Industrial Handbook*. 2008.
- [71] F. W. Taylor, "On the art of cutting metals", Book, American Society of Mechanical Engineers, 1906.
- [72] P. J. Arrazola, A. Garay, L. M. Iriarte, M. Armendia, S. Marya, and F. Le Maître, "Machinability of titanium alloys (Ti6Al4V and Ti555.3)," *J. Mater. Process. Technol.*, vol. 209, no. 5, pp. 2223–2230, 2009.
- [73] M. Armendia, A. Garay, L. M. Iriarte, and P. J. Arrazola, "Comparison of the machinabilities of Ti6Al4V and TIMETAL® 54M using uncoated WC–Co tools," *J. Mater. Process. Technol.*, vol. 210, no. 2, pp. 197–203, Jan. 2010.
- [74] R. Lalbondre, P. Krishna, and G. C. Mohankumar, "An Experimental Investigation on Machinability Studies of Steels by Face Turning," *Procedia Mater. Sci.*, vol. 6, pp. 1386–1395, 2014.
- [75] S. I. Jaffery and P. T. Mativenga, "Assessment of the machinability of Ti-6Al-4V alloy using the wear map approach," *Int. J. Adv. Manuf. Technol.*, vol. 40, no. 7–8, pp. 687–696, 2009.
- [76] R. Komanduri and B. F. Von Turkovich, "New observations on the mechanism of chip formation when machining titanium alloys," *Wear*, vol. 69, no. 2, pp. 179–188, Jun. 1981.
- [77] E. O. Ezugwu and Z. M. Wang, "Titanium alloys and their machinability—a review," *J. Mater. Process. Technol.*, vol. 68, no. 3, pp. 262–274, Aug. 1997.
- [78] T. Childs, "Metal Machining Theory and Applications," *Mater. Technol.*, pp. 1–19, 2000.
- [79] O. Hatt, P. Crawforth, and M. Jackson, "On the mechanism of tool crater wear during titanium alloy machining," *Wear*, vol. 374, pp. 15–20, 2017.
- [80] A. Jawaid, C. H. Che-Haron, and A. Abdullah, "Tool wear characteristics in turning of titanium alloy Ti-6246," *J. Mater. Process. Technol.*, vol. 92–93, pp. 329–334, Aug. 1999.

- [81] O. Hatt, H. Larsson, F. Giuliani, P. Crawford, B. Wynne, and M. Jackson, "Predicting Chemical Wear in Machining Titanium Alloys Via a Novel Low Cost Diffusion Couple Method," *Procedia CIRP*, vol. 45, pp. 219–222, 2016.
- [82] C. Ramirez et al., "Understanding the diffusion wear mechanisms of WC-10%Co carbide tools during dry machining of titanium alloys," *Wear*, vol. 390–391, pp. 61–70, Nov. 2017.
- [83] D. Jianxin, L. Yousheng, and S. Wenlong, "Diffusion wear in dry cutting of Ti–6Al–4V with WC/Co carbide tools," *Wear*, vol. 265, no. 11, pp. 1776–1783, 2008.
- [84] E. M. Trent and P. K. Wright, *Metal Cutting*, 4th ed. 1991.
- [85] W. Min, W. Min, and Z. Youzhen, "Diffusion wear in milling titanium alloys," *Mater. Sci. Technol.*, vol. 4, no. 6, pp. 548–553, Jun. 1988.
- [86] N. Tomac, K. Sørby, and S. Doboviček, "Formation of built-up layer on the tool in turning operation of magnesium alloys," *Teh. Vjesn.*, vol. 25, no. 3, pp. 940–943, 2018.
- [87] K. Ohgo, "The adhesion mechanism of the built-up edge and the layer on the rake face of a cutting tool," *Wear*, vol. 51, no. 1, pp. 117–126, 1978.
- [88] A. Hosseini and H. A. Kishawy, "Cutting Tool Materials and Tool Wear," in *Machining of Titanium Alloys*, 2014, pp. 31–56.
- [89] D. Carou and J. P. Davim, *Machining of Light Alloys*. CRC Press, 2018.
- [90] P. A. Dearnley and A. N. Grearson, "Evaluation of principal wear mechanisms of cemented carbides and ceramics used for machining titanium alloy IMI 318," *Mater. Sci. Technol.*, vol. 2, no. 1, pp. 47–58, Jan. 1986.
- [91] N. Narutaki, A. Murakoshi, S. Motonishi, and H. Takeyama, "Study on Machining of Titanium Alloys," *CIRP Ann.*, vol. 32, no. 1, pp. 65–69, Jan. 1983.
- [92] N. Fang and Q. Wu, "A comparative study of the cutting forces in high speed machining of Ti–6Al–4V and Inconel 718 with a round cutting edge tool," *J. Mater. Process. Technol.*, vol. 209, no. 9, pp. 4385–4389, May 2009.
- [93] J. Hou, W. Zhou, H. Duan, G. Yang, H. Xu, and N. Zhao, "Influence of cutting speed on cutting force, flank temperature, and tool wear in end milling of Ti-6Al-4V alloy," *Int. J. Adv. Manuf. Technol.*, vol. 70, no. 9–12, pp. 1835–1845, Feb. 2014.
- [94] S. V. Telrandhe, A. K. Saxena, and S. Mishra, "Effect of microstructure and cutting speed on machining behavior of Ti6Al4V alloy," *J. Mech. Sci. Technol.*, vol. 31, no. 5, pp. 2177–2184, May 2017.

- [95] S. Sun, M. Brandt, and M. S. Dargusch, "Characteristics of cutting forces and chip formation in machining of titanium alloys," *Int. J. Mach. Tools Manuf.*, vol. 49, no.7-8, pp. 561-568, June. 2009.
- [96] C. Gao and L. Zhang, "Effect of cutting conditions on the serrated chip formation in high-speed machining," *Mach. Sci. Technol.*, vol. 17, no. 1, pp. 26–40, Jan. 2013.
- [97] W. P. Koster, M. Field, L. Fritz, L. R. Gatto, and J. F. Kahles, "Surface Integrity of Machined Structural Components," *Technic. Report*, 1970, <https://apps.dtic.mil/sti/citations/AD0870146>
- [98] S. Ramesh, L. Karunamoorthy, and K. Palanikumar, "Surface Roughness Analysis in Machining of Titanium Alloy," *Mater. Manuf. Process.*, vol. 23, no. 2, pp. 174–181, Jan. 2008.
- [99] A. Polishetty, M. Shunmugavel, M. Goldberg, G. Littlefair, and R. K. Singh, "Cutting Force and Surface Finish Analysis of Machining Additive Manufactured Titanium Alloy Ti-6Al-4V," *Procedia Manuf.*, vol. 7, pp. 284–289, Jan. 2017.
- [100] F. Wang, J. Zhao, A. Li, and J. Zhao, "Experimental Study on Cutting Forces and Surface Integrity in High-Speed Side Milling of Ti-6Al-4V Titanium Alloy," *Mach. Sci. Technol.*, vol. 18, no. 3, pp. 448–463, Jul. 2014.
- [101] C. H. Che-Haron and A. Jawaid, "The effect of machining on surface integrity of titanium alloy Ti-6% Al-4% v," *J. Mater. Process. Technol.*, vol. 166, no. 2, pp. 188-192, Aug. 2005.
- [102] A. Ginting and M. Nouari, "Surface integrity of dry machined titanium alloys," *Int. J. Mach. Tools Manuf.*, vol. 49, no. 3–4, pp. 325–332, Mar. 2009.
- [103] C. H. Che-Haron, "Tool life and surface integrity in turning titanium alloy," *J. Mater. Process. Technol.*, vol. 118, no. 1–3, pp. 231–237, Dec. 2001.
- [104] Y. Xu, J. Zhang, Y. Bai, and M. A. Meyers, "Shear Localization in Dynamic Deformation: Microstructural Evolution," *Metall. Mater. Trans. A*, vol. 39, no. 4, pp. 811–843, Apr. 2008.
- [105] T. Özel and D. Ulutan, "Prediction of machining induced residual stresses in turning of titanium and nickel based alloys with experiments and finite element simulations," *CIRP Ann.*, vol. 61, no. 1, pp. 547–550, Jan. 2012.
- [106] L. Chen, T. I. El-Wardany, and W. C. Harris, "Modelling the Effects of Flank Wear Land and Chip Formation on Residual Stresses," *CIRP Ann.*, vol. 53, no. 1, pp. 95–98, Jan. 2004.
- [107] Q. Wang and Z. Liu, "Plastic deformation induced nano-scale twins in Ti-6Al-4V machined surface with high speed machining," *Mater. Sci. Eng. A*, vol. 675, pp. 271–279, Oct. 2016.
- [108] R. Reed-Hill and R. Abbaschian, *Physical Metallurgy Principles*, 3rd ed. Boston: International Thomson Publishing, 1994.

- [109] Z. W. Wyatt, W. J. Joost, D. Zhu, and S. Ankem, "Deformation mechanisms and kinetics of time-dependent twinning in an α -titanium alloy," *Int. J. Plast.*, vol. 39, pp. 119–131, Dec. 2012.
- [110] R. Komanduri and Z. Hou, "On Thermoplastic Shear Instability in the Machining of a Titanium Alloy (Ti-6Al-4V)," *Metall. Mater. Trans. A*, vol. 33, no. 9, pp. 1–16, 2002.
- [111] S. A. Niknam, R. Khettabi, and V. Songmene, "Machinability and Machining of Titanium Alloys: A Review," in *Materials Forming, Machining and Tribology*, 2014, pp. 1–30.
- [112] M. Groover, *Fundamentals of Modern Manufacturing Materials, Processes and Systems*, 4th Editio. John Wiley & Sons Inc, 2011.
- [113] J. G. Schneider, "Cutting Tool Applications," Book, ISBN-10: 0615121918, 2002.
- [114] S. H. Rhim and S. I. Oh, "Prediction of serrated chip formation in metal cutting process with new flow stress model for AISI 1045 steel," *J. Mater. Process. Technol.*, vol. 171, no. 3, pp. 417–422, Feb. 2006.
- [115] K. Viswanathan, S. Yadav and D. Sagapuram, "Shear bands in materials processing: Understanding the mechanics of flow localization from Zener's time to the present," *Appl. Mech. Rev.*, vol. 72, no.6, pp. 17, Jan. 2021.
- [116] A. Kara, A. Tasdemirci, and M. Guden, "Modeling quasi-static and high strain rate deformation and failure behavior of a (± 45) symmetric E-glass/polyester composite under compressive loading," *Mater. Des.*, vol. 49, pp. 566–574, Aug. 2013.
- [117] G. Sutter, "Chip geometries during high-speed machining for orthogonal cutting conditions," *Int. J. Mach. Tools Manuf.*, vol. 45, no. 6, pp. 719–726, 2005.
- [118] S. James, Y. Kosaka, R. Thomas, and P. Garratt, "Timetal® 407: A Titanium Alloy to Enable Cost Reduction," in *Proceedings of the 13th World Conference on Titanium*, 2016, pp. 721–725.
- [119] W. Davey, M. Bache, H. Davies, and M. Thomas, "Fatigue Performance of the Novel Titanium Alloy Timetal 407," *MATEC Web Conf.*, vol. 165, p. 4001, May 2018.
- [120] M. Bache, H. Davies, W. Davey, M. Thomas, and I. Berment-Parr, "Microstructural Control of Fatigue Behaviour in a Novel alpha+beta Titanium Alloy," *Metals (Basel)*, vol. 9, no. 11, p. 1200, Nov. 2019.
- [121] Z. Kloenne, G. Viswanathan, M. Thomas, M. Loretto, and H. Fraser, "A Comparative Study on the Substructure Evolution and Mechanical Properties of TIMETAL 407 and Ti-64," in *The 14th World Conference on Titanium Proceedings*, 2019, pp. 1–6.

- [122] Johnson GR, Cook WH. Fracture characteristics of three metals subjected to various strains, strain rates, temperatures and pressures. *Eng Fract Mech* 1985; 21: 31–48.

3.1 Introduction

There is an increasing drive to exploit the desirable properties of titanium alloys in the petrochemical, biomedical and aerospace industries [1]. However, developing titanium alloys is an expensive process where the requirements are not only to meet strict mechanical properties but also a level of acceptable machinability to maintain economic viability. Titanium alloys are known for their inherently poor machinability properties which can contribute up to 60% of a titanium component's final cost [2]. The conventional approach to assess an alloy's machinability is time consuming and heavily material and machine intensive, thus expensive.

For the machining of titanium alloys, cutting tool manufacturers recommend WC-Co tools which can vary in composition, grain size and coating. Understanding the complex relationship between the cutting tool and workpiece is imperative, when considering that different titanium alloys, ranging from the commercially pure (CP) alpha to metastable β type alloys, exhibit markedly different machinability characteristics [3]. In terms of tool wear, the onset of crater wear is much more rapid for β rich alloys than for near α titanium alloys.

Recent benchtop diffusion couple studies have offered valuable insight into the complexities of titanium alloy machining [4, 5]. They also provide a better understanding into the thermodynamic driving forces and mechanisms occurring at the tool-chip interface prior to carrying out costly machining trials. In order to further support alloy development, finite element (FE) modelling is widely used as a tool for predicting material response in large scale deformation operations such as machining, which typically apply the Johnson Cook (JC) relationship [6]. Yet, in order for this to be applied to emerging alloys, reliable parameters need to be obtained. Furthermore, even for established titanium alloys, such as Ti-6Al-4V (Ti-64), these parameters can vary hugely as demonstrated in Figure 3.1 depending on the starting microstructure and condition of the alloy.

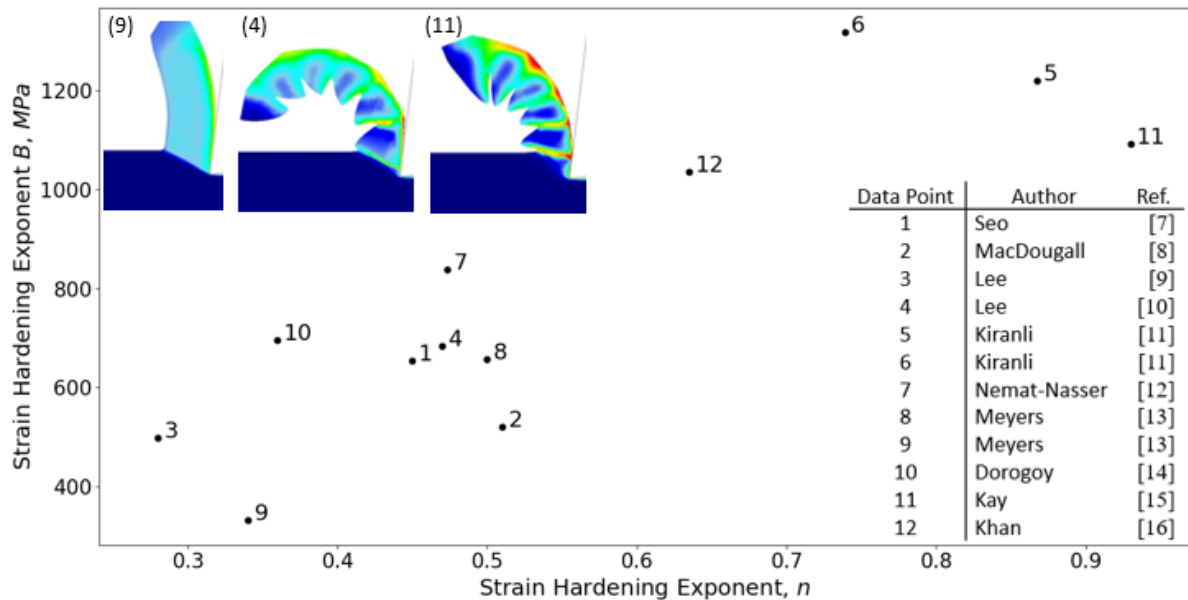


Figure 3.1: Plot showing the combinations of the Johnson-Cook strain hardening parameters, B and n along with the associated chip morphologies from finite element models reported in the literature.

The reported strain hardening characteristics for Ti-64 range from close to perfectly-plastic in nature, [13] to that approaching linear hardening [15]. This results in a change in the chip characteristics from continuous to fully serrated; meaning that obtaining accurate material parameters to represent the microstructural condition is crucial. This further supports the need for a rapid, small scale, testing approach, designed to screen emerging titanium alloy compositions and conditions at an early stage, to inform the FE models, similar to how a microhardness test is used to quantify the resistance of a material to plastic deformation.

A review of the literature reveals two methods for obtaining the material modelling parameters. The first method uses orthogonal cutting to obtain key chip characteristics which are inputted into predictive models to obtain the flow stress data. Oxley [17] was one of the first researchers to suggest this method to obtain flow stress data, using an analytical model to predict the high strains, high strain rates and high temperatures encountered in machining using parallel sided shear zone theory. Subsequently, authors have used this methodology: Shatla et al. [18] used Oxley's theory to model orthogonal milling. They identified the JC material parameters by inverse analysis and demonstrated applicability in numerous alloys. Molinari et al. [19] presented analysis for the development of adiabatic shear bands from orthogonal cutting of Ti-64, across a range of cutting speeds from 0.01 to 73.0 m.s⁻¹. This work was later used by Miguélez et al. [20, 21] to develop an FE model of the chip forming process and of the residual stresses produced during orthogonal cutting based on the JC model. Bai et al. [22] offered a chip forming model but used the Calamaz-modified JC model, again based on orthogonal cutting data. Zhou et al. [23] also developed their own FE model using a modified JC model for cutting titanium alloy Ti-6Al-4V, to improve the accuracy of predicted cutting forces and chip formation. Nasr et al. [24] investigated the effects of workpiece thermal properties on machining induced residual

stresses through the use of FE modelling. Cotterell & Byrne. [25, 26] utilized a high speed camera during orthogonal cutting to rapidly obtain key chip characteristics, however practicalities such as imaging frame rate and accessibility provided challenges for this technique. Laakso & Niemi [27] presented their work on determining the material model parameters from orthogonal cutting experiments, however they advised that compression tests should be used in conjunction with cutting experiments as they offer the ability to change the key variables, strain, strain rate and temperature independently.

An early test by Hastings et al. [28] used high speed compression tests to predict a material's machining characteristics, including chip form and cutting forces. Since then the Split Hopkinson pressure bar test has been used to produce simple flow stress curves at different temperatures, strains and strain rates to generate accurate and reliable material data for the JC model [9, 29–32]. These tests have often been complimented with orthogonal cutting experiments to validate the finite element simulation results, with significant focus aimed at accurately describing the chip geometries and cutting forces. However, up until now the literature has not discussed machinability more broadly in conjunction with uniaxial compression tests.

This work proposes a novel low-cost methodology utilising the Arbitrary Strain Path (ASP) test rig in Figure 3.2a, produced by Servotest and developed at the University of Sheffield. The ASP produces a uniaxial load which lowers a test piece towards a bespoke tooling fixture to create an orthogonal cut. The small scale orthogonal cutting test developed in this work was based upon an approach by Sutter [33], however the limitation of their work was that no load data could be recorded.

The testing method has been designed to inform the manufacturing supply chain of material data at an early stage in the alloy design process. It can provide information on mechanical data and machinability data from just a small volume of material. At the very early development phase, new alloy compositions are vacuum arc melted into small ingot < 300 g 'buttons' prior to partial forging, and hot rolled into approx. 200 mm long bars for testing and analysis. The use of the ASP small-scale testing approach was developed (with the titanium machining supply chain) in order to rapidly assess the machinability of such early stage compositions. This paper demonstrates that machinability with respect to chip formation, subsurface damage, tool wear and force data is typical of what could be expected during large scale machinability experiments.

3.2 Methodology

3.2.1 Small Scale Orthogonal Cutting

As-forged Ti-6Al-4V (Ti-64) and Ti-3.9V-0.25Fe-0.85Al (Ti-407) billet material was supplied by TIMET UK of diameter 225 mm. The material was subsequently wire electrical discharge machined (EDM) from the centre of the cross-section of the billet to the dimensions of 60 x 20 x 20 mm. Following

this the Ti-64 was put through a mill annealed (MA) treatment and the Ti-407 was solution treated and aged (STA). The mediums for solution treatment included air, oil and water, to generate different cooling rates, and therefore specific microstructures and α/β morphologies for each alloy. The microstructures for each of the heat treatments are shown in Figure 3.3. The test pieces were machined again to a final geometry of 50 x 15 x 15 mm. The lower 30 mm of the samples were machined to a ‘cross’ geometry with each section of the ‘cross’ profile being machined to a width of 4 mm, as shown in Figure 3.4. The bespoke insert holder was designed to clamp Seco Tools SNMA150616- MR9 cutting inserts. A square insert was used for two reasons; firstly, for the ease of manufacturing a bespoke tool holder as a proof of concept for using the ASP as part of the methodology, and secondly to handle the high forces exerted on the tool edge. The insert material was uncoated (WC-6% Co) tungsten carbide substrate with a cobalt binder phase. The orthogonal set-up comprised of a negative 6° rake angle, as illustrated in Figure 3.2c. The tests were performed at a constant speed of $6.0 \text{ m}\cdot\text{min}^{-1}$ with an uncut chip thickness of 0.3 mm which was measured to within 10% of the expected value using a digital gauge indicator. The maximum cutting speed was limited by the available pressure in the pumps to move the actuators in a single cut. The length of the cut was 10 mm. In order to improve the design from the previous work by Marshall et al. [34], it was necessary to firstly use only a single tool insert rather than the two used by Marshall. This raised issues of deflection of both the tool and the workpiece sample. To address the deflection of the workpiece, the cross shaped geometry was developed which reduced the load on the tool by nearly 75%, by minimizing the volume of material being cut by the tool. To minimise the deflection of the tool, the tool was bolted into place.

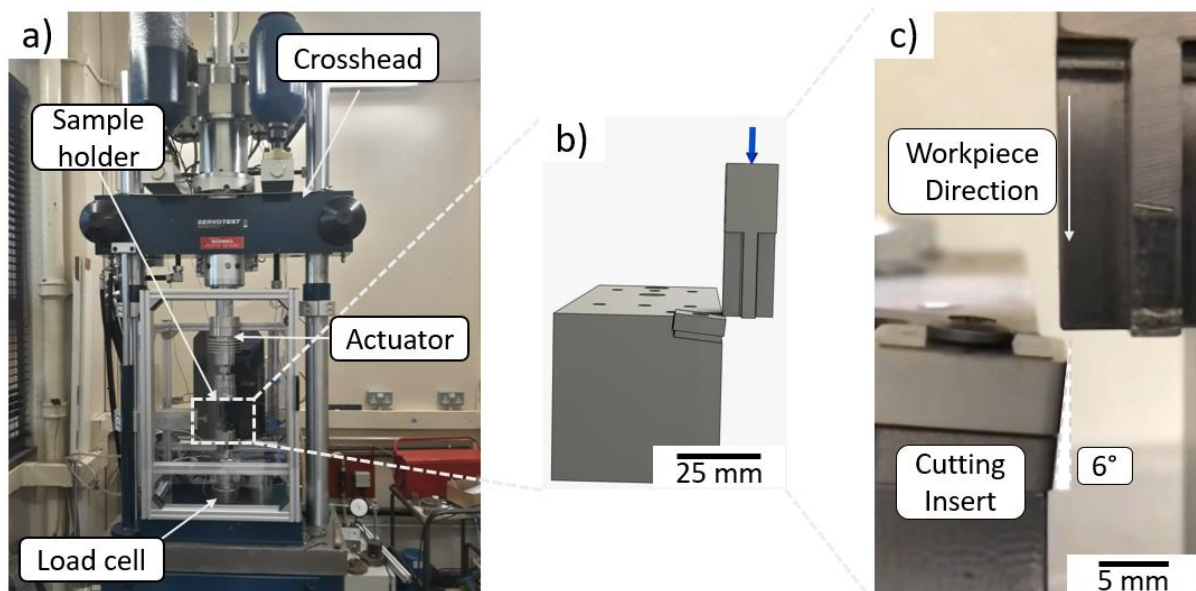


Figure 3.2: a) Photograph of the ASP rig used for the small scale cutting experiments, b) 3D model of the tool holder designed and developed using Autodesk and c) a photograph showing the negative 6° rake angle between the workpiece and the cutting insert.

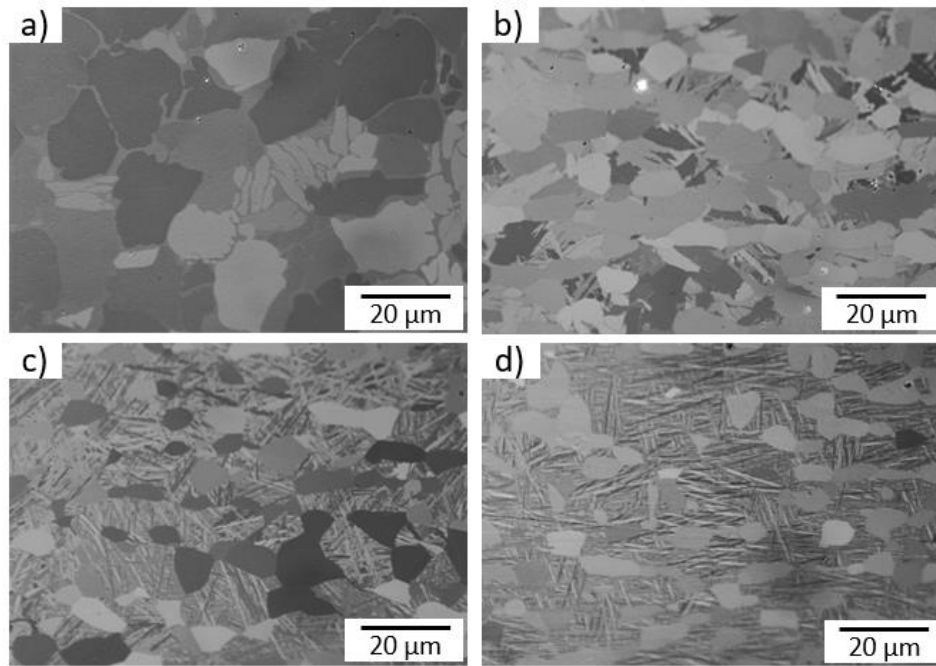


Figure 3.3: Micrographs of the titanium alloy test pieces used in this work post heat treatment, a) Ti-64 MA, b) Ti-407 STA Air Cooled, c) Ti-407 STA Oil Quenched and d) Ti-407 STA Water Quenched.

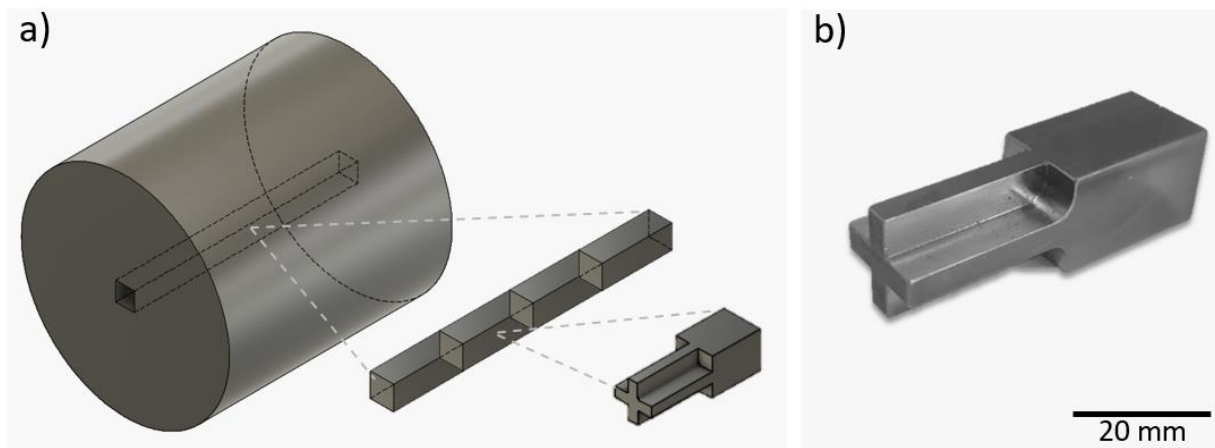


Figure 3.4: a) Location of and geometry of the test samples used for the small scale orthogonal cutting tests and b) a photograph of the sample used for the small scale orthogonal cutting test.

3.2.2 Diffusion Couple Experiment

The diffusion couple method consists of a titanium alloy coupon of size 20 x 20 mm sat underneath an uncoated (WC-6% Co) tungsten carbide, Seco Tools SNMA150616- MR9 insert, with an Inconel weight placed on top to provide pressure. Prior to testing, the titanium alloy test pieces were

polished to a mirror finish using conventional methods and ultrasonically cleaned in isopropanol. The test piece, tool and nickel weight stack were placed on a ceramic cradle inside the vacuum furnace. The chamber was pumped to a pressure of 10^{-5} mbar. Following this, the furnace was heated slowly at a steady rate of $3^{\circ}\text{C}/\text{min}$, and held for two hours at 1000°C before being cooled down to room temperature. After the heating process, the titanium alloy and the insert were set in an epoxy resin mold to protect the bond, before being carefully sectioned. Metallographic preparation was conducted again to achieve a mirror finish. The samples were analyzed in a scanning electron microscope to reveal the thickness of the chemical diffusion bond. This work is a continuation of previous studies conducted by Hatt et al. [4, 5, 35].

3.2.3 Large Scale Cutting Trials

To validate the small scale methodology, industrial scale machining tests were also conducted on the same alloy conditions and some commonalities between the tests have been highlighted. Turning operations were conducted on a DMG Mori NLX 2500 CNC machine turning centre at the University of Sheffield's, Advanced Manufacturing Research Centre (AMRC), with an experimental setup as shown in Figure 3.5. Cutting tools used were WC-6% Co, TNMG160408-MF1, uncoated inserts. The inserts used in the industrial cutting trials are not identical in shape to the small scale orthogonal cutting inserts, however they are of the same substrate grade, so the machining characteristics of both alloys should be representative, irrespective of the tool. A PTJNL2525M16 tool holder was modified by wire EDM to offset tool angles back to orthogonal and like the small scale cutting trials maintain a negative 6° rake angle. An outer ring of width 4 mm was grooved out using an internal grooving tool and an LCMF160608-0600-FT insert with a CP500 coating. The width of the region used for the orthogonal machining tests was measured to $4\text{ mm} \pm 0.05\text{ mm}$ using a ball micrometer as illustrated in Figure 3.6.



Figure 3.5: Photograph showing the setup for the industrial machining trials. Using a disk of material held inside a CNC machining centre; the cutting insert held into a dynamometer to record the cutting forces and the coolant provided through an external pipe.

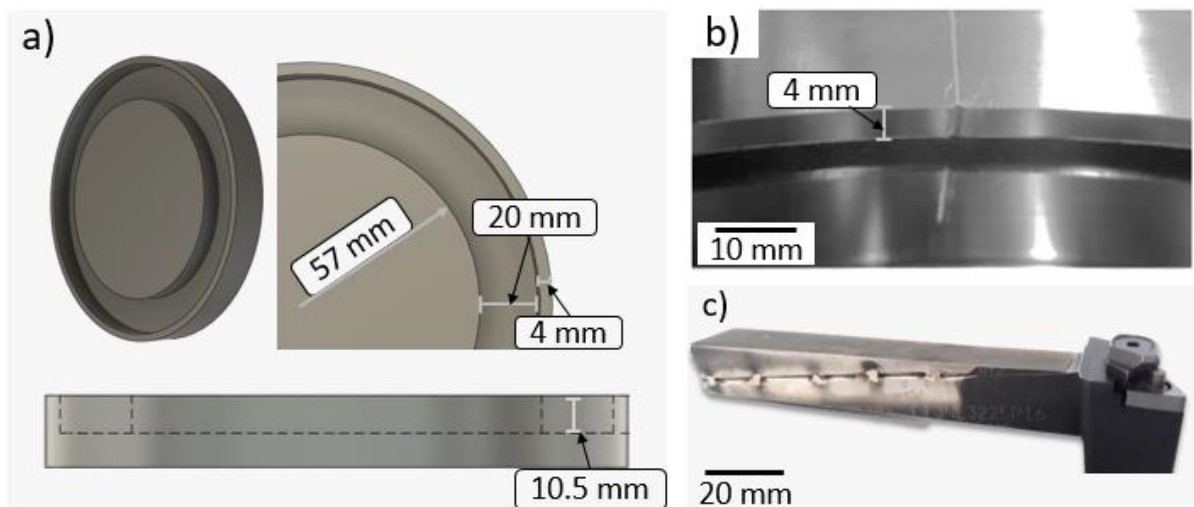


Figure 3.6: a) 3D CAD illustration of the workpiece after grooving the disk to form a 4 mm wide ring for orthogonal machining trials, b) Photograph of the 4 mm wide ring for orthogonal cutting trials and c) photograph of the modified tool holder, Wire EDM'd to meet the requirements for orthogonal machining.

3.3 Results and Discussion

3.3.1 Chip Formation

3.3.1.1 Uniaxial Compression- Analysis of the Deformation Characteristics for Ti-64 and Ti-407

Room temperature uniaxial compression tests were performed at four strain rates ranging from 0.1-100 s⁻¹. Figure 3.7 contains a series of flow stress graphs for strain rate tests of 0.1, 1.0 and 10 s⁻¹. The measurement frequency was too low to measure 100 s⁻¹, so the flow stress data has not been presented.

Figure 3.7 shows that the test samples fractured in all of the tests at strain rates 0.1 s⁻¹ and 10 s⁻¹, except for the Ti-407 oil quenched at a strain rate of 1.0 s⁻¹. Without further testing at higher strains, this cannot be explained, although the Ti-407 oil quenched sample did show signs of plastic instability and imminent failure due to intense shear band in the macrostructure. Nevertheless, the main point from Figure 3.7 is that the observed trends between strain rates and conditions are in strong agreement. The Ti-64 accommodated less strain than Ti-407 at all strain rates tested. The maximum measured stress was higher in Ti-64 than Ti-407 across all strain rates, this agrees with our knowledge of the two alloys from Ref [36], that Ti-64 is a stronger alloy, so can accommodate greater stress at the point of fracture. The area under the curves, presented in Table 3.1, is a good approximation of the toughness and work done prior to fracture of the alloys. At the strain rate of 0.1 s⁻¹, the Ti-407 water quenched test sample has a lower toughness compared to the Ti-407 air cooled one, however increasing the strain rate to 10 s⁻¹, the reverse trend is observed. Cross sections of the test samples in Figure 3.8 compliment the results displayed in Figure 3.7 and Table 3.1, to document the level of fracture of Ti-64 compared to the ductile behavior of Ti-407. Comparing the Ti-407 STA processed through different solution treatment mediums, the process of oil quenching greatly enhanced the toughness of the Ti-407 alloy; accommodating a greater amount of strain before fracture.

As Ti-407 was developed as an alloy to replace Ti-64 in applications where energy absorption during fracture is a primary design consideration [36] it is expected that the alloy exhibits higher toughness through accommodating greater strain than Ti-64. From these results the relative chip forming characteristics of Ti-64 and Ti-407 can be predicted.

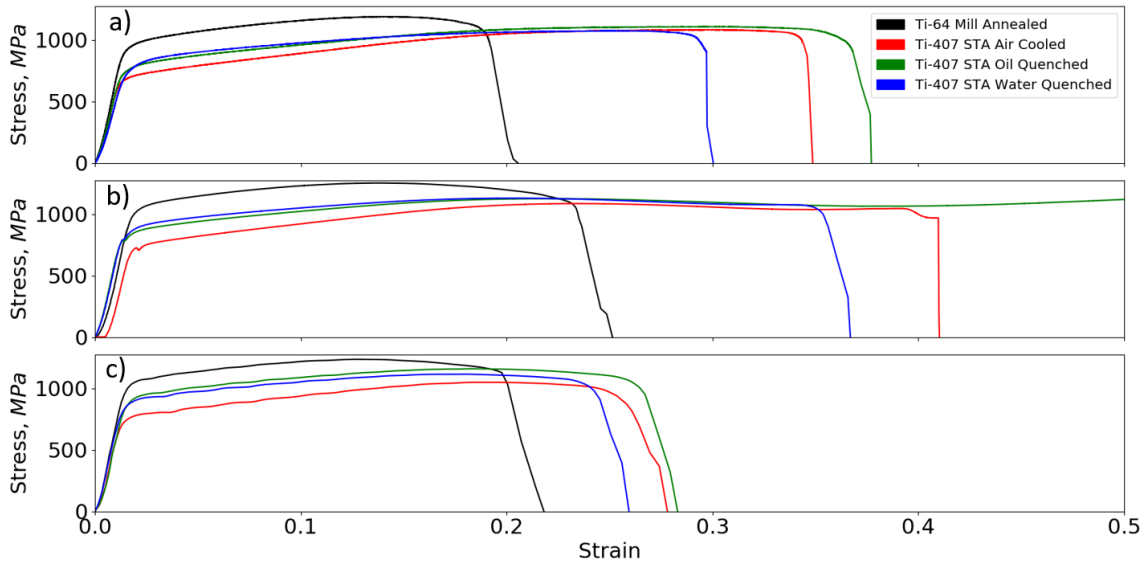


Figure 3.7: Flow stress curves produced from the uniaxial compression tests at strain rates of a) 0.1 s^{-1} , b) 1.0 s^{-1} and c) 10 s^{-1} .

Table 3.1: Comparison of the toughness of each titanium alloy, measured as the area under the flow stress curve.

Strain Rate, s^{-1}		Ti-64 MA	Ti-407 STA Air Cooled	Ti-407 STA Oil Quenched	Ti-407 STA Water Quenched
Toughness, $\text{J}\cdot\text{m}^{-3}$	0.1	210	329	373	288
	1.0	277	403	740*	381
	10	234	249	289	256

*Area under the curve calculated at a strain of $0.7 \text{ mm}\cdot\text{mm}^{-1}$

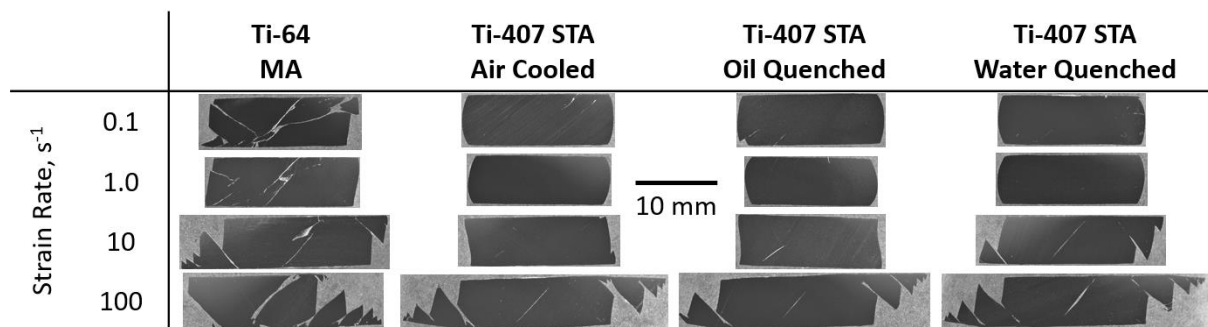


Figure 3.8: Map of photographs showing the cross-section of the titanium alloys, from a strain rate of $0.1 - 100 \text{ s}^{-1}$, after testing has been completed.

3.3.1.2 Comparison of Ti-64 and Ti-407 propensity for mechanical twinning

It is very well cited that during deformation of titanium alloys, mechanical twins can propagate extensively through the material to accommodate strain where the ability to slip is limited. As an important deformation characteristic mechanical twinning has a bearing on both the ability to form and create breakable chips as well as determine the depth to which deformation occurs in the machined surface.

Marshall et al. [37] and Salem et al. [38, 39] had previously conducted research investigating mechanical twinning during deformation of titanium alloys. In both studies the density of mechanical twins in an alloy during deformation was quantified using the normalised strain-hardening rate curve constructed from flow stress data.

Salem et al. [38, 39] had shown that three regions of strain hardening existed during simple compression: Stage I corresponds to falling strain hardening rates; stage II correlates to the initiation of mechanical twins in the microstructure and stage III is associated with saturation in the twin volume fraction. A higher strain hardening rate at the peak of stage II, indicates a much higher twin density.

Figure 3.9 shows the strain-hardening rate curves of the alloys used in this study, which have been normalised by the shear modulus. The shear modulus was calculated from the linear portion of the flow stress curve of each alloy. The transition between Region I and Region II are comparable to those recorded by Salem et al. [38]. Ti-407 has a higher Region II peak than Ti-64, indicating that Ti-407 accommodates strain through a greater propensity to form mechanical twins than Ti-64. The Ti-407 oil quenched has the highest and the water quenched has the lowest mechanical twin density. These results indicate that the mechanical twinning could be responsible for the increased strain achieved at the point of failure for the Ti-407 oil quenched, which ultimately will be detrimental to the chip breaking ability of the alloy. It would be expected that the Ti-407 water quenched sample should be the most likely to form a breakable chip.

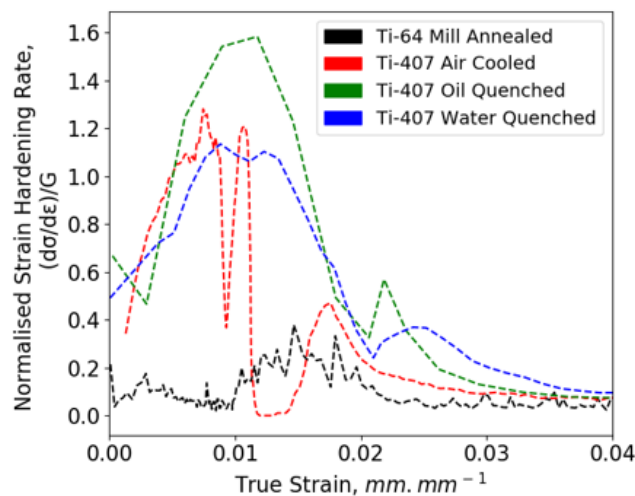


Figure 3.9: Curve of normalised strain hardening rate against true strain, calculated from flow stress data, which was determined from compression tests of Ti-64 and Ti-407 at a strain rate of $1.0 s^{-1}$.

3.3.1.3 FE Model- Development of the FE Model to predict the Chip Formation of Titanium Alloys in each Microstructural Condition

Table 3.2: Norton Hoff Model Material Parameters from flow stress curves at a strain rate of 0.1 s^{-1} . C-L Refers to Cockroft-Latham Damage Criterion

	Ti-64 MA	Ti-407 STA Air Cooled	Ti-407 STA Oil Quenched	Ti-407 STA Water Quenched
k	870	620	620	625
m	0.01	0.01	0.01	0.01
n	0.6	0.85	0.62	0.8
β	140	140	165	200
ϵ_0	0.65	0.65	0.65	0.65
C-L	200	249.8	412.6	261.8
Softening, %	10	10	10	10

The flow stress data from the compression tests at a strain rate of 0.1 s^{-1} was used to develop a DEFORMTM [40] model to predict the relative strain and chip form for room temperature orthogonal cutting tests of these alloys. The model makes some assumptions including; (1) a rigid-viscoplastic workpiece and (2) a rigid tool. The Norton-Hoff model, shown in Equation 3.1 was used for this study, as the JC model exhibits a flow stress increase with increasing strain at any temperature. Researchers [41, 42] have confirmed that the JC model cannot predict the adiabatic phenomenon responsible for the segmented chip formation as the thermal softening effects are not taken into account. The Norton Hoff equation assumes perfect viscoplasticity, therefore it fails to examine the effect of the elastic behaviour of the material. Cockroft-Latham (C-L) [43] was used for the damage criterion model in order to obtain a segmented chip geometry.

$$\sigma = K \epsilon^n \dot{\epsilon}^m \left(\frac{Q}{RT} \right) \quad \text{Equation 3.1}$$

Where K is a constant, n is the strain-hardening exponent, m is the strain rate sensitivity parameter, Q the activation energy, R the ideal gas constant and T the temperature. To obtain the K, n, m and Q/R parameters, a multiple linear regression was used. With the material parameters from Table 3.2, a simple 2D uniaxial compression test was simulated using DEFORMTM, with the results presented in Figure 3.10. The C-L damage criterion was measured at the point at which fracture occurred in the compression tests. The model agrees with the experimental compression tests, showing that at the point of fracture, the effective strain is lower in Ti-64 than in Ti-407. The effective strain for the oil quenched model was over double that of Ti-64. This means that more strain has to be accommodated in the

material for fracturing of the chip to occur. Comparing Figure 3.10 with the toughness values in Table 3.1, it is evident that the larger compression and higher strain values in the FE compression models of Figure 3.10 are validation of the enhanced toughness of the Ti-407 compared to Ti-64. The ability of a material to plastically deform to higher strains prior to fracture, is a key property of an alloy designed to absorb significant loads before fracturing, however this indicates that the machined chip form will be inherently more ductile in such an alloy.

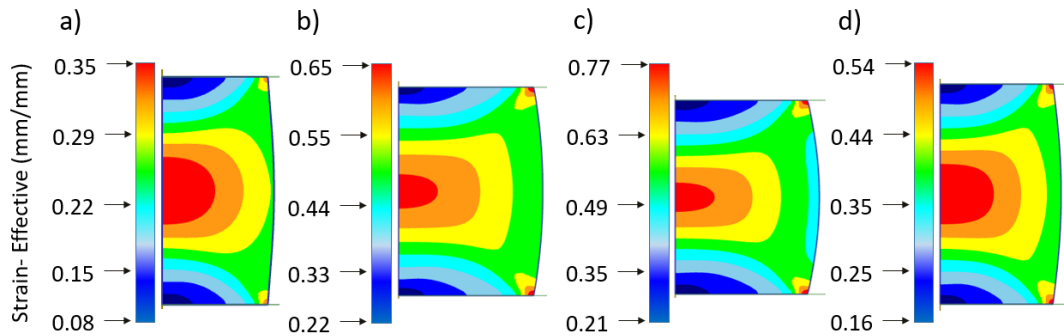


Figure 3.10: DEFORM™ compression simulations showing the effective strain across the cross section of the test pieces at the point of fracture at a strain rate of 0.1 s^{-1} . The material data used is as shown in Table 3.2. a) Ti-64 MA, b) Ti-407 STA Air Cooled, c) Ti-407 STA Oil Quenched and d) Ti-407 STA Water Quenched.

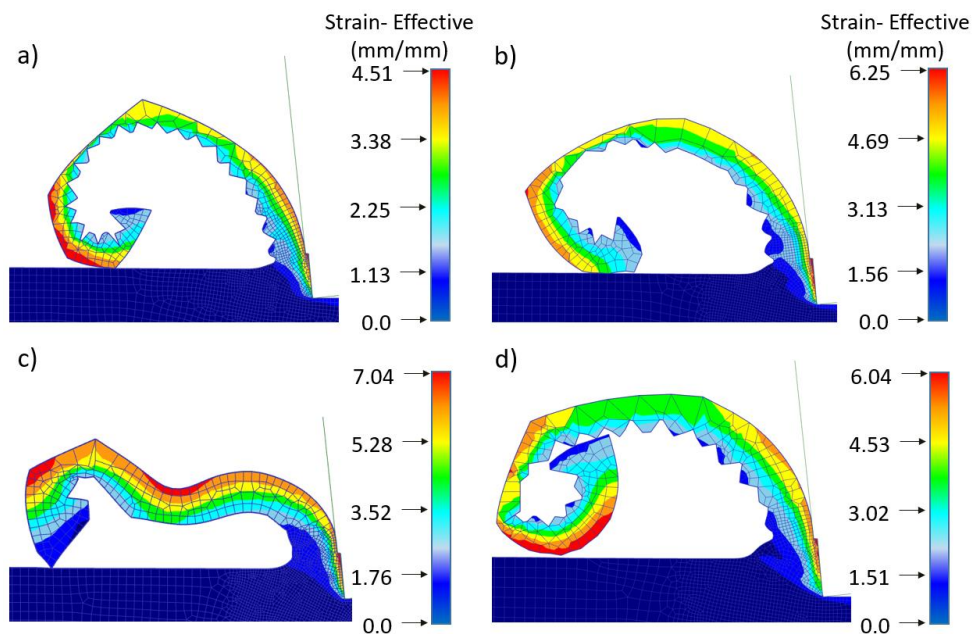


Figure 3.11: DEFORM™ orthogonal 2D simulations showing the chip forming characteristics for each of the corresponding alloys based on material data modelled in the DEFORM™ compression simulations at a cutting speed of $6.0 \text{ m} \cdot \text{min}^{-1}$. a) Ti-64 MA, b) Ti-407 STA Air Cooled, c) Ti-407 STA Oil Quenched and d) Ti-407 STA Water Quenched.

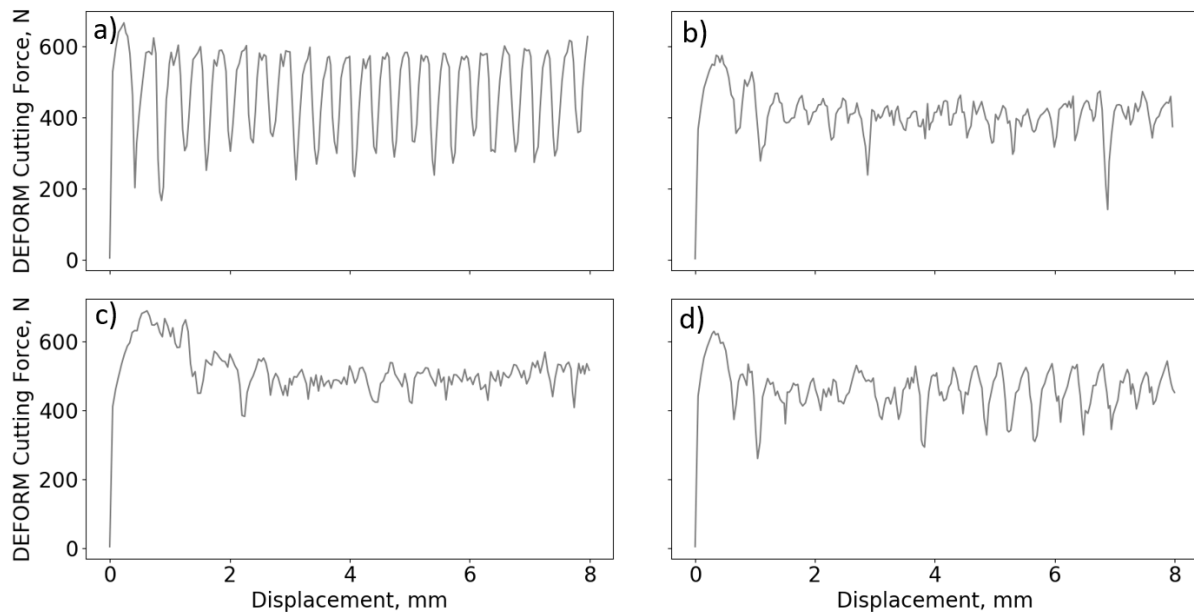


Figure 3.12: Figure of DEFORMTM 2D orthogonal cutting simulations showing the cutting forces required to form a chip for a) Ti-64 MA, b) Ti-407 STA Air Cooled, c) Ti-407 STA Oil Quenched, d) Ti-407 STA Water Quenched.

Using the same material parameters from the DEFORMTM uniaxial compression tests, a 2D orthogonal cutting test was simulated, to predict the chip forming characteristics of the test samples. The model was set up to closely replicate the cutting conditions of the small scale orthogonal cutting tests; by using a cutting tool with a chip breaker and a negative 6° rake angle; depth of cut of 0.3 mm and a cutting speed of 6.0 m.min⁻¹. There is strong agreement between the DEFORMTM chip forming models in Figure 3.11 and both the experimental compression tests and the DEFORMTM compression models in Figure 3.7 and Figure 3.10 respectively. Ti-64, which accommodates less strain prior to fracture forms a segmented chip. The chip form for Ti-407 varies hugely from one microstructural condition to the next. The higher strain accommodation in the Ti-407 oil quenched chip resulted in the formation of a continuous chip. The simulations shown in Figure 3.11 predict that the Ti-64 would form a high frequency segmented chip. The Ti-407 samples by contrast range from a segmented chip of moderate frequency to a fully continuous chip. Presence of adiabatic shear bands can be postulated from the fluctuations in the cutting forces shown in Figure 3.12a, which can be attributed to the thermal softening and strain hardening of the forming chip. One of the reasons for the lower regularity of segmentation of Ti-407 is due to its higher thermal conductivity [36], which is almost double that of Ti-64 at room temperature. Bäker et al. [44] studied the influence of thermal conductivity on the chip segmentation process, finding that the degree of segmentation reduced as thermal conductivity increased. The Ti-407 has far lower cutting force peaks, implying that the adiabatic shear bands are wider than Ti-64 surmising that the chip forming and breakability of the alloy is much more challenging

to manage. Furthermore, with greater strain accommodated in the chip more subsurface features such as severe plastic deformation and mechanical twinning can be retained in the machined surface.

3.3.1.4 Small Scale Cutting Experiments- Comparison of Chip Form for Ti-64 and Ti-407

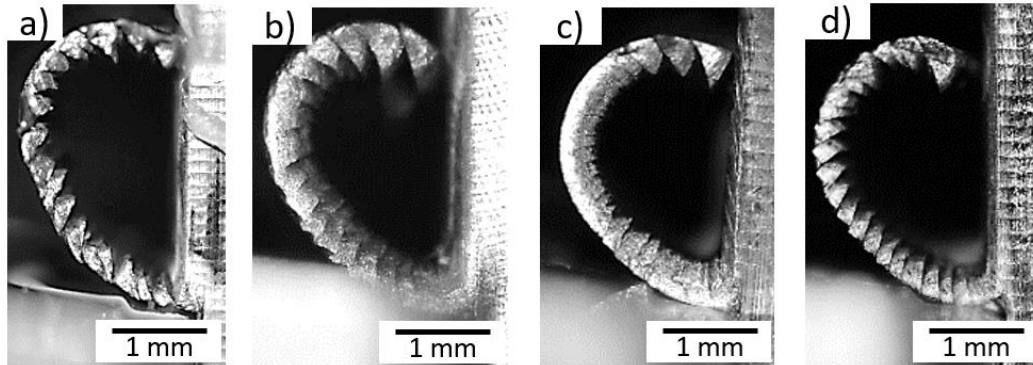


Figure 3.13: In-situ photographs taken with a Nikon D5000 camera of the chip forming process from the small scale orthogonal cutting tests, a) Ti-64 MA, b) Ti-407 STA Air Cooled, c) Ti-407 STA Oil Quenched and d) Ti-407 STA Water Quenched.

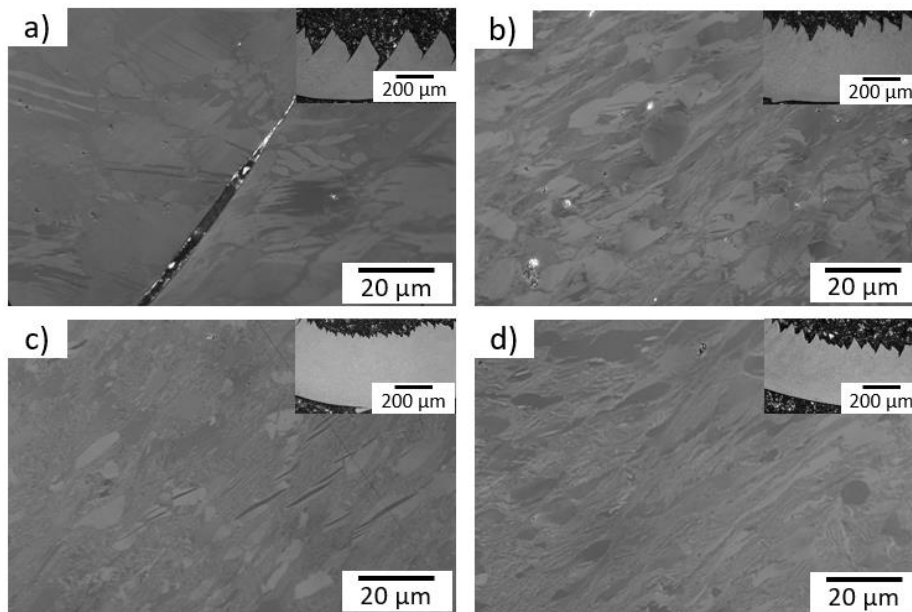


Figure 3.14: Cross sectional light micrographs of the chip formation from the small scale orthogonal cutting tests for a) Ti-64 MA, b) Ti-407 STA Air Cooled, c) Ti-407 STA Oil Quenched and d) Ti-407 STA Water Quenched

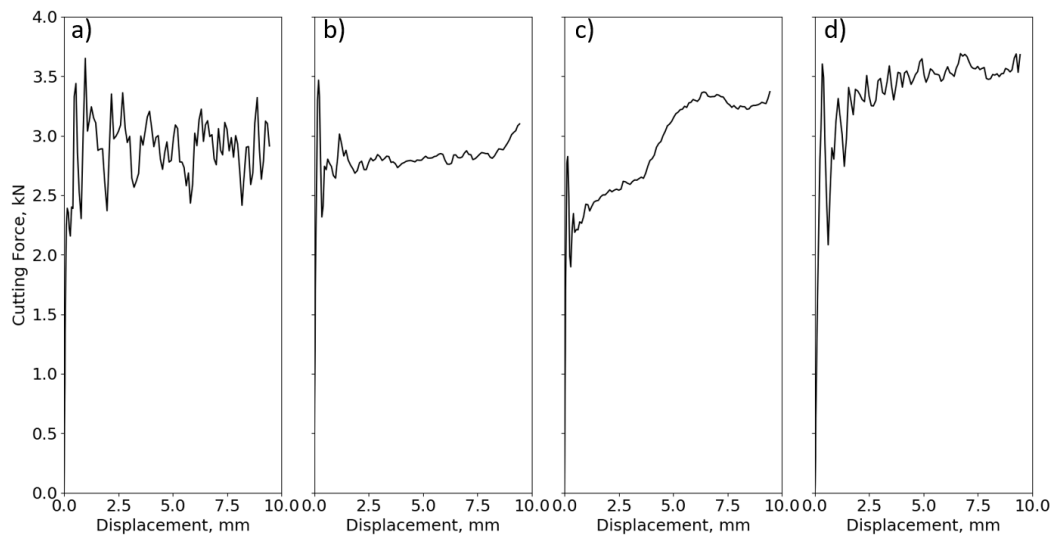


Figure 3.15: Experimental cutting forces measured from the small scale orthogonal cutting for a) Ti-64 MA, b) Ti-407 STA Air Cooled, c) Ti-407 STA Oil Quenched and d) Ti-407 STA Water Quenched.

Figure 3.13 shows in situ photographs from the small scale orthogonal cutting tests, which under identical conditions shows marked differences between the test alloys. There is good agreement between the experimental results and the FE orthogonal cutting models. Ti-64 in Figure 3.13a forms a segmented chip at regular intervals which analysed closely in the micrograph of Figure 3.14a shows that each chip segment is of consistent geometry and pitch, with formation of narrow shear bands between each. The Ti-407 oil quenched test piece, forms almost a continuous chip which is comparable to the predicted chip modelled in Figure 3.11c. Some researchers [45, 46] believe that there is a critical cutting speed when a continuous chip form ceases and a serrated, shear localised chip dominates. This theory is based on a purely thermally activated process; when cutting speed decreases to a ‘critical value’, the deformation becomes uniform and the distance between the shear bands approaches zero because the thermal gradient is negligible [47].

There is no discernible shear band in the Ti-407 oil quenched sample, showing that a uniform temperature gradient was present across the chip during the cut. The experimental cutting forces in Figure 3.15, show similar trends to the FE orthogonal cutting simulations, where the cyclicity of the cutting forces directly relate to the serrated nature of the chips, with Ti-64 MA being the most serrated with the largest force peaks and the Ti-407 oil quenched being the least. There is a sudden rise in the force output of the Ti-407 oil quenched, which will be discussed in a following section looking at tool wear.

Up to this point the results have focused on the small scale experimental work and modelling study. The industrial cutting tests have been requisite to validate the small scale experimental work and provide some relatability to industry. Figure 3.16 shows the chip form of both Ti-64 and Ti-407. Similarly to Figure 3.14, the Ti-64 forms a serrated chip, with large peaks and narrow shear bands,

conversely the Ti-407 forms chip segments with very small peaks and a continual shear band straining perpetually into the following section of the chip. Relating these observations to the overall machinability of the materials with a focus on chip breakability, it is apparent from Figure 3.17 that the Ti-64 MA chip is easier to manage and control compared to Ti-407 across a range of cutting speeds. Based on flow stress data and chip form characteristics, these results were predicted in the first part of this investigation with the compression tests and 2D orthogonal model.

3.3.1.5 Large Scale Turning Trials- Analysis of Chip Form for Ti-64 and Ti-407

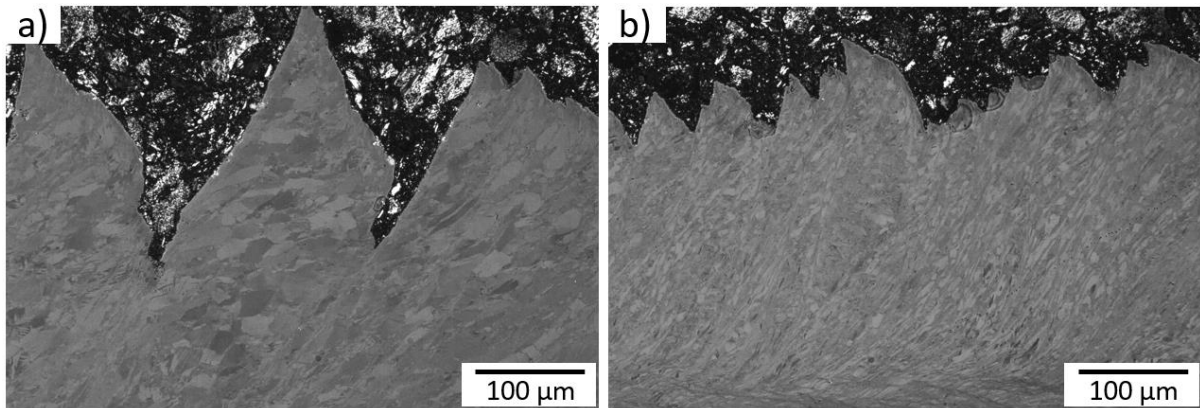


Figure 3.16: Cross sectional light micrographs of the chip formation from the industrial cutting tests for a) Ti-64 MA, b) Ti-407 STA Water Quenched.

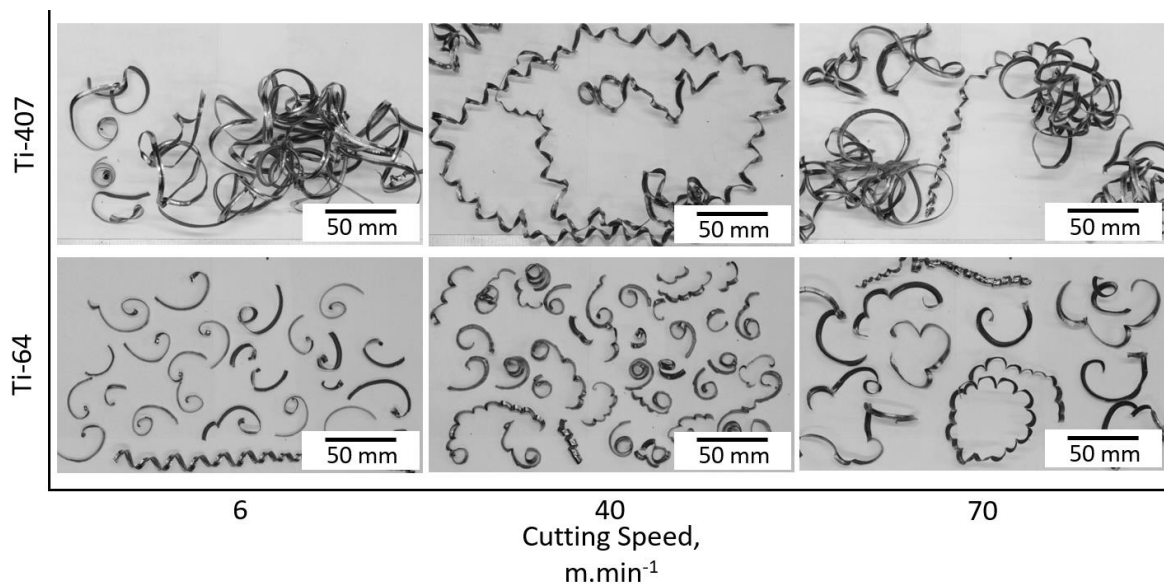


Figure 3.17: Photographs showing the comparable chip formation at cutting speeds (6, 40, and 70 $m.min^{-1}$) from the industrial orthogonal cutting tests of Ti-64 MA and Ti-407 STA Water Quenched. Feed Rate = $0.3 mm.rev^{-1}$.

In addition to reliable chip morphology, subsurface features have been obtained to support the work comparing small scale cutting and industrial scale cutting. Analysis of subsurface features are of paramount importance with features like white layer being rejected for aerospace components. Therefore being able to inform on the relative damage tolerance of one alloy against another during the development phase is essential. Previous work [2, 48] has shown that microstructural modifications in the subsurface of the titanium alloy are induced by machining parameters.

3.3.2 Subsurface Deformation Characteristics for Small Scale Cutting and Large Scale Turning Trials

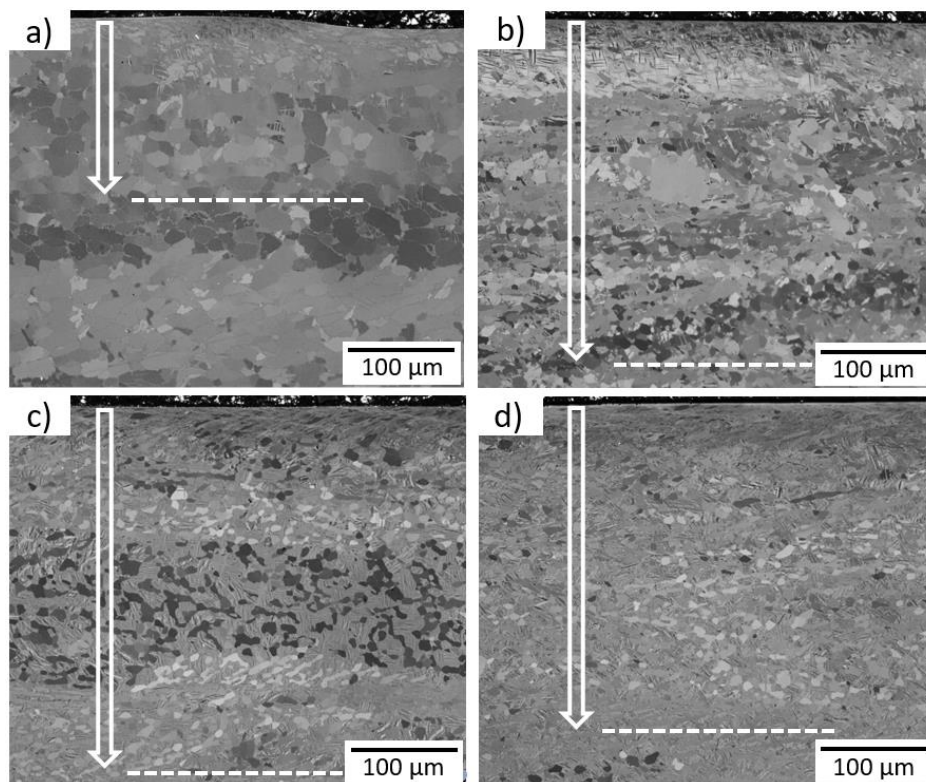


Figure 3.18: Light micrographs of the depth of subsurface features from the small scale orthogonal cutting tests, a) Ti-64 MA, b) Ti-407 STA Air Cooled, c) Ti-407 STA Oil Quenched and d) Ti-407 STA Water Quenched

Table 3.3: Measured depth of subsurface features including mechanical twins and severe plastic deformation from the small scale orthogonal cutting tests.

	Ti-64 MA	Ti-407 STA Air Cooled	Ti-407 STA Oil Quenched	Ti-407 STA Water Quenched
Max. Depth of Subsurface Features, μm	171	309	339	322

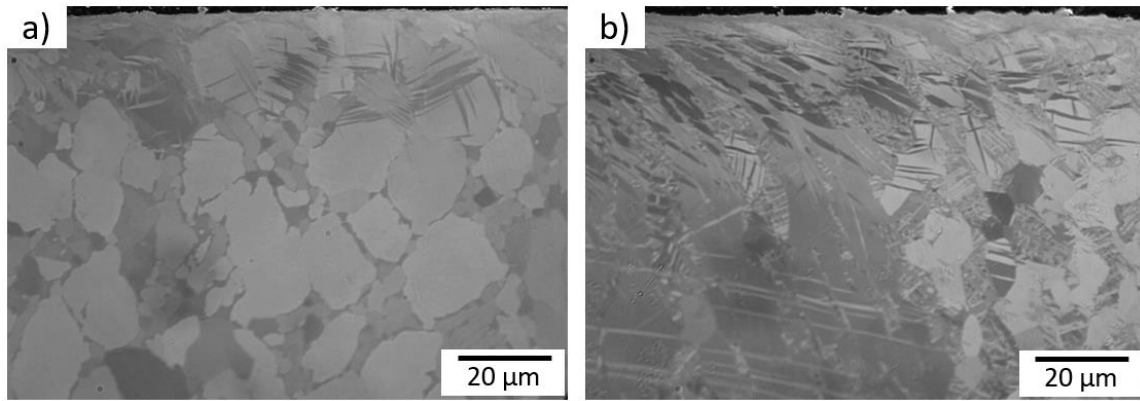


Figure 3.19: Light micrographs of the depth of the subsurface features from the industrial cutting trials, a) Ti-64 MA and b) Ti-407 STA Water Quenched.

In this work subsurface features were characterised as severe plastic deformation and mechanical twinning. Under the same cutting conditions the Ti-64 was able to tolerate the effects of machining more than Ti-407. Table 3.3 and Figure 3.18 shows the measured depth of subsurface features in the Ti-407 were almost double that of Ti-64 with mechanical twins being the predominant feature. Similarly Figure 3.19 shows the same trends for industrial cutting tests. Twin formation in Ti-64 occurred randomly across the surface of the alloy, likely due to variations in the grain orientation with certain grains being more favourable to slip. The Ti-407 however consistently formed a dense region of mechanical twins just below the machined surface. The mechanical twins provide a mechanism for the material to accommodate more strain before fracture occurs which is an idea put forward by Kloenne [49] to explain the improved ductility of Ti-407.

3.3.3 Comparison of the Cutting Forces for Small Scale Cutting and Large Scale Turning Trials

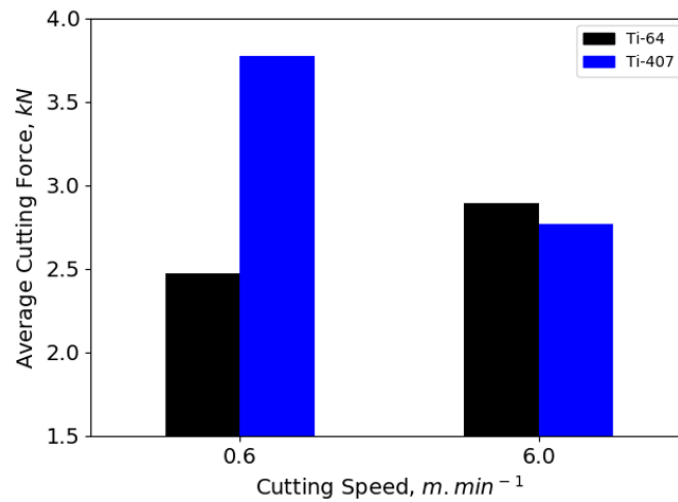


Figure 3.20: Bar plot showing the average cutting force in comparison to the cutting speed for the small scale orthogonal cutting tests for Ti-64 MA and Ti-407 STA Water Quenched Cooled.

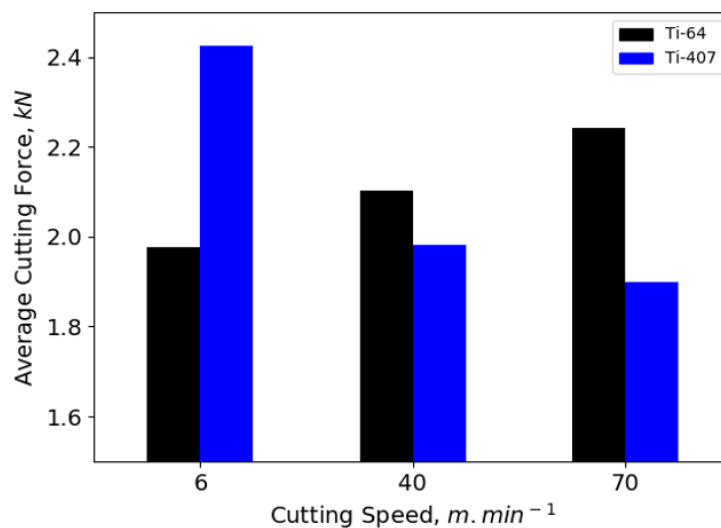


Figure 3.21: Bar plot showing the average cutting force in comparison to the cutting speed for the large scale cutting tests for Ti-64 MA and Ti-407 STA Water Quenched.

The average cutting forces for Ti-64 MA and Ti-407 STA water quenched have been presented in Figure 3.20 and Figure 3.21 for both the small scale orthogonal cutting and the industrial cutting trials respectively. The figures are significant as they show particular trends for each alloy. As the cutting speed increases, Ti-64 average cutting forces increase in agreement with other authors [50] whereas for Ti-407 these forces decrease, which shows that the relationship between thermal softening and strain hardening for each alloy is uniquely different. Predictions on tool wear can also be implied from these results as well. It would be prudent to assume that with the decreasing cutting forces, the stresses acting on the tool would also be reduced and tool wear mechanisms would change. Where Ti-407 would likely

develop more built-up edge (BUE) across the tool edge, from the softening of the workpiece; Ti-64 would likely experience the effect of more mechanical wear types as the stresses on the tool increase, through the likes of notch wear, chipping and crater wear.

3.3.4 Tool Wear Analysis for Ti-64 and Ti-407 using Diffusion Couple Experiments, Small Scale Cutting and Large Scale Turning Trials

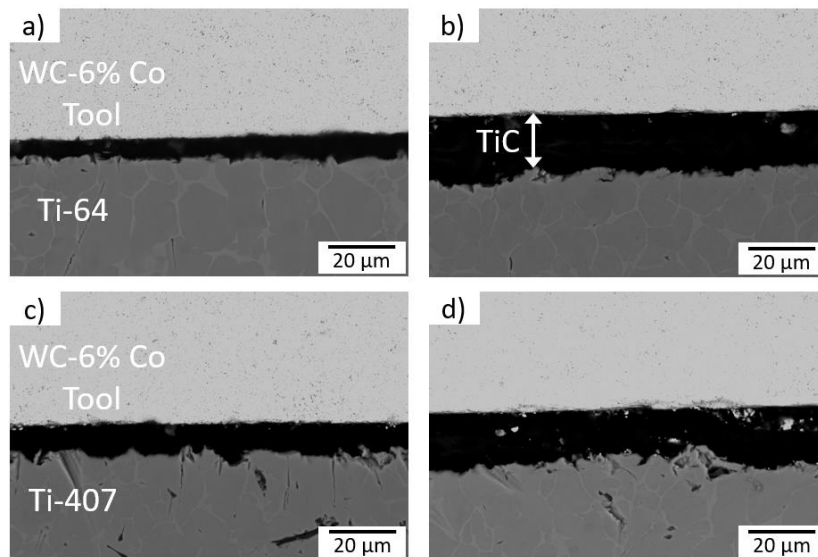


Figure 3.22: Scanning electron micrographs of the TiC interface between WC-6% Co cutting insert and workpiece material from diffusion couple experiments a) Ti-64 MA, b) Ti-407 STA Air Cooled, c) Ti-407 STA Oil Quenched and d) Ti-407 STA Water Quenched.

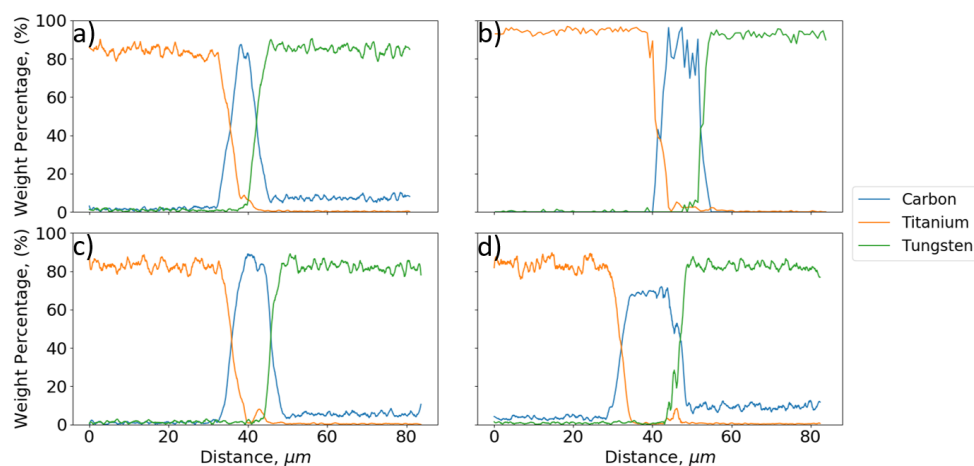


Figure 3.23: X-EDS analysis showing the titanium, tungsten and carbon across the tool and workpiece, including diffusion bond region. a) Ti-64 MA, b) Ti-407 STA Air Cooled, c) Ti-407 STA Oil Quenched and d) Ti-407 STA Water Quenched.

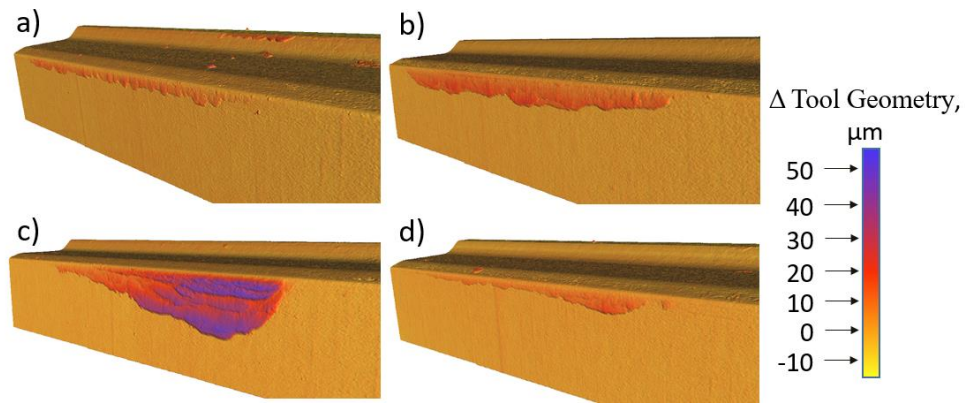


Figure 3.24: Alicona 3D scans of the tools from the small scale orthogonal cutting tests showing the build-up of workpiece material across the edge of the tool for a) Ti-64 MA, b) Ti-407 STA Air Cooled, c) Ti-407 STA Oil Quenched and d) Ti-407 STA Water Quenched.

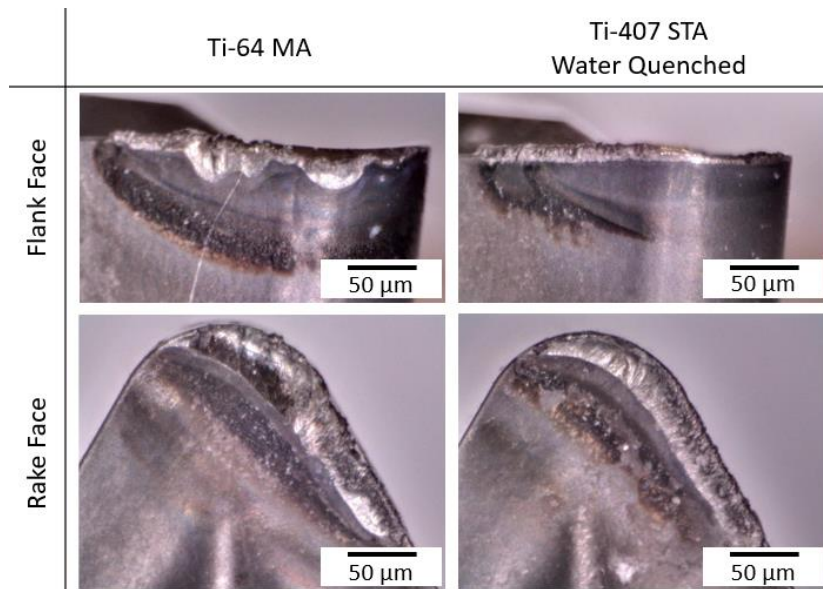


Figure 3.25: Photographs of the flank wear and rake face wear from tool life trials for Ti-64 MA and Ti-407 STA Water Quenched from large scale turning trials at 80 m.min^{-1} .

Crater wear, a wear mode recognised as detrimental to the life of a tool due to the high chemical reactivity of titanium alloys has been investigated previously [4, 5, 51]. Hatt and co-workers [4, 5] developed a low cost static diffusion couple experiment that could predict the complex reaction mechanisms that occur at the tool chip interface during high speed machining of titanium alloys. The methodology developed by Hatt et al. [4], was replicated in this study to investigate the chemical reactivity of the alloys. All of the alloy samples formed a strong diffusion bond with the tool. Figure

3.22 shows a dark region in between the tool and alloy which was determined to be a layer of TiC. This idea is further strengthened by Figure 3.23 which demonstrates through the utilization of X-EDS analysis a highly concentrated region of carbon in between the tool and the workpiece. The thickness of the TiC layer is larger for the Ti-407 compared to the Ti-64. The micrographs agree with Ref [5], where by increasing beta content and thus the molybdenum equivalency of an alloy, the thickness of the TiC layer decreases. The molybdenum equivalency for the two alloys in this investigation, Ti-64 and Ti-407 has been calculated as, 3.7 and 3.2 respectively. The TiC layer acts as a protective coating reducing the susceptibility of chemical wear. Based on this knowledge, the tool life for Ti-407 should be better than that of Ti-64 due to the lower chemical reactivity and the greater formation of TiC across the rake face.

Tool wear images for the small scale orthogonal and the industrial cutting tests pictured in Figure 3.24 and Figure 3.25 respectively, show strong correlations between the two test methods. The Ti-407 oil quenched in particular, is more susceptible than Ti-64 MA to BUE formation across the edge of the tool. The formation of BUE has been argued to act as a protective layer by forming work hardened material across the edge of tool delaying tool failure [52–55] however it significantly affects the rake angle of the tool [44] which has a further knock on effect to the shape and length of the chip and the surface finish of the machined work piece. Referring back to Figure 3.15c, the rise in cutting forces could be attributed to the formation of the BUE shown in Figure 3.24c. It would be beneficial to the tool life of Ti-407 to form a small layer of BUE in order to protect the tool from the effects of the alloys high chemical reactivity. Conversely, the higher thermal conductivity of the Ti-407 alloy should help protect the tool from crater wear longer than Ti-64, by promoting better heat transfer away from the tool, so lowering the rate of diffusivity of chemical elements at the tool-chip interface.

3.3.5 Contextualisation of the Small Scale Machinability Approach

It is necessary to place these results in a wider context. The small scale methods are not to be a direct replacement for conventional, machining trials; simply an early stage filtering step, exploited to efficiently down select compositions and microstructural conditions to generate new information for a material data sheet allowing machinability for different alloys to be compared. Table 3.4 provides an approximation of the costs associated with both the industrial cutting experiments and the small scale testing methods to examine the machinability of Ti-64 MA and Ti-407 STA water quenched. These costs do not include the price of the FEM software licence, for the small scale tests, however it should be noted that as the machinability tests are for preliminary exploration of a number of new compositions, the cost of the licence per simulated composition is minimal. The significant costs of machine time and technical support associated with the industrial cutting trials are attributed to the requirement for skilled personnel to operate the high energy consuming machining centres and the extra resources required which add further cost to the cutting operation. The small scale tests provide significant cost savings, in

the order of approximately 90%, and provide key information about the relative machinability of titanium alloys.

Table 3.4: Cost comparison for the testing Ti-64 MA and Ti-407 STA Water Quenched for the industrial cutting tests and the small scale tests.

	Industrial Cutting Trials	Small Scale Tests (Compression, Diffusion Couple and ASP)
Aerospace Quality Material, £40/kg	£2000	£10
Material Heat Treatment	£1000	£50
Material Machining Preparation	£0	£250
Machine and Labour	£3200	£250
Total	£6200	£560

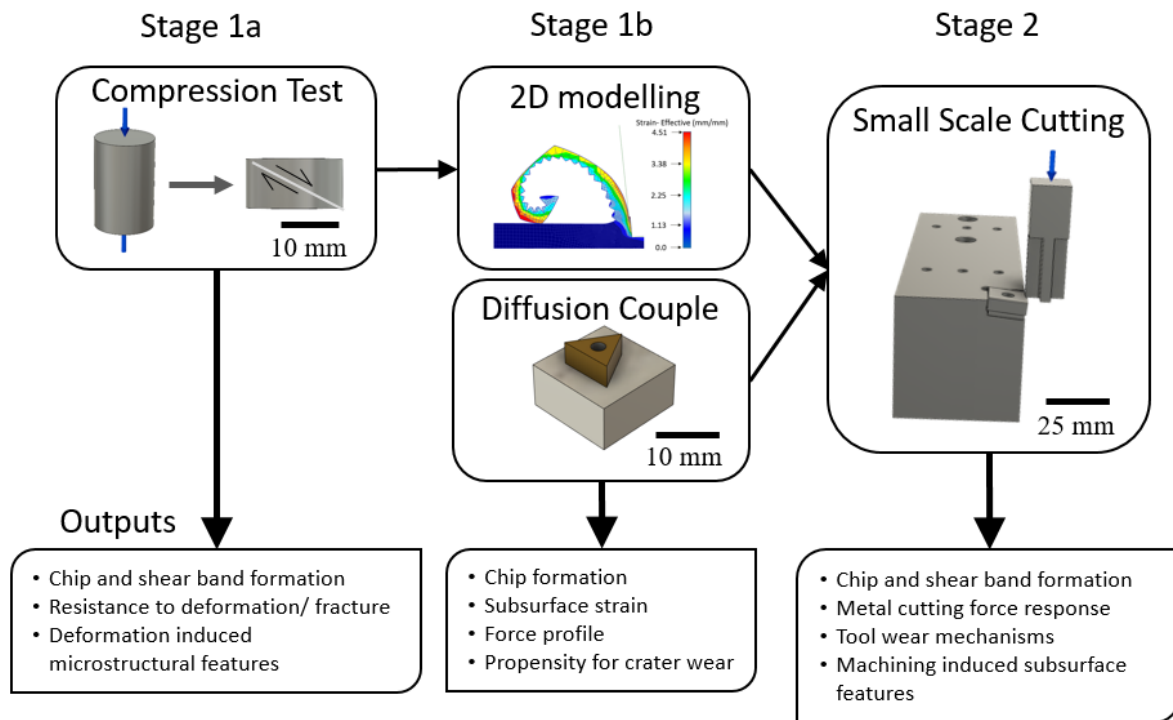


Figure 3.26: A schematic showing the suggested order for completion of the small scale tests and modelling to filter out undesirable alloy combinations and conditions.

The small scale tests coupled with the DEFORM™ models, have been developed and “stress tested” against full scale turning trials to inform on key machinability outputs. The tests are shown to be intrinsically linked such that the machinability outputs of each level, presented in the schematic of Figure 3.26 can be inferred through completion of each of the other tests. The first level of experiments

presented (the compression and the diffusion couple experiment), have provided an insight into the fundamental material and machinability data in particular flow stress, shear band formation characteristics and thermodynamic driving forces, directly correlating to the machinability variables, chip geometry characteristics, subsurface features and tool crater wear. Modelling the 2D chip form allows prediction of the relative strain accommodated in the titanium alloys, which again infers chip geometry characteristics, subsurface features and cutting forces of titanium alloys. The small scale cutting experiments in stage 2 not only validate observations from stage 1 but also provide better resolution of chip form and subsurface damage characteristics. Importantly, the machinability characteristics captured for Ti-64 and Ti-407 using the low cost machinability assessments were reliably observed in the large scale high speed turning trials.

3.4 Conclusions

The use of standalone small scale experiments to ascertain the machinability of future alloys, will be valuable for alloy and tool development. The low cost machinability approach filters out alloy combinations which do not offer desirable properties and predicts relative machinability, without the requirement of conducting costly, large scale and time consuming machinability trials. To conclude:

- A first level filter of a titanium alloys machinability can be determined from a simple uniaxial, room temperature compression test.
- Material parameters calculated from compression tests can be used to model 2D orthogonal chip formation of an alloy using FEM software.
- A small-scale, orthogonal cutting test has been developed to provide data on key machinability criteria including chip formation, tool wear, subsurface features and cutting forces.
- Key machinability criteria from the small-scale tests have been verified through industrial-scale cutting trials.
- The results show that both titanium alloys exhibit strengths and weaknesses when considering machinability as a whole. Ti-407 shows better machinability when the focus is on cutting forces and tool wear. However, Ti-64 shows better machinability in relation to subsurface microstructural features and chip control.
- The costs for completing the full set of small-scale tests (incl. uniaxial compression tests, orthogonal cutting and diffusion couple tests) and the industrial-scale cutting tests have been analysed. As an early stage, machinability assessment, the cost benefits along with the data output make this an attractive approach for screening emerging titanium alloy combinations and heat treatment conditions.

References

- [1] Lütjering G, Williams JC. Titanium. 2nd ed. Springer, 2007.
- [2] Thomas M, Turner S, Jackson M. Microstructural damage during high-speed milling of titanium alloys. *Scr Mater* 2010; 62: 250–253.
- [3] Arrazola PJ, Garay A, Iriarte LM, et al. Machinability of titanium alloys (Ti6Al4V and Ti555.3). *J Mater Process Technol* 2009; 209: 2223–2230.
- [4] Hatt O, Crawford P, Jackson M. On the mechanism of tool crater wear during titanium alloy machining. *Wear* 2017; 374: 15–20.
- [5] Hatt O, Lomas Z, Thomas M, et al. The effect of titanium alloy chemistry on machining induced tool crater wear characteristics. *Wear* 2018; 408–409: 200–207.
- [6] Johnson GR, Cook WH. Fracture characteristics of three metals subjected to various strains, strain rates, temperatures and pressures. *Eng Fract Mech* 1985; 21: 31–48.
- [7] Seo S, Min O, Yang H. Constitutive equation for Ti – 6Al – 4V at high temperatures measured using the SHPB technique. *Int J Impact Eng* 2005; 31: 735–754.
- [8] Macdougall DAS, Harding J. A constitutive relation and failure criterion for Ti6Al4V alloy at impact rates of strain. *J Mech Phys Solids* 1999; 47: 1157–1185.
- [9] Lee W, Lin C. High-temperature deformation behaviour of Ti6Al4V alloy evaluated by high strain-rate compression tests. *J Mater Process Technol* 1998; 75: 127–136.
- [10] Lee W, Lin C. Plastic deformation and fracture behaviour of Ti–6Al–4V alloy loaded with high strain rate under various temperatures. *Mater Sci Eng A* 1998; 241: 48–59.
- [11] Kiranli E. Determination of material constitutive equation of a biomedical grade Ti-6Al-4V alloy for cross-wedge rolling. Izmir Institute of Technology, 2009.
- [12] Nemat-Nasser S, Guo WG, Nesterenko VF, et al. Dynamic response of conventional and hot isostatically pressed Ti–6Al–4V alloys: experiments and modeling. *Mech Mater* 2001; 33: 425–439.
- [13] Meyer HW, Kleponis DS. Modeling the high strain rate behavior of titanium undergoing ballistic impact and penetration. *Int J Impact Eng* 2001; 26: 509–521.
- [14] Dorogoy A, Rittel D. Determination of the Johnson – Cook Material Parameters Using the SCS Specimen. *Exp Mech* 2009; 49: 881.
- [15] Kay G. Failure Modeling of Titanium-6Al-4V and 2024-T3 Aluminum with the Johnson-Cook Material Model. 2002; 1–28.

- [16] Khan AS, Sung Suh Y, Kazmi R. Quasi-static and dynamic loading responses and constitutive modeling of titanium alloys. *Int J Plast* 2004; 20: 2233–2248.
- [17] Oxley PLB. *The Mechanics of machining: An analytical approach to assessing machinability*. Halsted Press, 1989.
- [18] Shatla M, Kerk C, Altan T. Process modeling in machining. Part I: determination of flow stress data. *Int J Mach Tools Manuf* 2001; 41: 1511–1534.
- [19] Molinari A, Musquar C, Sutter G. Adiabatic shear banding in high speed machining of Ti–6Al–4V: experiments and modeling. *Int J Plast* 2002; 18: 443–459.
- [20] Miguélez MH, Soldani X, Molinari A. Analysis of adiabatic shear banding in orthogonal cutting of Ti alloy. *Int J Mech Sci* 2013; 75: 212–222.
- [21] Miguélez MH, Zaera R, Molinari A, et al. Residual Stresses in Orthogonal Cutting of Metals: The Effect of Thermomechanical Coupling Parameters and of Friction. *J Therm Stress* 2009; 32: 269–289.
- [22] Bai W, Sun R, Roy A, et al. Improved analytical prediction of chip formation in orthogonal cutting of titanium alloy Ti6Al4V. *Int J Mech Sci* 2017; 133: 357–367.
- [23] Zhou J, Ren J, Jiang Y. Inverse identification of modified Johnson–Cook model for cutting titanium alloy Ti6Al4V using firefly algorithm. *Proc Inst Mech Eng Part B J Eng Manuf* 2020; 234: 584–599.
- [24] Nasr M, Ng E, Elbestawi M. Effects of workpiece thermal properties on machining-induced residual stresses - thermal softening and conductivity. *Proc Inst Mech Eng Part B J Eng Manuf* 2007; 221: 1387–1400.
- [25] Cotterell M, Byrne G. Characterisation of chip formation during orthogonal cutting of titanium alloy Ti–6Al–4V. *CIRP J Manuf Sci Technol* 2008; 1: 81–85.
- [26] Cotterell M, Byrne G. Dynamics of chip formation during orthogonal cutting of titanium alloy Ti–6Al–4V. *CIRP Ann* 2008; 57: 93–96.
- [27] Laakso SVA, Niemi E. Determination of material model parameters from orthogonal cutting experiments. *Proc Inst Mech Eng Part B J Eng Manuf* 2016; 230: 848–857.
- [28] Hastings WF, Oxley PLB, Stevenson MG. Predicting a Material's Machining Characteristics Using Flow Stress Properties Obtained from High-Speed Compression Tests. *Proc Inst Mech Eng* 1974; 188: 245–252.

- [29] Chen G, Ren C, Yu W, et al. Application of genetic algorithms for optimizing the Johnson–Cook constitutive model parameters when simulating the titanium alloy Ti-6Al-4V machining process. *Proc Inst Mech Eng Part B J Eng Manuf* 2012; 226: 1287–1297.
- [30] Chandrasekaran H, M’saoubi R, Chazal H. Modelling of material flow stress in chip formation process from orthogonal milling and Split Hopkinson bar tests. *Mach Sci Technol* 2005; 9: 131–145.
- [31] Storchak, Rupp, Möhring, et al. Determination of Johnson–Cook Constitutive Parameters for Cutting Simulations. *Metals (Basel)* 2019; 9: 473.
- [32] Shrot A, Bäker M. Determination of Johnson–Cook parameters from machining simulations. *Comput Mater Sci* 2012; 52: 298–304.
- [33] Sutter G. Chip geometries during high-speed machining for orthogonal cutting conditions. *Int J Mach Tools Manuf* 2005; 45: 719–726.
- [34] Marshall L, Wynne B, Turner S, et al. Influence of Aluminium Content on the Machinability and Subsurface Deformation Of Titanium Alloys. In: *Proceedings of the 13th World Conference on Titanium*. Hoboken, NJ, USA: John Wiley & Sons, Inc., pp. 923–928.
- [35] Hatt O, Larsson H, Giuliani F, et al. Predicting Chemical Wear in Machining Titanium Alloys Via a Novel Low Cost Diffusion Couple Method. *Procedia CIRP* 2016; 45: 219–222.
- [36] James S, Kosaka Y, Thomas R, et al. Timetal® 407: A Titanium Alloy to Enable Cost Reduction. In: *Proceedings of the 13th World Conference on Titanium*. 2016, pp. 721–725.
- [37] Marshall L. The influence of aluminium additions on titanium during machining through the application of a novel orthogonal cutting test method. University of Sheffield, 2014.
- [38] Salem AA, Kalidindi SR, Doherty RD. Strain hardening of titanium: role of deformation twinning. *Acta Mater* 2003; 51: 4225–4237.
- [39] Salem AA, Kalidindi SR, Doherty RD. Strain hardening regimes and microstructure evolution during large strain compression of high purity titanium. *Scr Mater* 2002; 46: 419–423.
- [40] Scientific Forming Technologies. DEFORM v11.2.
- [41] Devotta A, Sivaprasad P, Beno T, et al. A Modified Johnson-Cook Model for Ferritic-Pearlitic Steel in Dynamic Strain Aging Regime. *Metals (Basel)* 2019; 9: 528.
- [42] Guo YB, Wen Q, Woodbury KA. Dynamic material behavior modeling using internal state variable plasticity and its application in hard machining simulations. *J Manuf Sci Eng Trans ASME* 2006; 128: 749–759.

- [43] Cockroft MG, Latham DJ. Ductility and the Workability of Metals. *J Inst Met* 1968; 96: 33–39.
- [44] Bäker M, Rösler J, Siemers C. The influence of thermal conductivity on segmented chip formation. In: *Computational Materials Science*. 2003, pp. 175–182.
- [45] Komanduri R, Hou Z. On Thermoplastic Shear Instability in the Machining of a Titanium Alloy (Ti-6Al-4V). *Metall Mater Trans A* 2002; 33: 1–16.
- [46] Groover M. *Fundamentals of Modern Manufacturing Materials, Processes and Systems*. 4th Editio. John Wiley & Sons Inc, 2011.
- [47] Machado AR, Wallbank J. Machining of Titanium and its Alloys—a Review. *Proc Inst Mech Eng Part B J Eng Manuf* 1990; 204: 53–60.
- [48] Crawford P, Wynne B, Turner S, et al. Subsurface deformation during precision turning of a near-alpha titanium alloy. *Scr Mater* 2012; 67: 842–845.
- [49] Kloenne Z, Viswanathan G, Thomas M, et al. A Comparative Study on the Substructure Evolution and Mechanical Properties of TIMETAL 407 and Ti-64. In: *The 14th World Conference on Titanium Proceedings*. 2019, pp. 1–6.
- [50] Polishetty A, Shunmugavel M, Goldberg M, et al. Cutting Force and Surface Finish Analysis of Machining Additive Manufactured Titanium Alloy Ti-6Al-4V. *Procedia Manuf* 2017; 7: 284–289.
- [51] Odelros S, Kaplan B, Kritikos M, et al. Experimental and theoretical study of the microscopic crater wear mechanism in titanium machining. *Wear* 2017; 376–377: 115–124.
- [52] Oliaei SNB, Karpat Y. Investigating the influence of built-up edge on forces and surface roughness in micro scale orthogonal machining of titanium alloy Ti6Al4V. *J Mater Process Technol* 2016; 235: 28–40.
- [53] Oliaei SNB, Karpat Y. Built-up edge effects on process outputs of titanium alloy micro milling. *Precis Eng* 2017; 49: 305–315.
- [54] Wyen C, Wegener K. Influence of cutting edge radius on cutting forces in machining titanium. *CIRP Ann* 2010; 59: 93–96.
- [55] Ramaswami R. The effect of the built-up-edge (BUE) on the wear of cutting tools. *Wear* 1971; 18: 1–10.

Machinability Maps – Towards a Mechanistic Understanding of the Machining of Ti-6Al-4V and Timetal 407

4

4.1 Introduction

The last decade has witnessed an increase in air traffic, in particular, a greater demand for single aisle commercial aircraft. To meet such demand, there has been an increase in the production of airframe and aero-engine components [1]. As titanium is the fastest growing material in the aerospace sector [2], there is a requirement for increased manufacturing rates to meet the growing demand. As a result, new titanium alloys have been developed and marketed on the fact that they have improved machinability, with the potential to be machined at much higher metal removal rates (MRRs).

Machinability, a term used to describe the property of a material or a part to be machined [3], has been discussed by numerous authors to offer insights into comparable tool wear, force data, surface integrity and chip forming characteristics of different titanium alloys. The machinability of titanium alloys has been reviewed over recent years, largely from a chip formation, cutting force and tool wear standpoint as in Refs. [4], [5]. Surface integrity was later incorporated into machinability reviews by Ezugwu and Wang [6] and Yang and Liu [7].

A number of mechanistic studies have been conducted to understand the influence of alloy chemistry and microstructure on titanium alloy machinability, such as, Marshall *et al.* [8] studied the influence of aluminium content on the machinability and subsurface deformation in binary titanium alloys. Arrazola *et al.* [9] assessed the machinability of Ti-64 and Ti-5553, investigating specific cutting forces, tool wear and chip analysis. The study was heavily focussed on tool wear, with the cutting forces and chip analysis being used to offer insights into their individual effects on tool wear. A machinability study by Khanna *et al.* [10]–[12] explored specific cutting forces, chip morphology and cutting tool temperature in Ti-64, Ti-54M and Ti-1023. Armendia *et al.* [13], [14], reported higher wear rates in Ti-6246 compared to Ti-64; in single point turning trials, Ti-64 had higher wear rates than Ti-54M. Jaffery and Mativenga [15] assessed the machinability of Ti-64 using a wear map approach to highlight the regions of high and low tool wear for a range of turning variables. However, the study did not incorporate other important criteria, such as chip formation and surface microstructural deformation characteristics. To the best of the authors' knowledge, no comprehensive model has been produced to offer an informative machinability map that predicts the effect of cutting parameters and MRR on tool wear, chip form and subsurface microstructural deformation.

TIMETAL® 407 (Ti-407) an $\alpha + \beta$ titanium alloy with composition Ti-3.9V-0.85Al-0.25Si-0.25Fe has been recently developed as an alternative to Ti-64 in applications where energy absorption at high strain rates is an important design consideration. Ti-407 has also been marketed as an alloy that is ‘more machinable’ and delivers improved MRR during machining compared to Ti-64 [16]. The high energy absorption prior to fracture is due to Ti-407’s improved ductility [16], accommodating greater strain at the point of fracture compared to Ti-64. Mechanistically, the higher ductility in Ti-407 has been shown to be a result of the alloy’s propensity for mechanical twinning over deformation slip, with mechanical twins being responsible for the greater strain accommodation in the alloy [17]. The favourable twinning deformation is thought to be due to the low aluminium content in Ti-407, which is 0.85 wt.%, compared to 6.0 wt.% in Ti-64. As previous research has shown, increasing the aluminium content reduces elongation to failure [18], causes unstable shear [19], and there is evidence to suggest that titanium alloy contents of > 6.0 wt.% aluminium completely suppress mechanical twinning [20].

Early testing by Dredge *et al.* [21] has demonstrated the positive machinability properties of Ti-407 with respect to tool wear and cutting forces, however challenges with controlling chip formation for a range of cutting speeds were highlighted. The study did not consider all machinability criteria, such as incorporating the effects of machining on subsurface microstructural deformation or providing an explanation for the poor chip breakability, which this paper also aims to address. The challenge of chip control is dictated by a combination of material properties, chemistry and initial microstructure. Groover [22] has shown that greater ductility can lead to the formation of long continuous chips during machining. Titanium alloys are well documented for their formation of serrated chips through shear localisation [23], [24] owing to their inherent low thermal conductivity and high work hardening characteristics. Serrated chips are considered beneficial for chip breakability, however they have been linked to cyclic cutting forces and tool chatter, both of which are detrimental to workpiece surface integrity and tool life [6], [25], [26].

Groover [22] and Komanduri and Hou, [27] have shown that to transition the chip morphology from continuous to serrated, a critical cutting speed must be reached in order for the onset of shear localisation to occur. Komanduri and Hou [27] found that due to the properties of titanium alloys, the critical cutting speed for shear localisation is rather low, indicating that this transition could occur at all conventional cutting speeds. However, very high cutting speeds can cause a deterioration in the chip breakability of titanium alloys, by decreasing the chip thickness, increasing the segmentation frequency and causing a localised temperature increase. These factors in turn reduce the time and length of material over which thermoplastic-instability occurs, lowering the shear strain within the chip and causing further thermal softening, which for ductile materials negatively affects the breakability of chips [28]. For example, Sun *et al.* [29] stated that machining Ti-64 at cutting speeds greater than 75 m.min⁻¹ caused the chip length to increase.

Increasing the feed rate can be an effective solution to counteracting poor chip breakability by decreasing the segmentation frequency [30], thus forming a thicker chip. Rahman [31] stated that by increasing the feed rate, the shear strain within the adiabatic shear bands (ASBs) increases, aiding chip breakage. In addition, thicker chips are more effective at removing heat from the cutting zone, which prolongs tool life and reduces localised tool-workpiece temperatures. Chandler [32] has suggested that higher feed rates are more desirable for productivity, as this does not increase the tool wear rate as significantly as cutting speed and depth of cut. However, if the feed rate is too high, the likelihood of catastrophic tool failure increases significantly, due to the high stresses on the tool [33]. In fact, a common limitation of increasing the feed rate is the negative effect it has on component surface integrity [34].

In this study, the machinability of Ti-64 and Ti-407 was assessed with respect to the key criteria: (1) subsurface microstructural deformation, (2) tool wear and (3) chip formation and compared through easy-to-visualise machinability maps. Additionally an explanation for Ti-407's poor chip control is also evaluated with respect to the machinability map.

4.2 Methodology

4.2.1 Material Preparation

As-forged Ti-64 and Ti-407 billet material of diameter 225 mm was provided by TIMET UK. Both alloys were sectioned into 20 mm thick disks and different annealing heat treatments were applied to each disk. The Ti-64 underwent a mill annealed (MA) heat treatment and the Ti-407 a solution treatment, water quench and age (STA), as recommended by the aerospace supply chain. The micrographs of these have been presented in Figure 4.1.

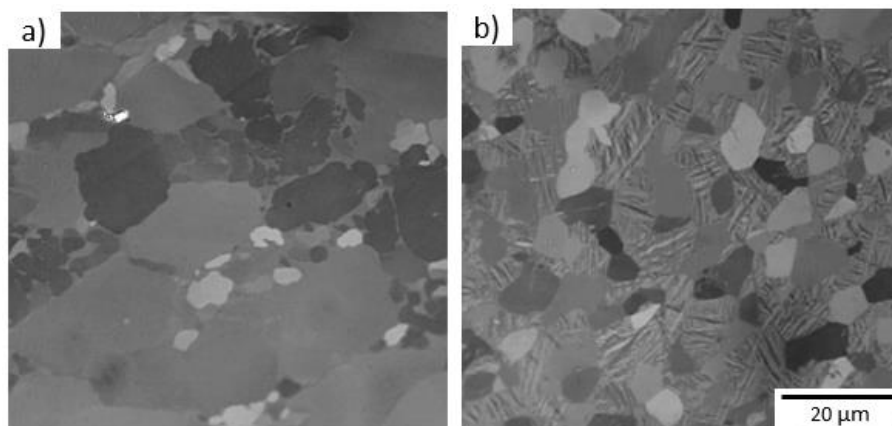


Figure 4.1: Light optical micrographs of the titanium alloys post-heat treatment a) Ti-64 (Mill Annealed), b) Ti-407 (Solution Treated and Aged).

4.2.2 Machining Trials

Turning trials were conducted on a DMG Mori NLX 2500 CNC machine turning centre at The University of Sheffield's Advanced Manufacturing Research Centre (AMRC), with the set up shown in Figure 4.2. The cutting tools used were WC-6% Co, TNMG160408-MF1, uncoated inserts supplied by Seco Tools. Prior to testing, the cutting tools were measured using an Alicona Infinite focus SL to ensure the cutting edge radius used in this work varied by less than 5%. A PTJNL2525M16 tool holder was modified by wire EDM to offset tool angles back to orthogonal, whilst maintaining the negative 6° rake angle. An outer ring of width 4 mm was grooved out using an internal grooving tool and an LCMF160608-0600-FT insert leaving a test geometry as presented in Figure 4.2a. The width of the region used for the orthogonal machining tests was measured to be 4 mm ± 0.05 mm using a ball micrometer. The tests were conducted over an axial cut distance of 5 mm and were performed at a range of cutting parameters shown in Table 4.1 to maintain relevance to industrial machining applications. For this study, the middle of the tool insert chip breaker, as shown by the red box over the tool edge in Figure 4.2b, was used during turning trials to replicate an industrial plunge turning operation - whereby deep, continuous grooves are cut into the workpiece. The red arrow in Figure 4.2b shows the direction of motion of the tool during the cut. Once the axial cut distance of 5 mm was reached, the tool was immediately retracted away in the opposite direction to the feed-in direction to preserve the machined surface for further analysis. Finally, Hocut 795b was supplied through external coolant hose pipes at a pressure of 6 bar to provide lubrication and cooling to the tool and workpiece.

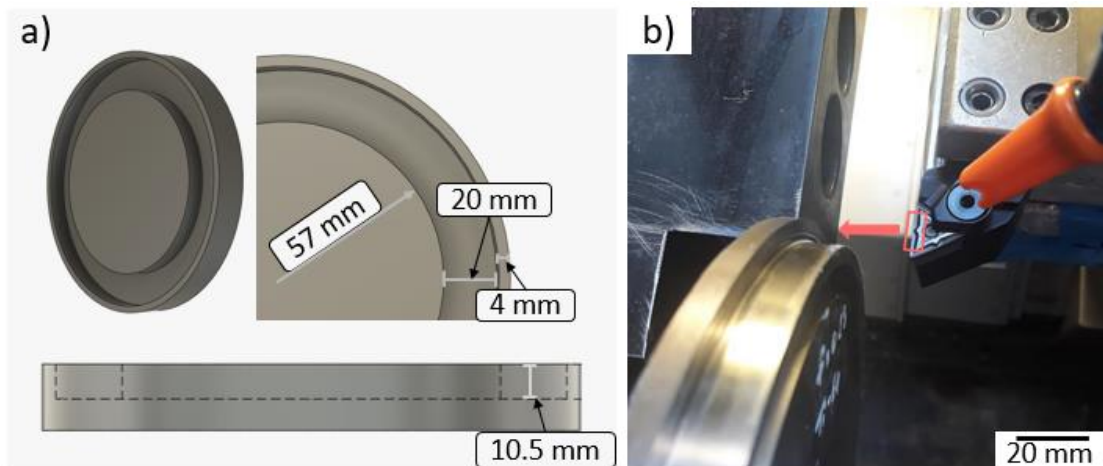


Figure 4.2: a) 3D CAD drawing of the workpiece after grooving the disk with a 4 mm wide ring for orthogonal axial plunge turning trials, b) Photograph of the setup for the orthogonal turning trials. A red box around the tool edge indicates the 4mm wide section of the tool used to perform the orthogonal cutting operation. The red arrow shows the direction of movement of the tool.

Table 4.1: The cutting parameters used in the orthogonal experiments to turn Ti-64 and Ti-407 billet (in Figure 4.2)

Test no.	With of cut, mm	Feed Rate, mm.rev ⁻¹	Cutting Speed, m.min ⁻¹
1	4.0	0.15	40
2	4.0	0.15	70
3	4.0	0.23	55
4	4.0	0.30	6.0
5	4.0	0.30	40
6	4.0	0.30	70

4.2.3 Subsurface Deformation

To assess the imparted deformation in the machined surface, the machined surfaces were sectioned from the disks, set in conductive bakelite and ground and polished to a mirror finish. A Nikon LV150 optical microscope with polarised light was used to reveal the depth of mechanical twins in the machined surface. Electron Backscatter Diffraction (EBSD) imaging was employed to reveal the depth of the severe plastic deformation (SPD) by measuring the crystallographic orientation of the α phase in the machined surface, using an FEI Sirion field emission gun scanning electron microscope with a 20 keV accelerating voltage and a step size of 0.1 μm . Automated indexing and post processing of the electron diffraction data was performed using Oxford Instruments HKL Channel 5 software. To quantify the depth of SPD in the machined surface, low angle grain boundary (LAGB) density between the alloys was compared from the surface to the bulk material. A misorientation angle of between 1° and 10° was defined as the LAGB range [35], [36]. The measurements were not taken from the machined surface as the poor indexing revealed too few grains to accurately measure the density of misorientations. The LAGB measurements were normalised for both materials in order to show the relative effect of cutting parameters on the density of misorientations.

4.2.4 Tool Wear

The tool flank wear images were taken using a Dino-lite digital microscope. The flank wear was measured using the Dinocapture software. The experiments were designed such that flank wear would be the major tool wear type. This allowed fair comparison between the alloy's wear rate without additional effects of other wear mechanisms.

4.2.5 Chip Analysis

Using a Nikon D5000 camera, photographs of the chips were taken to compare the chip morphology for each alloy. The chips were then broken into smaller pieces, set in conductive bakelite and ground and polished to a mirror finish. Microstructural analysis was carried out on a Nikon LV150 optical microscope using polarised light to reveal the morphology of the chip form and characteristics of the adiabatic shear band formation.

4.2.6 Development of the Machinability Map

To create the machinability map, the machinability outputs i.e. tool flank wear, chip formation and subsurface deformation were split into their own distinct categories. Chip formation was split into chip morphology and chip mechanical twins, and subsurface deformation was split into SPD and subsurface twins. Splitting machinability outputs was necessary to realise the independent nature of each variable.

A multi-variable linear regression was used to present the relationship between the cutting parameters (cutting speed and feed rate) and all of the machinability outputs, except for chip mechanical twins which used a linear support vector machine (SVM) model. A linear SVM model was utilised for the analysis of the chip mechanical twins as the output data fell into one of two categories (twins or no twins), therefore a multi-variable linear regression was inappropriate for this data type. The equation for both models has been shown in Equation 4.1.

$$\hat{y}_i = \beta_0 v + \beta_1 f + a \quad \text{Equation 4.1}$$

β_0 was the slope coefficient for the cutting speed variable. β_1 was the slope coefficient for the feed rate variable, a was the y-intercept, \hat{y}_i was the dependent variable and v and f were the independent variables, cutting speed and feed rate respectively.

For the multivariable linear regression the p-value was used to assess the statistical significance of the regressions. A value less than 0.05 being described as statistically significant. The adjusted R^2 was also used alongside the p-value as a statistical measure to determine how well the data fits to the regression model. Values for the adjusted R^2 range from 0 to 1 with a value closer to 1 indicating a better model fit. For the linear SVM model the accuracy was calculated to confirm the percentage of the data points which was correctly identified as either forming no twins or twins, i.e. pass (0) or fail (1) for the binary outputs.

4.3 Results

The results have been split into two sections. Section one presents the results and numerical values which led to the development of the machinability maps. Section two explores the machinability maps explaining what can be learnt from using maps in this way.

4.3.1 Section 1: Experimental Results

4.3.1.1 Comparison of subsurface mechanical twinning

Mechanical twins have been shown to be sites for crack initiation during cyclic loading [37], [38], therefore for a lifing engineer setting strict conditions on the depth of mechanical twins is necessary to ensure the longevity of the component. Figure 4.3 and Figure 4.4 present light optical micrographs of the machined subsurface of Ti-64 and Ti-407 respectively, showing the depth to which mechanical twins occur. Table 4.2 shows the measured depth of subsurface twins for all of the data points tested. The density of mechanical twins is significantly higher in Ti-407 compared to Ti-64. Additionally increasing the cutting speed and feed rate saw increases in the depth of mechanical twins, with a proportionally bigger increase observed with feed rate, which agrees with work by [8]:

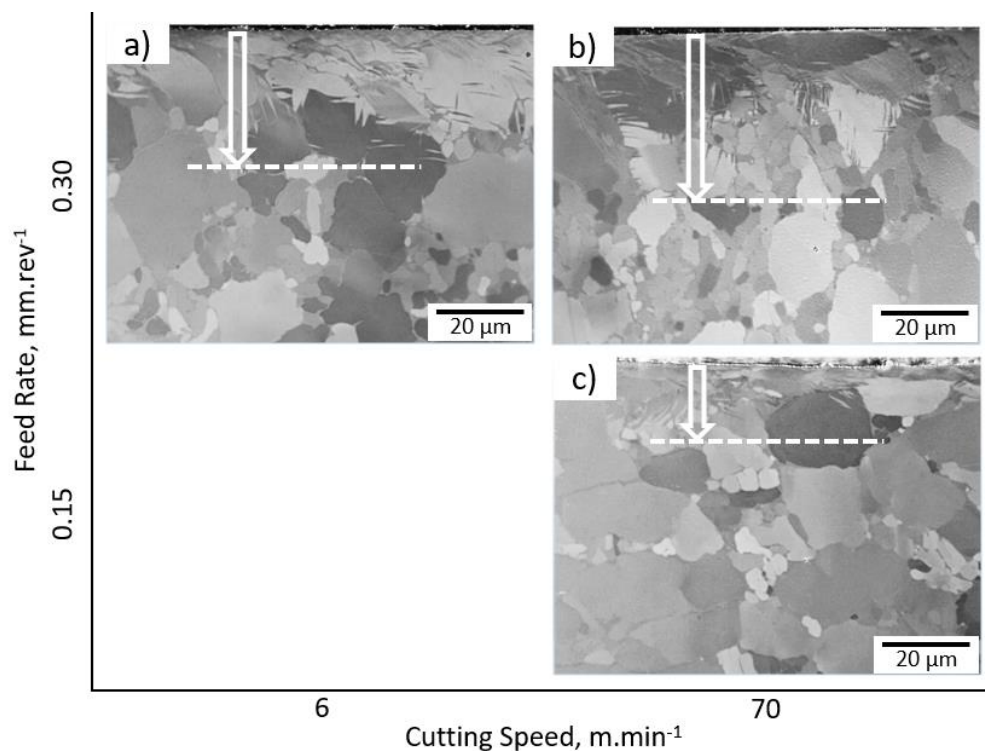


Figure 4.3: Light optical micrographs showing the depth of subsurface twins after machining Ti-64 at different cutting speeds and feeds in the orthogonal cutting tests.

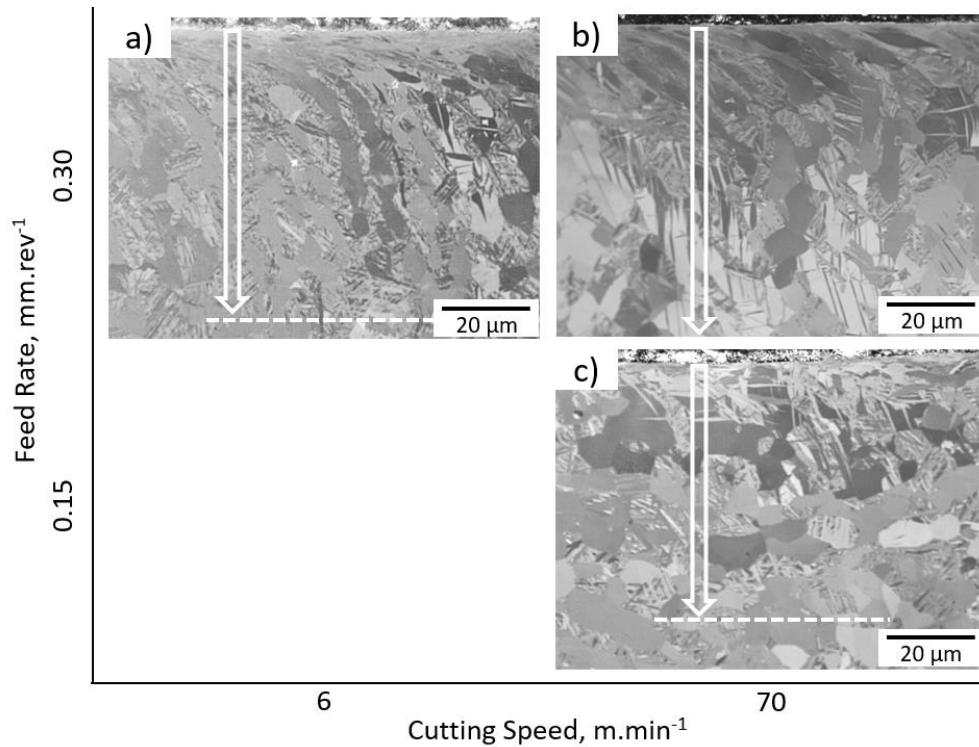


Figure 4.4: Light optical micrographs showing the depth of subsurface twins after machining Ti-407 at different cutting speeds and feeds in the orthogonal cutting tests.

Table 4.2: Measured depth of subsurface twins within the machined surface of Ti-64 and Ti-407 over the range of cutting parameters.

Cutting Speed, m.min ⁻¹	Feed Rate, mm.rev ⁻¹	Ti-64	Ti-407
		Subsurface Twins, μm	Subsurface Twins, μm
6	0.3	30	70
40	0.3	35	85
70	0.3	40	100
40	0.15	15	30
70	0.15	20	50
55	0.23	25	60

4.3.1.2 Comparison of microstructural subsurface deformation

Figure 4.5 shows EBSD scans used to assess the imparted deformation in the machined surface. Table 4.2 presents the measured depth of SPD within the machined surface of Ti-64 and Ti-407 for the full range of cutting parameters. Due to the SPD directly beneath the machined surface, Kikuchi band indexing was poor. From the orientation imaging data, the extent of the SPD was visually evaluated. This revealed that Ti-64 was more tolerant to machining induced damage than Ti-407. The EBSD scans

revealed that for both alloys, increasing cutting speed reduced the visual depth of SPD in the machined surface, whereas increasing feed rate increased the depth of SPD. These observations were quantitatively assessed through analysing the LAGB misorientations within grains (i.e. the orientation difference between two adjacent measured points). The results have been presented in Figure 4.6. The highest density of LAGB was measured in the region closest to the machined surface decreasing towards the bulk material in line with expectations from previous studies by [35], [36]. The LAGB density decreases much quicker in the Ti-64 than the Ti-407 which agrees with the visual observations in Figure 4.5. The SPD in Figure 4.5d appears to extend further than the scanned EBSD map presented, based on the negligible change in LAGB density over the first 100 μm below the machined surface.

Labels have been used in Figure 4.6 to show where the qualitative visual assessment from Figure 4.5 lines up with the LAGB misorientation measurements. Comparing the visual inspection with the LAGB analysis, it is evident that the visual inspection greatly underestimates the extent of machining induced subsurface deformation.

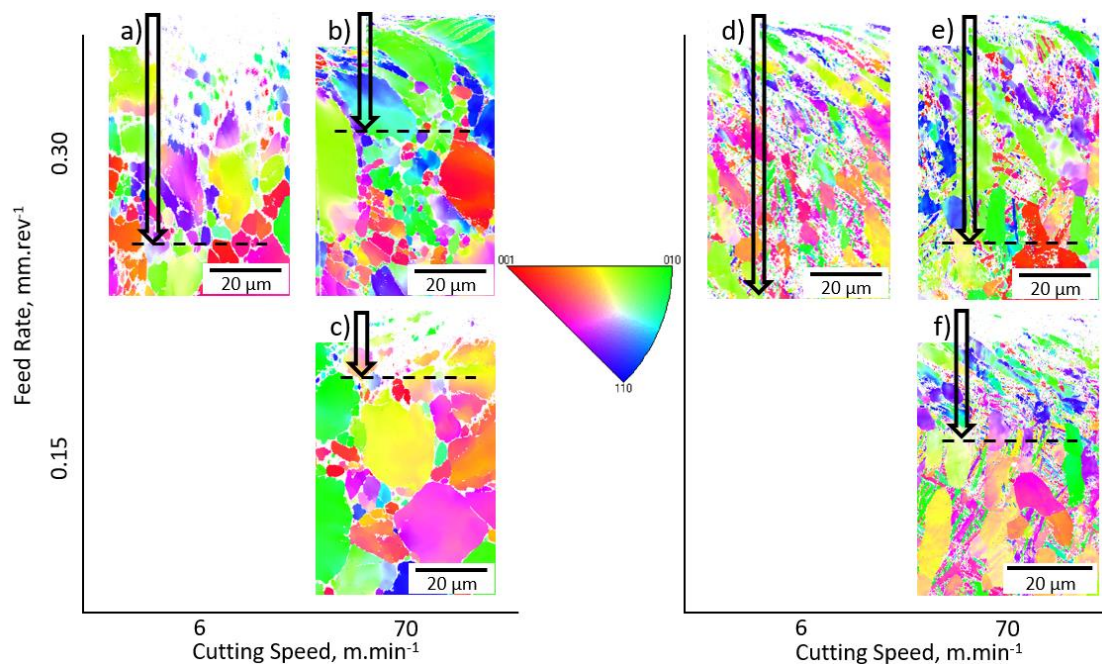


Figure 4.5: Following machining, EBSD scans of the subsurface shows imparted deformation in the surface of the Ti-64 (a-c) and Ti-407 (d-f) samples. The black dotted lines represent the maximum depth of SPD.

Table 4.3: Measured depth of severe plastic deformation (SPD) within the machined surface of Ti-64 and Ti-407 over the range of cutting parameters.

Cutting Speed, m.min ⁻¹	Feed Rate, mm.rev ⁻¹	Ti-64	Ti-407
		Severe Plastic Deformation, μm	Severe Plastic Deformation, μm
6	0.3	58	100+
40	0.3	39	75
70	0.3	20	50
40	0.15	28	45
70	0.15	14	30
55	0.23	25	52

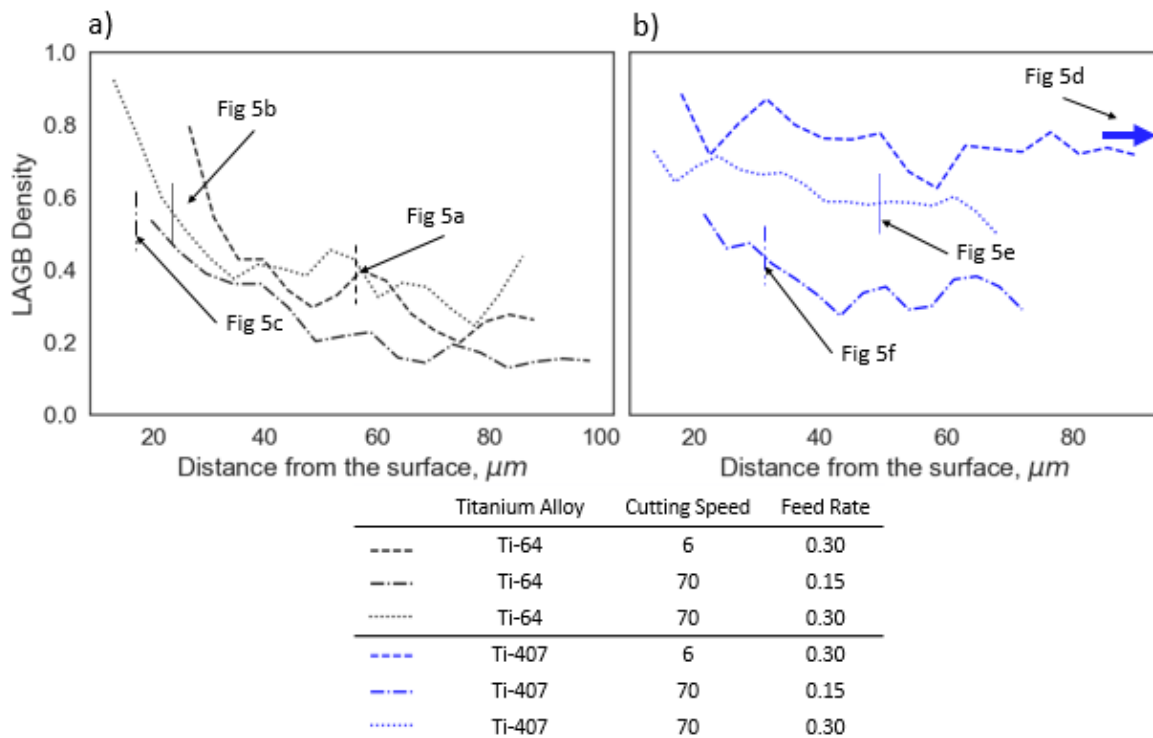


Figure 4.6: The change in LAGB density vs depth beneath the machined surface a) Ti-64 and b) Ti-407. The labels correlate with the qualitatively measured depth of SPD from Figure 4.5 which provide a visual comparison to the quantitatively measured depth of SPD using the LAGB in this figure. The arrow on the Fig 5d LAGB density line indicates that the depth of SPD extends further than was able to be imaged using EBSD.

4.3.1.3 Comparison of Tool Flank Wear

Tool flank wear has been studied to assess machinability of the two alloys. Figure 4.6 shows the tool flank edge at three cutting speeds for a feed rate of 0.30 mm.rev⁻¹. Greater flank wear was

recorded from machining Ti-64 (Figure 4.8a) than from machining Ti-407 (Figure 4.8b). This agrees with previous work by [21], which showed that the Ti-407 had a lower rate of tool wear than Ti-64 under the same cutting conditions for standard longitudinal turning operations. Figure 4.8a shows the flank wear measurements for Ti-64 as well as a dotted black line to express the boundary condition used in the machinability map. Three of the six Ti-64 tests failed the flank wear analysis, by exceeding the boundary condition, however none of the Ti-407 tests failed the flank wear boundary conditions.

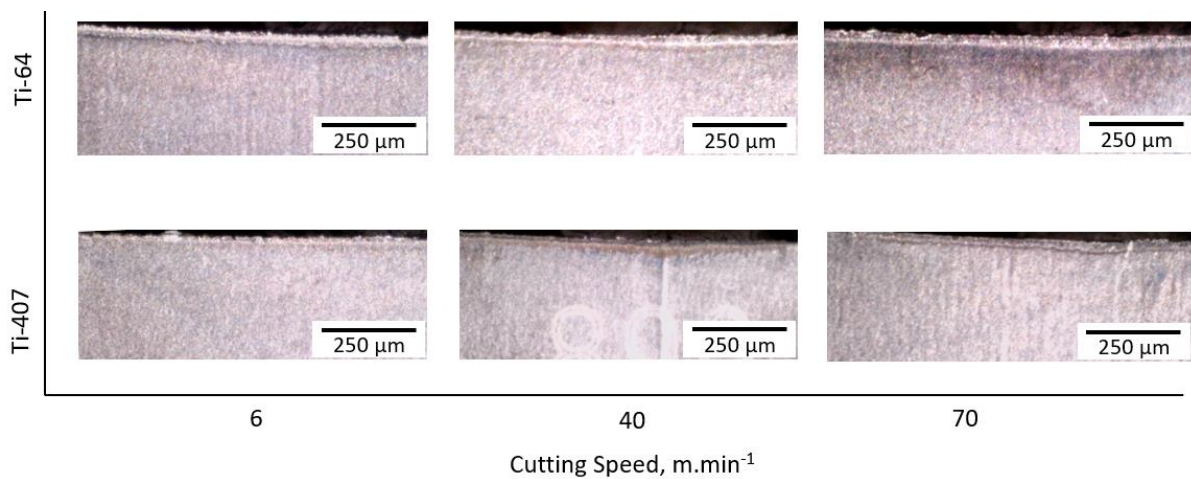


Figure 4.7: Photographs of the flank wear after (replicating plunge turning) machining Ti-64 and Ti-407 at the cutting speeds (6, 40 and 70 $m.min^{-1}$) and at a feed rate of $0.30 mm.rev^{-1}$.

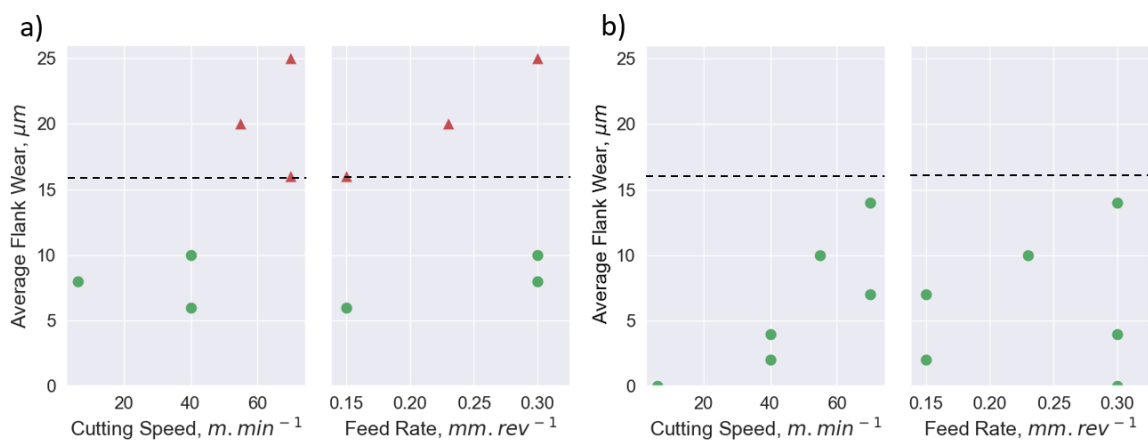


Figure 4.8: Flank wear measurements for a) Ti-64 and b) Ti-407. The black dotted line indicates the flank wear boundary condition set for the machinability map.

4.3.1.4 Comparison of chip morphology

Figure 4.9 and Figure 4.10 show the chip form of Ti-64 and Ti-407 respectively, at a range of cutting speeds and feed rates. In the case of both alloys, increasing the cutting speed increased the length of the chip, whilst the inverse was true for feed rate. Figure 4.9b shows how the machined chips are in a state of transition, between spiral and arc chip type morphologies, which demonstrates the sensitivity of the chip form on the cutting parameters.

Ti-407 forms long nested chips at all cutting speeds with the exception of Figure 4.10b, which formed a long helical chip. In general, long nested chips are undesirable for the manufacturing industry as they provide increased risk of the cutting tool fracture and the workpiece becoming scratched and damaged.

The chip morphology (in Figure 4.10a-c), changes from a nested, to helical and then a reversion back to a nested appearance in response to the increasing cutting speed from 6 to 70 $\text{m}\cdot\text{min}^{-1}$. This shows that the chip morphology is particularly sensitive to cutting speed.

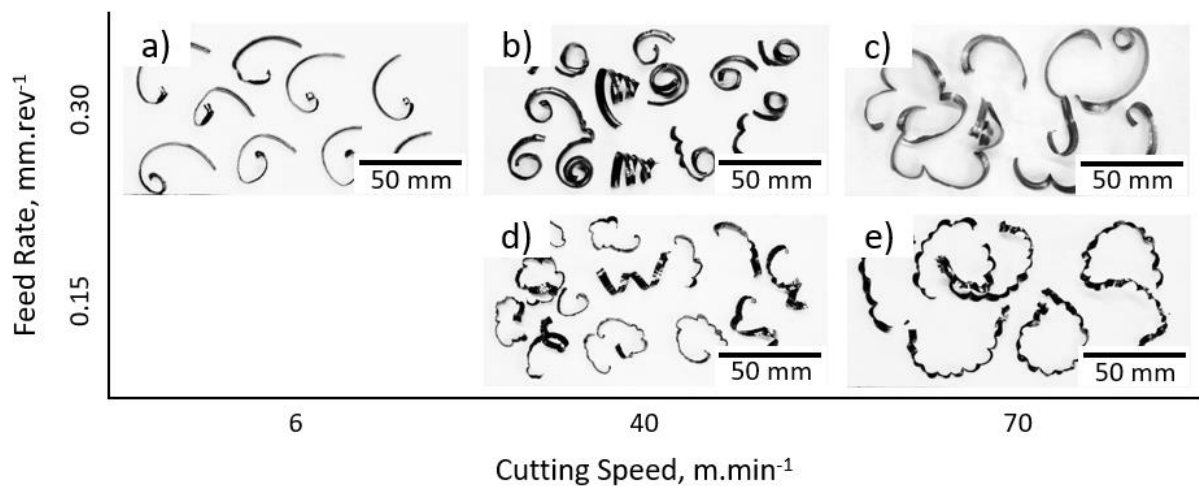


Figure 4.9: Photographs illustrating the change of Ti-64 chip morphology for a range of cutting speeds and feed rates from the orthogonal cutting tests.

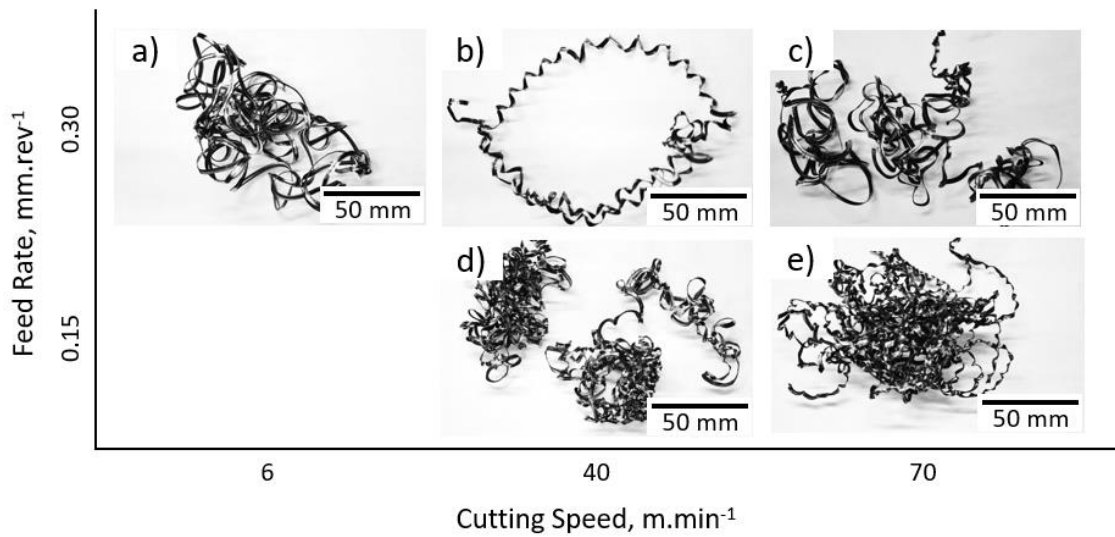


Figure 4.10: Photographs illustrating the change in Ti-407 chip morphology for a range of cutting speeds and feed rates from the orthogonal cutting tests.

4.3.1.5 Comparison of chip serration characteristics

Cross-sectional micrographs of the Ti-64 and Ti-407 chips have been presented in Figure 4.11 and Figure 4.12 respectively. Ti-64 forms the classical, serrated chips, with narrow ASBs between serrations, which are characteristics of serrated chips and indicators of thermoplastic instability during the cutting process. As the cutting speed increases, the serrations become more regular, the ASBs narrow slightly and micro-cracks develop between the serrations, which was also observed by Behera *et al.* [39] and Molinari *et al.* [40] in the machining of Inconel 718 and Ti-64 respectively.

The Ti-407 chip cross-sectional micrographs in Figure 4. are categorically different to Ti-64. The Ti-407 chips require a higher cutting speed for thermoplastic instability to activate compared to Ti-64. Figure 4.(a, d) presents chips in constant uniform shear where the absence of thermoplastic instability hinders the formation of ASBs and chip serrations, resulting in long nested chips, as shown in Figure 4.10(a, d). Increasing feed rate has a positive influence on the thermoplastic instability phenomenon, as shown between Figure 4.b and Figure 4.d. Again, increasing the cutting speed promotes thermoplastic instability as shown from the transition from continuous to serrated between Figure 4.a and Figure 4.c. It is therefore of interest to understand why the chips between Figure 4.10a and Figure 4.10c do not become more manageable. This suggests that uniform chip serration and ASBs are no guarantee of chip breakage, in contradiction to Bayoumi and Xie [41]. Clearly other factors are involved which negatively impact the breakability of Ti-407 chips.

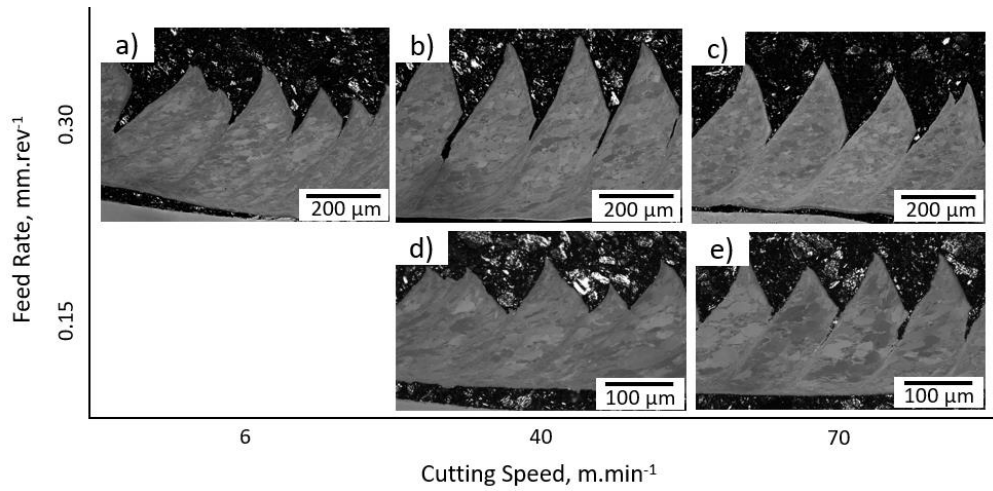


Figure 4.11: Cross-sectional light optical micrographs of the chip formation of Ti-64 at a range of cutting speeds and feed rates from the orthogonal cutting tests.

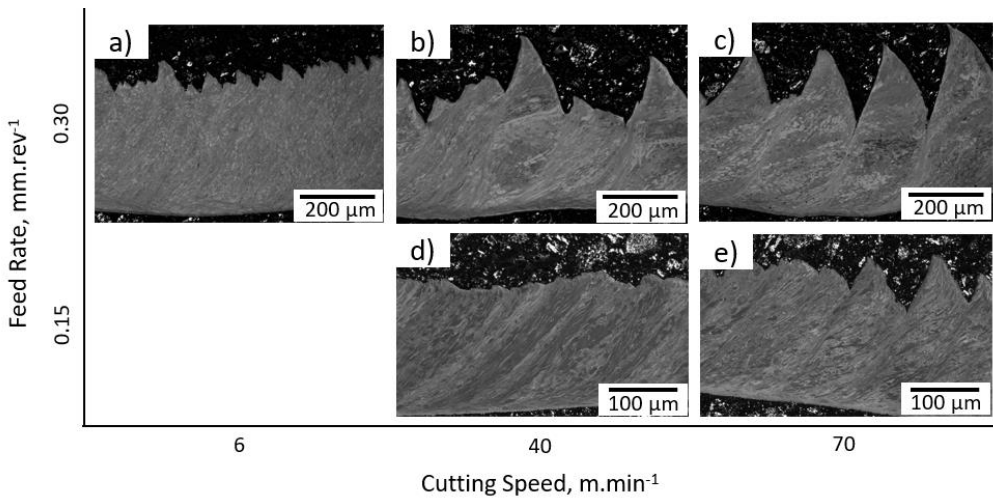


Figure 4.12: Cross-sectional light optical micrographs of the chip formation of Ti-407 at a range of cutting speeds and feed rates from the orthogonal cutting tests.

Table 4.4: The classification of chips into acceptable chip morphology =1, unacceptable chip morphology = 0 and transitioning chips = 0.5.

Cutting Speed, m.min ⁻¹	Feed Rate, mm.rev ⁻¹	Ti-64	Ti-407
		Chip Morphology	Chip Morphology
6	0.3	1	0
40	0.3	1	0.5
70	0.3	1	1
40	0.15	1	0
70	0.15	1	1
55	0.23	1	1

Table 4.4 shows the classification of the chip morphology for each of the tests which were subsequently used in the machinability model. The chips were either classified with a score of 0 if they were unacceptable for good chip control as seen in Figure 4.12a, 0.5 for those which were in a state of transition as shown in Figure 4.12b, or a score of 1 if they formed serrated chips as in Figure 4.12c. The Ti-64 produced serrated chips in all the tests therefore it was not possible to develop a Ti-64 chip morphology model. Ti-407 however, produced varied chip morphology ensuring a model could be created.

4.3.1.6 Comparison of chip shear band characteristics

Figure 4.13 and Figure 4.14 show the ASBs formed in the Ti-64 and Ti-407 chip respectively at high magnification. During the machining process, a significant proportion of the applied energy is converted into plastic deformation, which manifests as a highly distorted and unstable plastic region – leading to ASBs. Depending on a number of factors, including the thermal conductivity of the material and the cutting parameters used, the width and intensity of the ASBs can vary. Ti-64 forms very narrow, intense ASBs at all cutting parameters tested, thus offering ideal conditions for the formation of microvoids and cracks. Increasing the cutting speed narrows and intensifies the ASBs, whereas increasing the feed rate increases the width of the ASB very slightly in agreement with previous work by Miguélez *et al.* [30] and Molinari *et al.* [40]. Ti-407, in Figure 4.14(a, d), unlike Ti-64, undergoes constant uniform shear, which implies that the critical cutting speed for thermoplastic instability to occur is higher than Ti-64.

In both Ti-64 and Ti-407 at 70 m.min^{-1} , mechanical twins have nucleated in the low plastic strain regions adjacent to the SPD shear band region. This is an important observation which further validates the work of Kloenne *et al.* [17], who proposed that mechanical twinning in Ti-407 enabled greater strain accommodation and thus enhanced ductility. However, at the lower cutting speeds of 6 and 40 m.min^{-1} , there were no observed mechanical twins in and around the ASBs, in the Ti-64 and the Ti-407.

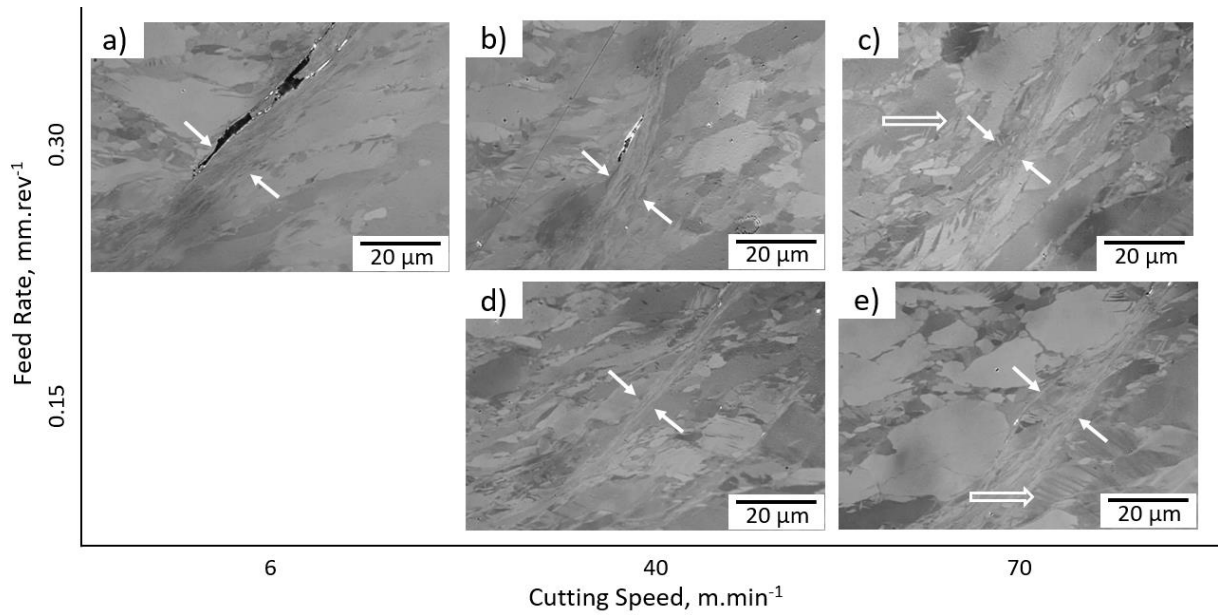


Figure 4.13: Light optical micrographs of the severely plastically deformed shear band region in the chip of Ti-64 for a range of cutting speeds and feed rates from the orthogonal cutting tests. Filled white arrows indicate the shear band region. The unfilled white arrows point to the mechanical twins which have nucleated around the ASB of the chip.

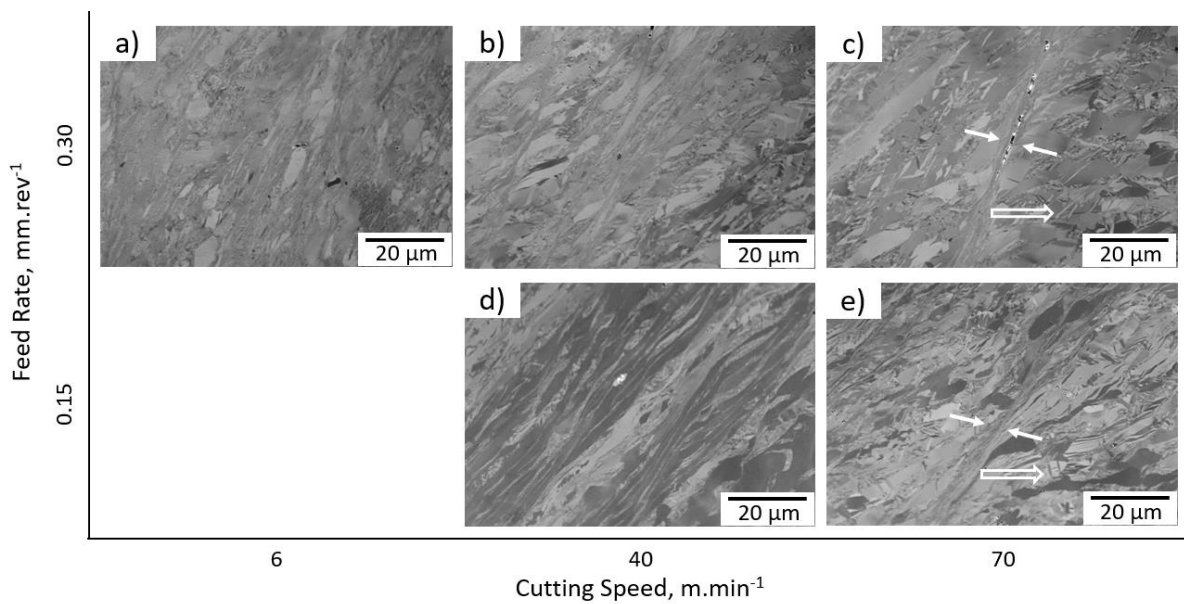


Figure 4.14: Light optical micrographs of the severely plastically deformed shear band region in the chip of Ti-407 for a range of cutting speeds and feed rates from the orthogonal cutting tests. Filled white arrows indicate the shear band region. The unfilled white arrows point to the mechanical twins which have nucleated around the ASB of the chip.

Table 4.5: The classification of chips into chip mechanical twins observed = 1, no chip mechanical twins observed = 0.

Cutting Speed, m.min ⁻¹	Feed Rate, mm.rev ⁻¹	Ti-64	Ti-407
		Chip Mechanical Twins	Chip Mechanical Twins
6	0.3	0	0
40	0.3	0	0
70	0.3	1	1
40	0.15	0	1
70	0.15	1	1
55	0.23	0	0

Table 4.5 shows the classification of chips based on whether they formed mechanical twins in the surrounding region of localised shear. A score of 0 was given to chips where mechanical twins were not formed in the surrounding region of the shear band, while a score of 1 was given for chips where mechanical twin were formed.

4.3.2 Section 2: Machinability Maps

The *machinability maps* constructed and presented in Figure 4.15 aim to capture the relationships between cutting speed and feed rate on the three key machinability criteria: tool wear, chip formation, and subsurface microstructural features.

Table 4.6: The boundary conditions set for the machinability map

	Ti-64	Ti-407
Flank Wear	16 µm	16 µm
Subsurface Twins	25 µm	35 µm
Severe Plastic Deformation	50 µm	70 µm
Chip Morphology	0 (Not Acceptable) → 1 (Acceptable)	
Chip Mechanical Twins	0 (No Twins) – 1 (Twins)	

A set of boundary conditions listed in Table 4.6 were used as values to pass or fail each machinability output. The flank wear boundary condition was set at 16 µm. This limit was based on two key points: (1) that the flank wear limit was 250 µm, and (2) that after 15 minutes the flank wear limit would be reached. This is a typical set of a conditions for a V15 tool life study, similar to the work published in Ref. [16], [42]–[44]. Of course it is difficult to draw conclusions about the tool life from

such a short test, especially as other tool wear mechanisms, such as crater wear and plastic deformation become more dominant later in the tool life. However the short tests do offer an indication of the tool flank wear rate of each alloy, whilst excluding other tool wear mechanisms. The subsurface deformation boundary conditions for the Ti-64 were similar to those used for industrial specifications. Due to the novelty of the Ti-407 alloy, there are currently no industry standards for machining this material. In this case, the boundary conditions were set as a percentage of the strain achieved at fracture for Ti-407 relative to Ti-64, based on previous results by Dredge *et al.* [21] in the same microstructural conditions. The results showed that Ti-407 fractured at a strain 40% higher than Ti-64. This limit of SPD and mechanical twinning has been defined in this work for the purpose of developing the machinability map. However further mechanical testing on Ti-407 would be required to propose an industrial specification for subsurface features to quantify at what depth or density such features become damaging to the longevity of a component. The boundary conditions for chip formation were determined based on the individual effects of chip morphology and chip mechanical twins on overall chip control.

Having calculated the unknown coefficients from Equation 4.1, the boundary conditions were set as \hat{y}_1 and the values of v and f were calculated to give a line across the machinability map where each condition either passed or failed.

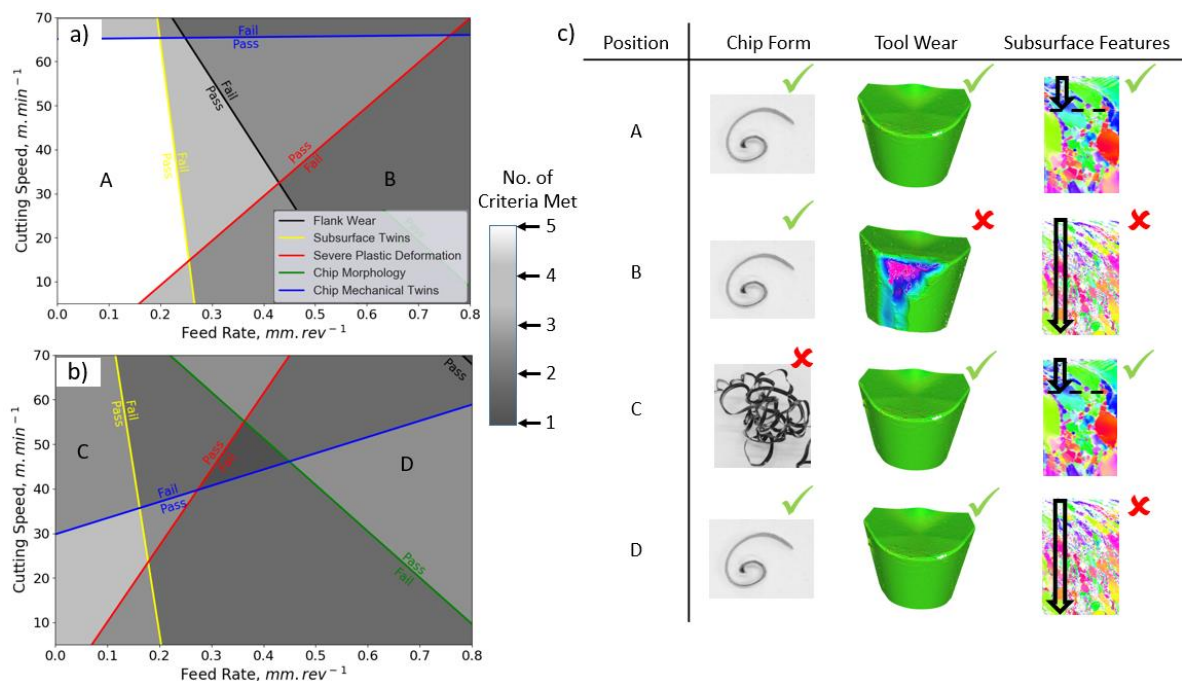


Figure 4.15: Machinability maps based on three criteria; chip form, tool wear and subsurface features in order to directly determine the relative machinability of a) Ti-64 and b) Ti-407. c) A summary and example of the pass/fail assessment of the three key machinability criteria at four different positions on the machinability maps in a) and b).

Table 4.7: Ti-64 machinability map parameters (β_0 , β_1 and a) used for each of machinability outputs along with the statistical significance, p and the Adjusted R² value of each line.

	Flank Wear	Subsurface Twins	Severe Plastic Deformation
β_0	0.31	0.15	-0.57
β_1	50.49	133.8	57.9
a	-12.98	-11.37	43.7
$p - value$	0.039	0.003	0.0004
Adjusted R ²	0.81	0.97	0.99

Table 4.8: Ti-64 machinability map parameters (β_0 , β_1 and a) for the chip mechanical twins line found using the Linear SVM model and the corresponding accuracy of the model

	Chip Mechanical Twins
β_0	-0.017
β_1	0
a	1.107
Accuracy, %	100

Table 4.9: Ti-407 machinability map parameters (β_0 , β_1 and a) used for each of machinability outputs along with the statistical significance, p , and the Adjusted R² value of each line.

	Flank Wear	Subsurface Twins	Severe Plastic Deformation	Chip Morphology
β_0	0.20	0.48	-0.73	0.02
β_1	29.04	355.1	170.5	2.05
a	-10.47	-41.2	52.09	-0.83
$p - value$	0.04	0.004	0.001	0.06
Adjusted R ²	0.81	0.96	0.98	0.77

Table 4.10: Ti-407 machinability map parameters (β_0 , β_1 and a) for the chip mechanical twins line found using the Linear SVM model and the corresponding accuracy of the model.

	Chip Mechanical Twins
β_0	-0.027
β_1	0.982
a	0.804
Accuracy, %	83.3

As shown in Figure 4.15a, Ti-64 has a large machinability processing window, where all the key criteria are met. In contrast, Ti-407 in Figure 4.15b has no region on the machinability map where the full criteria are met. There is one region where four of the five criteria have been met and three small regions where three of the five criteria have been met with conflicting requirements to satisfy the conditions of (i) subsurface microstructural features and (ii) chip formation features. The machinability map shows that tool wear is not an issue for Ti-407, whilst tool wear does limit the maximum MRR of Ti-64. There are very few chip control issues from machining Ti-64 at any of the tested cutting parameters. However the increase in chip length when cutting at $70 \text{ m}\cdot\text{min}^{-1}$ coincides with the formation of chip mechanical twins. The Ti-64 forms serrated chips very easily at all cutting parameters tested and therefore this factor does not feature on the machinability map in Figure 4.15a.

The factor which limits Ti-64's MRR is the formation of mechanical twins in the subsurface of the workpiece and to a lesser extent around the chip shear band, which confirms the findings of Fitzner *et al.* [45] and Marshall *et al.* [46]. However this disagrees with previous work by Lütjering *et al.*, [20] who suggested that 6.0 wt.% aluminium in titanium alloys would suppress the formation of mechanical twins entirely.

The machinability map has been used to quantify machinability of the titanium alloys as a percentage of the total area of the map where optimal parameters have been found, i.e. the area where all the boundary conditions were met. In the case of Ti-64 this area is attributed to "zone A" in Figure 4.15a. For Ti-407 in Figure 4.15b there is no corresponding area where optimal parameters have been located. Therefore for the range of cutting parameters in this study, the machinability of Ti-64 and Ti-407 was calculated as 26.1 % and 0%, respectively.

A composite figure has been produced in Figure 4.15c to present the predicted relative machining performance of these two alloys from different locations in the map. The composite figure at position (A) predicts that the Ti-64 would produce good chips, maintain low rates of tool wear and acceptable subsurface integrity. At position (B), good chip formation is predicted, however high rates of tool wear and excessive amounts of subsurface microstructural features or damage are predicted. In similar regions of the Ti-407 map, position (C) would produce a poor chip form, but result in lower rates of tool wear and acceptable subsurface microstructural features. But increasing the feed rate towards position (D) predicts a marked change in the machining characteristics where the chip form will improve dramatically, although the level of subsurface microstructural damage will be compromised. These predictions (based on the experimental data) highlight that at no point within the range of cutting parameters on the machinability map is it possible for Ti-407 to provide conditions where all of the selected boundary conditions can be met.

The parameters of the multi-variable linear regression and the linear SVM used to create the lines for each factor of the machinability map are provided in Table 4.7-4.10 along with the statistical

significance and accuracy of the data. Table 4.7 and Table 4.9 show that all the regression relationships are of statistical significance as the p-values are less than 0.05, except for Table 4.9 'Chip Morphology' where the p-value is 0.06. Further testing would be required to test the significance of the relationship between cutting parameters and chip morphology to ensure this linear regression is true.

4.4 Discussion

The discussion has been presented in two parts. The first part examines the machinability maps and what they tell us about each of these alloys. The second part investigates chip control and provides a fundamental understanding of the reasons behind the poor chip control of Ti-407.

4.4.1 Machinability Maps

The machinability maps presented in this work can be used as a tool by researchers and the manufacturing supply chain to visualise the effects of machinability variables against cutting parameters. Through the machinability maps, regions of both poor machinability can be avoided and regions of optimum machinability can be further investigated. Of course other factors i.e. alloy morphology, tool geometry, coolant pressure and chip-breakers will provide secondary variability and resolution to such maps. Though the general trends, which are in essence properties of each titanium alloy are predicted to remain. The machinability maps confirm that Ti-407 is more machinable than Ti-64 with respect to tool wear which was a desired outcome from the development of this alloy. This benefit may be offset by greater subsurface microstructural features and/ or by challenging chip formation.

4.4.2 Ti-407 Chip Control

The challenge of machining Ti-407 to produce manageable chips is linked to a number of factors: thermal conductivity, chemical composition, microstructure and mechanical properties. These affect the cutting parameters that can be used to machine titanium alloys efficiently.

According to James *et al.* [16] the thermal conductivity of Ti-407 is almost double that of Ti-64 at room temperature. Zang *et al.* [47] showed that as the thermal conductivity of the titanium alloy increases, the width of the ASBs also increases. This is due to the improved ability of the alloy to dissipate heat away from the contact region of the tool and the workpiece. With greater diffusion of heat, the thermal softening and work hardening phenomena are distributed over a wider localised region. This reduces the intensity, yet simultaneously increases the width of the ASBs which consequently contains less plastic deformation, making chip fracture less likely. Increasing the cutting speed increases

the temperature at the interface between the cutting tool and the workpiece, promoting thermal softening and work hardening. A balance of both phenomena are essential for thermoplastic instability and the facilitation of ASBs and serrated chip formation. As reported by Komanduri and Hou [27], a critical cutting speed must be reached to initiate thermoplastic instability. With a further increase in cutting speed, a higher strain is required to cause chip fracture as the localised temperature at the tool edge increases. This leads to higher plastic strain-energy, which has been shown previously in compression tests by Nguyen *et al.* [48], and observed in a machining set up by Davis *et al.* [49]. Importantly, increasing the cutting speed reduces the amount of strain accommodated in the chip, as the time for the generation of dislocations into the chip and the accommodation of plastic deformation is reduced. This is observed by the narrower shear bands and the higher frequency of chip serration, explaining why longer chips are observed at higher cutting speeds in Figure 4.9 and Figure 4.10, as identified by Cotterell and Byrne. [28].

In order to accommodate plastic strain, either slip or mechanical twinning occurs. Mechanical twinning involves a single coordinated movement of a large number of atoms, whereas slip involves the movement of a sequence of atoms. Mechanical twinning is often preferable to slip when resistance to slip is very large in certain directions. Furthermore twinning is prevalent at very high strain rates [50], [51]. As shown in studies by Dredge *et al.* [21] greater plastic strain is required to fracture Ti-407 as a result of the alloy's propensity to mechanically twin rather than slip - due to the low aluminium content. Machining at higher cutting speeds (and thus, higher rates of deformation) induces a greater density of mechanical twins forming in the chip and subsurface of the workpiece. Conversely, increasing the feed rate has the opposite effect to cutting speed, as it lowers the chip serration frequency and widens the ASB, and thus more plastic strain is accommodated in the chip. Furthermore, increasing the feed rate increases the time per serration which favours deformation slip - which is preferential for chip fracture. The formation of twins negatively affects the chip breakability by increasing the accommodation of plastic strain, and raising the required strain-energy to cause chip fracture.

The dominance of twins as a deformation mechanism in Ti-407 is largely due to the alloy chemistry. Ti-407 has a relatively low aluminium content (of 0.85 wt. %) compared to Ti-64 (at 6 wt. %). Marshall *et al.* [8] showed that high aluminium content in titanium alloys plays a major role in suppressing the formation of mechanical twins in both the chip and the workpiece subsurface during high strain rate plastic deformation processes such as machining. Fitzner *et al.* [45] determined that decreasing aluminium content suppressed some twin types, but encouraged others to form. The $\{11\bar{2}2\}$ compression twins and the $\{10\bar{1}2\}$ tensile twins both occurred less frequently with increasing aluminium content. The $\{11\bar{2}1\}$ tensile twins occurred more frequently with increasing aluminium content. Kloenne *et al.* [17] identified that the $\{10\bar{1}2\}$ was the most dominant twin to form during the deformation of Ti-407, and also concluded that the mechanical twins were the major mechanism for Ti-

407's ability to accommodate greater strain before fracturing. This explains the enhanced ductility of Ti-407 compared to Ti-64.

It is well researched [52]–[55] that grain size has a significant effect on twinning behaviour by establishing that a larger, coarser grain will typically twin easier than for a smaller, finer grain. It is therefore contrary to the research that the smaller grain size of Ti-407 relative to Ti-64 promotes a greater propensity to form twins. This highlights the significance of the chemical composition as a primary factor affecting the deformation properties of a material.

In high strain rate deformation regimes, the current understanding proposes that twinning is the preferential deformation mechanism because it occurs faster than slip mechanisms [56]. Contrary to this, Nemat-Nasser *et al.* [57] conducted research investigating mechanical twins using uniaxial compression test methodologies at elevated temperatures (above 700K) and found that increasing temperatures resulted in a reduction in the volume of mechanical twins. Kloenne *et al.* [17] pointed out that the most dominant twin type in Ti-407 deformation was the tension twin $\{10\bar{1}2\}$ which are not temperature dependent unlike other twins according to Chapuis *et al.* [58]. This may explain why twins are still the dominant deformation mechanism at elevated temperatures - generated through higher cutting speeds and strain rates.

At low feeds and higher cutting speeds, it could be predicted that there would be an increase in the number of twin nucleation sites resulting in a larger volume fraction of twins [59]. This would allow greater accommodation of plastic strain and suppress the point of fracture and thus, chip breakage.

4.5 Conclusion

This investigation into machining titanium alloys Ti-64 (in the Mill Annealed condition) and Ti-407 (in the Solution Heat Treated and Aged condition) has led to a greater understanding of the challenges of producing manageable chips and led to the development of machinability maps that provide a comprehensive analysis of the machinability of these particular titanium alloys in these specified microstructural conditions, considering: tool wear, chip form and subsurface microstructural features.

The following conclusions can be drawn from this study:

- 1) A machinability map has been developed to visualise the relationships between the key machinability factors for Ti-64 and Ti-407.

- 2) The machinability map indicates that Ti-407 has better machinability with respect to tool wear, however Ti-64 has better machinability with respect to chip formation and subsurface microstructural features.
- 3) According to the machinability map, there is a region of optimal machinability for Ti-64 but not for Ti-407 within this range of cutting parameters and in these particular microstructural conditions.
- 4) The machinability map does not show a region of ideal cutting parameters for Ti-407 but this does not mean that Ti-407 could not be acceptably machined in a real-world industrial environment because the criteria for acceptable machining will vary from one manufacturing company to another.
- 5) Improved chip breakability can be achieved when machining Ti-407 according to the machinability map, provided two conditions are met. Firstly, the feed rate needs to be high enough to induce sufficient plastic strain in each chip serration. Secondly, as shown in the machinability map, the ideal cutting speed to create controlled chips falls within a narrow range where both shear localisation is achieved and the formation of mechanical twins is avoided.
- 6) The poor chip control is due to two key reasons: firstly, a higher critical cutting speed is required to encourage thermoplastic-instability which could be due to the thermal conductivity of Ti-407 being greater than Ti-64, thus affecting the thermal softening capabilities of the alloy. Secondly, mechanical twins which can be prevalent during the chip forming process, increase the accommodation of strain prior to fracture.
- 7) Improving the chip control has a negative effect on subsurface microstructural features by increasing the depth of severe plastic deformation and mechanical twins.

References

- [1] A. Gittens, "ACI's World Airport Traffic Forecasts reveal the drivers of air transport demand growth on the path to 2040," ACI World, 2019. [Online]. Available: <https://www.internationalairportreview.com/article/106229/world-airport-traffic-forecasts-aci-world/>. [Accessed: 01-May-2020].
- [2] M. Peters, J. Kumpfert, C. H. Ward, and C. Leyens, "Titanium Alloys for Aerospace Applications," *Adv. Eng. Mater.*, vol. 5, no. 6, pp. 419–427, Jun. 2003.
- [3] H. K. Toenshoff, "Machinability," in *CIRP Encyclopedia of Production Engineering*, Berlin, Heidelberg: Springer Berlin Heidelberg, 2014, pp. 769–770.

- [4] A. R. Machado and J. Wallbank, "Machining of Titanium and its Alloys—a Review," *Proc. Inst. Mech. Eng. Part B J. Eng. Manuf.*, vol. 204, no. 1, pp. 53–60, 1990.
- [5] C. Veiga, J. P. Davim, and A. J. R. Loureiro, "Review on machinability of titanium alloys: The process perspective," *Rev. Adv. Mater. Sci.*, vol. 34, no. 2, pp. 148–164, 2013.
- [6] E. O. Ezugwu and Z. M. Wang, "Titanium alloys and their machinability—a review," *J. Mater. Process. Technol.*, vol. 68, no. 3, pp. 262–274, Aug. 1997.
- [7] X. Yang and C. R. Liu, "Machining titanium and its alloys," *Mach. Sci. Technol.*, vol. 3, no. 1, pp. 107–139, 1999.
- [8] L. Marshall, B. Wynne, S. Turner, and M. Jackson, "Influence of Aluminium Content on the Machinability and Subsurface Deformation Of Titanium Alloys," in *Proceedings of the 13th World Conference on Titanium*, Hoboken, NJ, USA: John Wiley & Sons, Inc., 2016, pp. 923–928.
- [9] P. J. Arrazola, A. Garay, L. M. Iriarte, M. Armendia, S. Marya, and F. Le Maître, "Machinability of titanium alloys (Ti6Al4V and Ti555.3)," *J. Mater. Process. Technol.*, vol. 209, no. 5, pp. 2223–2230, 2009.
- [10] N. Khanna, A. Garay, L. M. Iriarte, D. Soler, K. S. Sangwan, and P. J. Arrazola, "Effect of heat Treatment Conditions on the Machinability of Ti64 and Ti54M Alloys," *Procedia CIRP*, vol. 1, pp. 477–482, 2012.
- [11] N. Khanna and K. S. Sangwan, "Comparative machinability study on Ti54M titanium alloy in different heat treatment conditions," *Proc. Inst. Mech. Eng. Part B J. Eng. Manuf.*, vol. 227, no. 1, pp. 96–101, Jan. 2013.
- [12] N. Khanna and K. S. Sangwan, "Machinability analysis of heat treated Ti64, Ti54M and Ti10.2.3 titanium alloys," *Int. J. Precis. Eng. Manuf.*, vol. 14, no. 5, pp. 719–724, May 2013.
- [13] M. Armendia, P. Osborne, A. Garay, J. Belloso, S. Turner, and P. Arrazola, "Influence of Heat Treatment on the Machinability of Titanium Alloys," *Mater. Manuf. Process.*, vol. 27, no. 4, pp. 457–461, 2012.
- [14] M. Armendia, A. Garay, L. M. Iriarte, and P. J. Arrazola, "Comparison of the machinabilities of Ti6Al4V and TIMETAL® 54M using uncoated WC–Co tools," *J. Mater. Process. Technol.*, vol. 210, no. 2, pp. 197–203, Jan. 2010.
- [15] S. I. Jaffery and P. T. Mativenga, "Assessment of the machinability of Ti-6Al-4V alloy using the wear map approach," *Int. J. Adv. Manuf. Technol.*, vol. 40, no. 7–8, pp. 687–696, 2009.

- [16] S. James, Y. Kosaka, R. Thomas, and P. Garratt, "Timetal® 407: A Titanium Alloy to Enable Cost Reduction," in Proceedings of the 13th World Conference on Titanium, 2016, pp. 721–725.
- [17] Z. Kloenne, G. Viswanathan, M. Thomas, M. Loretto, and H. Fraser, "A Comparative Study on the Substructure Evolution and Mechanical Properties of TIMETAL 407 and Ti-64," in The 14th World Conference on Titanium Proceedings, 2019, pp. 1–6.
- [18] D. J. Truax and C. J. McMahon, "Plastic behavior of titanium-aluminum alloys," *Mater. Sci. Eng.*, vol. 13, no. 2, pp. 125–139, Feb. 1974.
- [19] J. C. Williams, R. G. Baggerly, and N. E. Paton, "Deformation behavior of HCP Ti-Al alloy single crystals," *Metall. Mater. Trans. A Phys. Metall. Mater. Sci.*, vol. 33, no. 3, pp. 837–850, 2002.
- [20] G. Lütjering and J. C. Williams, *Titanium*, 2nd ed. Springer, 2007.
- [21] C. Dredge, R. M'Saoubi, B. Thomas, O. Hatt, M. Thomas, and M. Jackson, "A low-cost machinability approach to accelerate titanium alloy development," *Proc. Inst. Mech. Eng. Part B J. Eng. Manuf.*, Jul. 2020.
- [22] M. Groover, *Fundamentals of Modern Manufacturing Materials, Processes and Systems*, 4th Editio. John Wiley & Sons Inc, 2011.
- [23] E. Booser, *CRC Handbook of Lubrication and Tribology, Volume III: Monitoring*. CRC Press, 1993.
- [24] R. Komanduri and B. F. Von Turkovich, "New observations on the mechanism of chip formation when machining titanium alloys," *Wear*, vol. 69, no. 2, pp. 179–188, Jun. 1981.
- [25] S. Zhang, J. Li, X. Zhu, and H. Lv, "Saw-tooth chip formation and its effect on cutting force fluctuation in turning of Inconel 718," *Int. J. Precis. Eng. Manuf.*, vol. 14, no. 6, pp. 957–963, Jun. 2013.
- [26] C. Gao and L. Zhang, "Effect of cutting conditions on the serrated chip formation in high-speed machining," *Mach. Sci. Technol.*, vol. 17, no. 1, pp. 26–40, Jan. 2013.
- [27] R. Komanduri and Z. Hou, "On Thermoplastic Shear Instability in the Machining of a Titanium Alloy (Ti-6Al-4V)," *Metall. Mater. Trans. A*, vol. 33, no. 9, pp. 1–16, 2002.
- [28] M. Cotterell and G. Byrne, "Dynamics of chip formation during orthogonal cutting of titanium alloy Ti-6Al-4V," *CIRP Ann.*, vol. 57, no. 1, pp. 93–96, Jan. 2008.

- [29] S. Sun, M. Brandt, and M. S. Dargusch, "Characteristics of cutting forces and chip formation in machining of titanium alloys," *Int. J. Mach. Tools Manuf.*, 2009.
- [30] M. H. Miguélez, X. Soldani, and A. Molinari, "Analysis of adiabatic shear banding in orthogonal cutting of Ti alloy," *Int. J. Mech. Sci.*, vol. 75, pp. 212–222, Oct. 2013.
- [31] M. D. F. Rahman, "Stress and Strain Distributions during Machining of Ti-6Al-4V at Ambient and Cryogenic Temperatures," University of Windsor, 2014.
- [32] H. E. Chandler, *Metals Handbook*. 1978.
- [33] Y. H. Çelik and A. Karabiyik, "Effect of cutting parameters on machining surface and cutting tool in milling of Ti-6Al-4V alloy," *Indian J. Eng. Mater. Sci.*, vol. 23, no. 5, pp. 349–356, 2016.
- [34] J. Sun, S. Huang, T. Wang, and W. Chen, "Research on surface integrity of turning titanium alloy TB6," *Procedia CIRP*, vol. 71, pp. 484–489, Jan. 2018.
- [35] Z. Chen et al., "Effect of thermal exposure on microstructure and nano-hardness of broached Inconel 718," *MATEC Web Conf.*, vol. 14, p. 08002, Aug. 2014.
- [36] J. Zhou, V. Bushlya, R. L. Peng, Z. Chen, S. Johansson, and J. E. Stahl, "Analysis of Subsurface Microstructure and Residual Stresses in Machined Inconel 718 with PCBN and Al₂O₃-SiC_w Tools," *Procedia CIRP*, vol. 13, pp. 150–155, 2014.
- [37] P. G. Partridge, "Cyclic twinning in fatigued close-packed hexagonal metals," *Philos. Mag. A J. Theor. Exp. Appl. Phys.*, vol. 12, no. 119, pp. 1043–1054, Nov. 1965.
- [38] X. Tan, H. Guo, H. Gu, C. Laird, and N. D. H. Munroe, "Cyclic deformation behavior of high-purity titanium single crystals: Part II. Microstructure and mechanism," *Metall. Mater. Trans. A*, vol. 29, no. 2, pp. 513–518, Feb. 1998.
- [39] B. Chandra Behera, C. Sudarsan Ghosh, and V. R. Paruchuri, "Study of saw-tooth chip in machining of Inconel 718 by metallographic technique," *Mach. Sci. Technol.*, vol. 23, no. 3, pp. 431–454, May 2019.
- [40] A. Molinari, C. Musquar, and G. Sutter, "Adiabatic shear banding in high speed machining of Ti-6Al-4V: experiments and modeling," *Int. J. Plast.*, vol. 18, no. 4, pp. 443–459, Apr. 2002.
- [41] A. E. Bayoumi and J. Q. Xie, "Some metallurgical aspects of chip formation in cutting Ti-6wt.%Al-4wt.%V alloy," *Mater. Sci. Eng. A*, vol. 190, no. 1–2, pp. 173–180, Jan. 1995.

- [42] C. M. Taylor, S. G. Abrego Hernandez, M. Marshall, and M. Broderick, "Cutting fluid application for titanium alloys Ti-6Al-4V and Ti-10V-2Fe-3Al in a finish turning process," *Procedia CIRP*, vol. 77, pp. 441–444, 2018.
- [43] O. Hatt, P. Crawforth, and M. Jackson, "On the mechanism of tool crater wear during titanium alloy machining," *Wear*, vol. 374, pp. 15–20, 2017.
- [44] T. Bakša, T. Kroupa, P. Hanzl, and M. Zetek, "Durability of Cutting Tools during Machining of Very Hard and Solid Materials," *Procedia Eng.*, vol. 100, pp. 1414–1423, 2015.
- [45] A. Fitzner, M. Thomas, J. Q. Fonseca, S. Y. Zhang, J. Kelleher, and M. Preuss, "The Effect of Aluminium on Deformation and Twinning in Alpha Titanium: The ND Case," in *Proceedings of the 13th World Conference on Titanium*, Hoboken, NJ, USA: John Wiley & Sons, Inc., 2016, pp. 1051–1055.
- [46] L. Marshall, "The influence of aluminium additions on titanium during machining through the application of a novel orthogonal cutting test method," University of Sheffield, 2014.
- [47] J. Zang, J. Zhao, A. Li, and J. Pang, "Serrated chip formation mechanism analysis for machining of titanium alloy Ti-6Al-4V based on thermal property," *Int. J. Adv. Manuf. Technol.*, vol. 98, no. 1–4, pp. 119–127, 2018.
- [48] D. T. Nguyen, Y. S. Kim, and D. W. Jung, "Flow stress equations of Ti-6Al-4V titanium alloy sheet at elevated temperatures," *Int. J. Precis. Eng. Manuf.*, vol. 13, no. 5, pp. 747–751, May 2012.
- [49] B. Davis, D. Dabrow, P. Ifju, G. Xiao, S. Y. Liang, and Y. Huang, "Study of the Shear Strain and Shear Strain Rate Progression During Titanium Machining," *J. Manuf. Sci. Eng.*, vol. 140, no. 5, May 2018.
- [50] J. P. Hirth, J. Lothe, and T. Mura, "Theory of Dislocations (2nd ed.)," *J. Appl. Mech.*, vol. 50, no. 2, pp. 476–477, Jun. 1983.
- [51] J. W. Christian and S. Mahajan, "Deformation twinning," *Prog. Mater. Sci.*, vol. 39, no. 1–2, pp. 1–157, 1995.
- [52] A. Ghaderi and M. R. Barnett, "Sensitivity of deformation twinning to grain size in titanium and magnesium," *Acta Mater.*, vol. 59, no. 20, pp. 7824–7839, Dec. 2011.
- [53] P. Dobroň, F. Chmelík, S. Yi, K. Parfenenko, D. Letzig, and J. Bohlen, "Grain size effects on deformation twinning in an extruded magnesium alloy tested in compression," *Scr. Mater.*, vol. 65, no. 5, pp. 424–427, 2011.

- [54] Y. T. Zhu, X. Z. Liao, X. L. Wu, and J. Narayan, "Grain size effect on deformation twinning and detwinning," *J. Mater. Sci.*, vol. 48, no. 13, pp. 4467–4475, Jul. 2013.
- [55] Z. W. Huang, P. L. Yong, H. Zhou, and Y. S. Li, "Grain size effect on deformation mechanisms and mechanical properties of titanium," *Mater. Sci. Eng. A*, vol. 773, p. 138721, 2020.
- [56] J. Jeong, M. Alfreider, R. Konetschnik, D. Kiener, and S. H. Oh, "In-situ TEM observation of $\{101\bar{2}\}$ twin-dominated deformation of Mg pillars: Twinning mechanism, size effects and rate dependency," *Acta Mater.*, vol. 158, pp. 407–421, Oct. 2018.
- [57] S. Nemat-Nasser, W. G. Guo, and J. Y. Cheng, "Mechanical properties and deformation mechanisms of a commercially pure titanium," *Acta Mater.*, vol. 47, no. 13, pp. 3705–3720, Oct. 1999.
- [58] A. Chapuis and J. H. Driver, "Temperature dependency of slip and twinning in plane strain compressed magnesium single crystals," *Acta Mater.*, vol. 59, no. 5, pp. 1986–1994, Mar. 2011.
- [59] M. Ahmed, D. Wexler, G. Casillas, D. G. Savvakina, and E. V. Pereloma, "Strain rate dependence of deformation-induced transformation and twinning in a metastable titanium alloy," *Acta Mater.*, vol. 104, pp. 190–200, Feb. 2016.

Validation of “Machinability Map” Approach: Improving Chip Control During the Machining of Titanium Alloy Ti-407

5

5.1 Introduction

The need for greater efficiency and cost savings in the aerospace industry is more important than ever, given the recent global pandemic. This is no more true than in the manufacturing of titanium alloy components, where the machining stage alone can contribute up to 60% of a titanium component’s final cost [1]. As companies scale back operations, and look to drive down costs, it is important to consolidate, look forward and try to improve productivity. To therefore machine efficiently one must understand the machining characteristics of the alloy. Depending on the final requirement of the component and the cutting conditions employed, i.e. tooling, coolant, operation etc. there are a number of cutting parameters, which when combined produce a set of very distinctive results in terms of chip form, tool wear mechanisms and machining induced deformation. In order to optimise the machining operation, it is necessary to consider all the machinability outputs together.

In recent years, a number of optimisation studies have been developed for machining. Makadia and Nanavati [2] used a Response Surface Methodology (RSM) to investigate surface roughness for turning operations. RSM is a statistical method employed to help fit models developed by Box and Wilson [3]. Tsourveloudis [4] used RSM and a fuzzy logic system through the Adaptive Neuro-Fuzzy Inference System (ANFIS) to predict the surface roughness of a machined surface. Some authors [5]–[7] have used the Taguchi method to optimise cutting parameters including: cutting speed, feed rate and depth of cut, again with the goal of reducing surface roughness. However, with all of these methods they require a great number of data points to ensure a good model fit, and so far they have failed to account for other machining outputs, including: tool wear, chip form and machining induced surface damage. To conduct such an extensive study would require a large amount of material, time, cost and labour to execute.

The machinability map is a simple but effective map to indicate the key machining trends of titanium alloys, for the purpose of optimising the parameters specific to a machining operation in order to increase output and efficiency. The machinability map comprises the key machining characteristics of tool wear, chip form and machining induced surface deformation and could play an important role in both the future machining optimisation and standardisation of emerging alloys, as well as ensuring optimisations are achieved in machining of current alloys. The machinability map developed in this study (see section 4.3.2) achieves this through identifying regions on the map where all machining

characteristics are satisfied, and utilising these regions to increase productivity within the bounds of industrial machining specifications such as maximum depth of severe plastic deformation (SPD).

The machinability map has been utilised in this study to analyse the machining characteristics of the emerging titanium alloy Ti-407, in a machining setup as close to representative of the industrial process as possible. The aim of this work was to resolve the challenge of chip management during machining of Ti-407 and implement these findings within industrial-scale process

5.2 Methodology

5.2.1 Pre-processing of billet material

As-forged Ti-407 (Ti-0.85Al-3.9V-0.15O-0.25Si-0.25Fe) billet material of diameter 225 mm was provided by TIMET UK. Figure 5.1a shows the microstructure of the as-forged material, which consists solely of globularised primary alpha grains. Within the grains there are mechanical twins (white arrows) and thus retained stresses within a proportion of the grains from the upstream billet processing stages. In order to stress relieve the billet, a solution treatment and age (STA) was performed as recommended by the industrial sponsors. After completing the heat treatment a disk of 25 mm was cut from the end of the billet which was etched in order to reveal the general microstructure and ensure consistency across the billet. Figure 5.1b shows the microstructure from a coupon cut from the outer 20 mm of the billet. The retained stresses in the material have been annihilated by the annealing process to leave a microstructure consisting of a lower volume fraction of primary alpha grains in a transformed beta with a Widmanstätten secondary alpha morphology. Figure 5.2 shows a comparison of the STA microstructure and the ImageJ analysis (of the same section) used to calculate the fraction of primary alpha in the material. The primary alpha in the outer 20 mm of the billet ranges from 35-45%, with the other 55-65% being the transformed beta matrix. Figure 5.3 presents a composite image showing the etched billet cross-section highlighting how the microstructure changes from the centre of the billet to the outer edge. Closer inspection of the microstructure using light optical microscopy, shows the variation in the microstructure across the billet due to differing cooling rates across the radius of the billet. From the centre to the outer edge, the microstructure evolves from roughly 35-45% primary alpha at the outer edge to nearly 90% primary alpha at the centre. In order for the machining validation experiments to be truly representative of material machined in industry, it was imperative that the outer section of the billet was used.

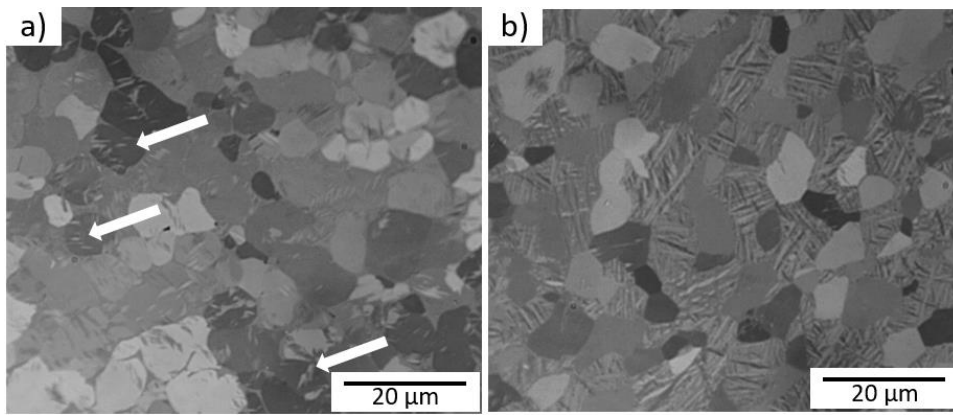


Figure 5.1: Light micrographs of Ti-407, taken from a coupon sectioned from the outer 20 mm of the billet cross section, a) in an as-forged condition, b) after the STA heat treatment.

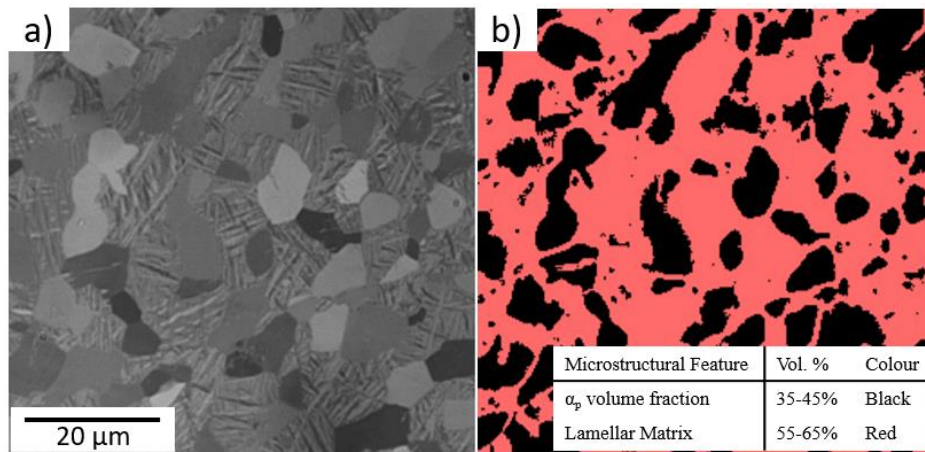


Figure 5.2: a) Light micrograph of Ti-407 at the outer 20 mm of the billet after a STA heat treatment. b) ImageJ contrasting used to ascertain the volume fraction of primary alpha and lamellar within the microstructure of Ti-407.

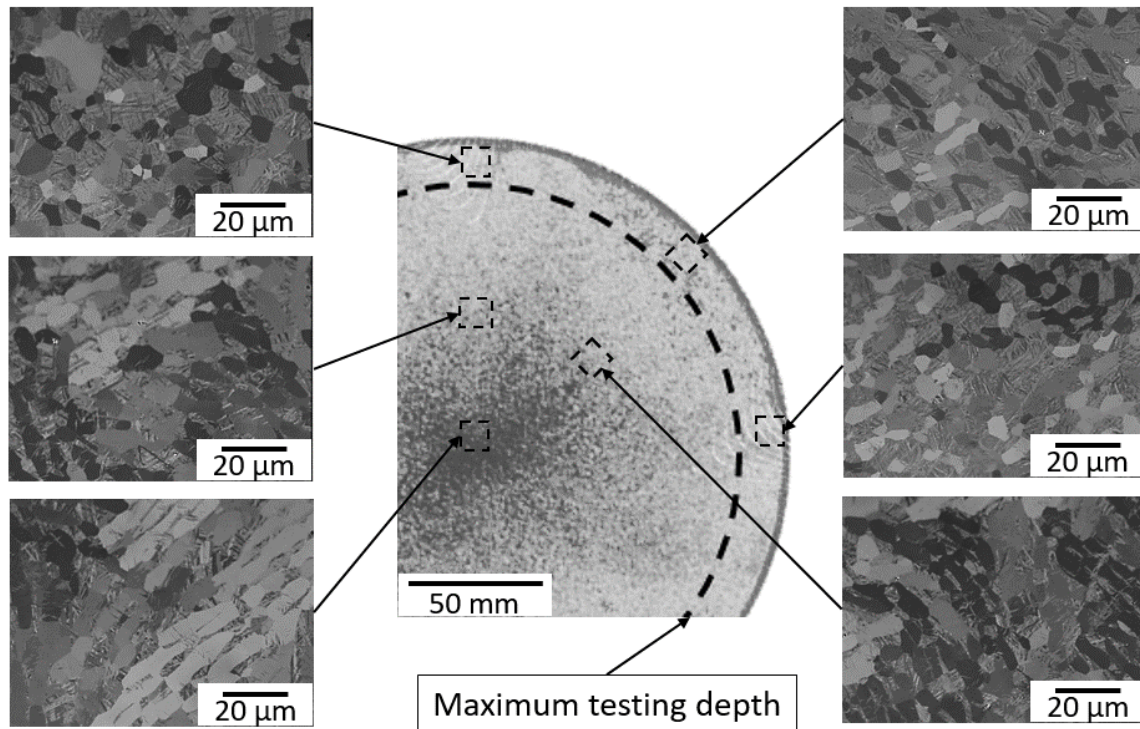


Figure 5.3: Composite image comprising of a quarter cross-section taken of the Ti-407 billet and the corresponding light micrographs at 0° , 45° and 90° .

5.2.2 Experimental setup

Turning trials were conducted on a DMG Mori NLX 2500 CNC machine turning centre at the University of Sheffield's, Advanced Manufacturing Research Centre (AMRC), with a set up shown in Figure 5.4. The billet was held by both the main chuck and a tailstock, for stability. The cutting tools used were Seco LCGF3008M0-0800-RP 883, uncoated inserts. These were held in a Seco CFIR/L2525M08JET tool holder which had been milled down to a shank size of 20 x 20 mm to fit in the Kistler dynamometer, used in this experiment to record the cutting forces. In Figure 5.4 the billet is in a post machining condition to show how the machined surfaces were preserved for further analysis. The test parameters used are shown in Table 5.1: these particular cutting parameters were used as they provided a broad range across the machinability map incorporating regions where it is expected that good chip management could be achieved. Additionally, as the scope of the project was to understand the machining behaviour during a finishing operation, a depth of cut of 0.3 and 0.5 mm was removed from the workpiece. Each test was conducted in one continuous cut for 100 seconds. Finally, Hocut 795b through jet coolant was operated at a pressure of 17 bar which was again employed to best replicate the machining conditions in an industrial set up.

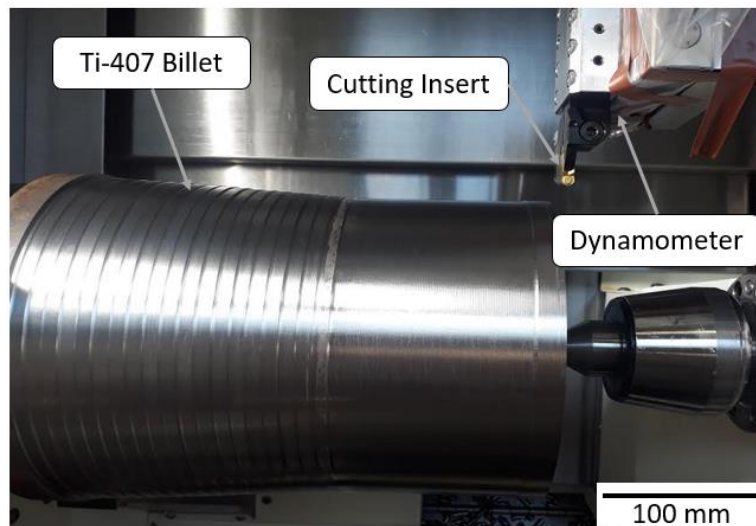


Figure 5.4: Photograph showing the setup for industrial machining trials. Use of a large billet of material held inside a CNC machining centre by chuck and tailstock; the cutting insert and shank held into a Kistler dynamometer to record the cutting forces. The image has been taken after completing all experiments to indicate how the post machining surface analysis samples recorded.

Table 5.1: Table presenting the cutting parameters used to turn Ti-407 STA billet (in Figure 5.4).

Test no.	Depth of cut, mm	Feed Rate, mm.rev ⁻¹	Cutting Speed, m.min ⁻¹
1	0.5	0.6	100
2	0.5	0.6	70
3	0.5	0.6	40
4	0.3	0.4	100
5	0.3	0.8	100
6	0.3	0.4	40
7	0.3	0.8	40

5.3 Experimental Results

5.3.1 Investigating the strain rate effects on the machinability map

The purpose of this experiment was to use the knowledge gained from Chapters 3 and 4 in order to improve the chip control of Ti-407, whilst considering the implications on the overall machinability of the workpiece and tool. The boundary conditions for the map are presented in Table 5.2, which as discussed in the Chapter 4 have been determined from previous experiments conducted on both Ti-407 and Ti-64 as a comparison, which has well established industrial specifications.

Table 5.2: *The boundary conditions set for each factor applied in the machinability model*

	Ti-407
Flank Wear	16 μm
Subsurface Twins	35 μm
Severe Plastic Deformation	70 μm
Chip Morphology	0 (Not Acceptable) → 1 (Acceptable)
Chip Mechanical Twins	0 (No Twins) – 1 (Twins)

The first set of results presented were conducted at a depth of cut of 0.5 mm and their positions on the machinability map have been shown in Figure 5.5, the corresponding results are shown in Table 5.3. All tests were conducted at a feed rate of 0.6 mm.rev⁻¹, and the cutting speed was varied to investigate the effect of strain rate during machining.

Using the machinability map in Figure 5.5, it was predicted that the cutting parameters at data point (3) would provide the best machining output compared to data points (1) and (2), with acceptable chip control and tool wear. However of the three data points, data point (3) would likely exhibit the most excessive amounts of machining induced deformation. Data point (3) was predicted to incur the largest machining induced SPD of the three tests, however the depth of mechanical twins would be the least of all the tests.

Data point (1) was predicted to be the worst for machinability for the reason that it would produce the least controlled chip of all of the tests: it would incur the most tool flank wear and in addition would exceed the acceptable level of mechanical twins in the subsurface. On a positive note, it would incur the lowest depth of SPD of all three tests. The chips were expected to be serrated in morphology, however form a high density of mechanical twins around the adiabatic shear band which would ultimately prevent the frequent breaking of the chips.

Data point (2) was predicted to fail on all accounts of machinability, except for tool wear and the formation of serrated chips. However, these cutting parameters would not be expected to produce a controlled chip due to the risk of formation of mechanical twins around the adiabatic shear band which would negatively affect the breakability of the chip and override any benefits associated with forming a serrated chip. Similar to data point (1), data point (2) should exceed the limit of severe plastic deformation and mechanical twins, however the intensity of SPD was predicted to be between data point (1) and (3).

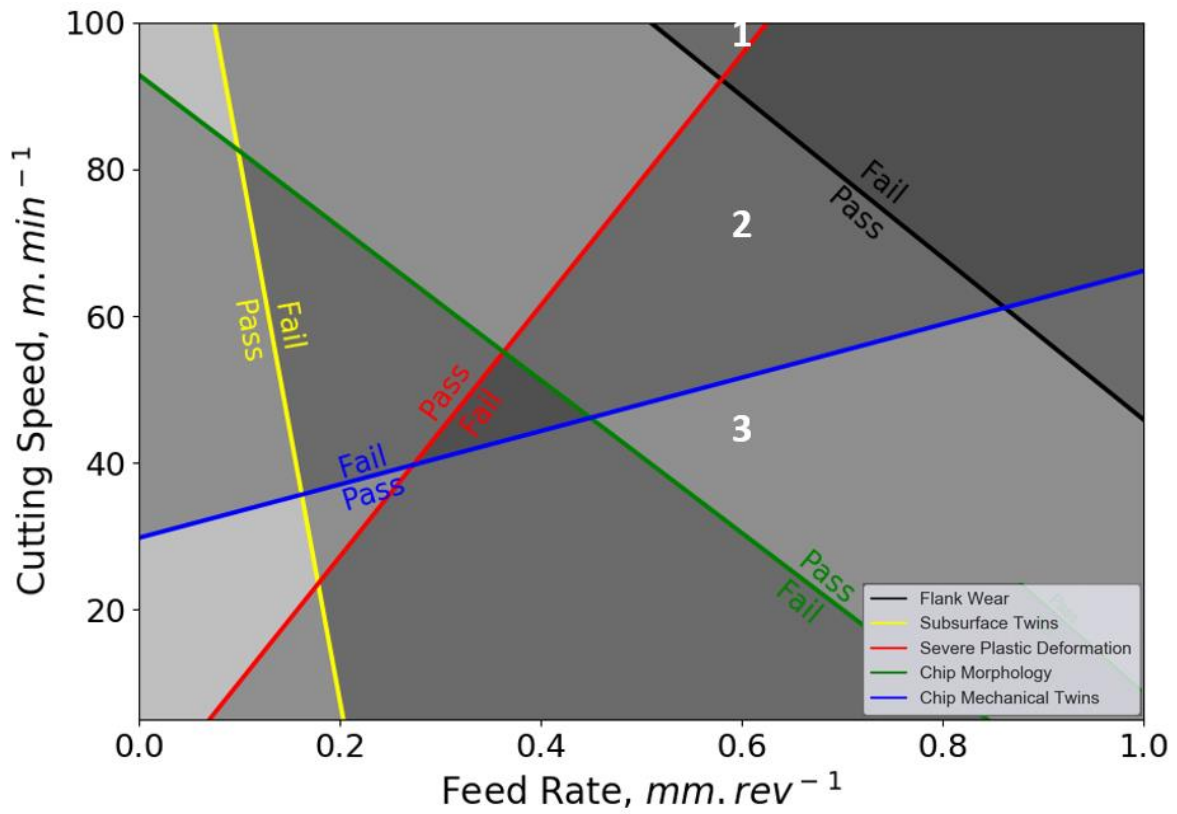
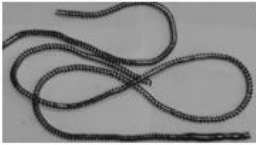
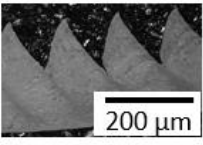
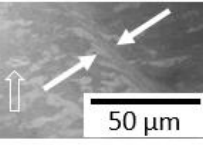
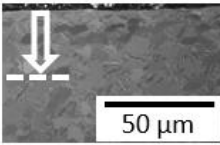
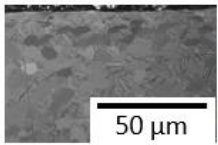
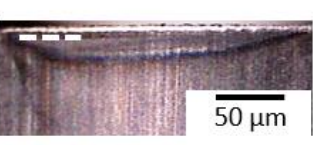
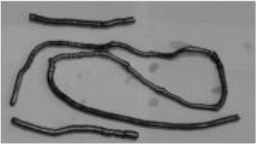
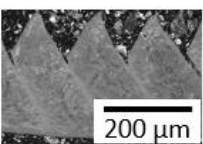
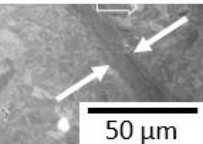
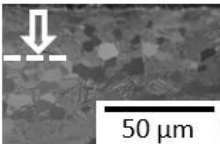
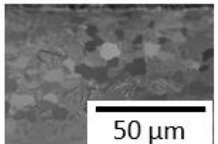
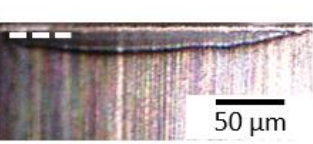
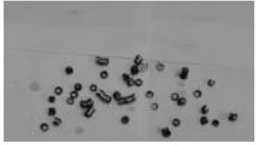
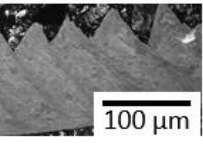
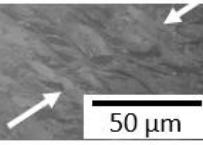
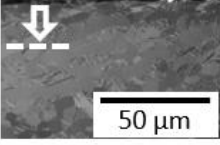
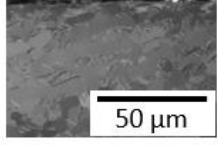


Figure 5.5: Machinability map with the three sets of machining parameters (Table 5.1) conducted at a depth of cut of 0.5 mm. The results have been presented below in Table 5.3.

Table 5.3: Shows the results from the machining trials conducted at a depth of cut of 0.5 mm. The first column shows the chip form resulting from the experiments. The second column shows the chip geometry. The third column shows the adiabatic shear band, with filled white arrows to represent the thickness of the shear band and the unfilled white arrows representing the formation of mechanical twins. Fourth column shows the depth of mechanical twins. The fifth column shows the 3D scans of the tool edge. The sixth column presents the average cutting force and the standard deviation for the test.

	Chip Form	Chip Morphology	Adiabatic Shear Band	Subsurface Mechanical Twins	Severe Plastic Deformation	Tool Flank Wear	Cutting Forces, N	
							Avg.	Std. Dev.
1							289	19
2							462	64
3							317	10

The first column in Table 5.3, shows the chip form produced at each of the points marked on the machinability map in Figure 5.5. Point 1 and 2 form a long chip and point 3 produces short controlled chips. Immediately referring back to the predictions – the experimental results agree entirely. The chips are all of a serrated morphology, as predicted, which is necessary for this alloy to achieve breakable chips. On closer inspection, it is clear from Table 5.3, column 3 that shear localisation is prominent with narrow shear bands forming in between each chip serration. The shear localisation, also known as adiabatic shear bands are highlighted by the solid white arrows. The width of adiabatic shear band increases marginally from approximately 10 μm to 14 μm between the cutting speeds of 100 and 70 $\text{m}\cdot\text{min}^{-1}$, respectively. At 40 $\text{m}\cdot\text{min}^{-1}$ the width of the adiabatic shear band increases to 63 μm . The only difference between data points 1 and 2, and data point 3 is the formation of mechanical twins in the region surrounding the adiabatic shear band, which have been emphasised by the unfilled white arrows. The predictions again agree with the experimental results, with data point 1 and 2 forming mechanical twins - unlike data point 3 which does not. The mechanical twins are seen in this work as a critical component to the deformation characteristics of Ti-407. As has been previously shown by Kloenne et al. [8], the mechanical twins are imperative for accommodating strain during deformation. A high propensity for mechanical twinning provides the alloy with the ductility properties necessary for applications where high fracture toughness resistance is essential. Therefore the presence of mechanical twins around the adiabatic shear band is evidence that greater strain can be accommodated, leading to the inevitable challenging chip management associated with this alloy during machining.

Mechanical twins were identified as a type of machining induced subsurface deformation feature and therefore important to investigate in relation to different cutting parameters and in addition to the twin formation in the chip. To summarise the general trend, increasing the cutting speed led to an increase in the depth of subsurface mechanical twins. At 100 $\text{m}\cdot\text{min}^{-1}$ the measured depth of mechanical twinning was approximately 29 μm , decreasing to 15 μm at the slower speed of 40 $\text{m}\cdot\text{min}^{-1}$. With the subsurface mechanical twin limit set at 35 μm , these cutting parameters are all within the acceptable limits of machining, which is surprising as the expectation was that all the tests would produce undesirable levels of mechanical twins. The relationship between twin formation in the chip and in the machined surface is similar, both increasing with cutting speed. Though in regards to data point 3 it is possible to visually see the twin propagation in the machined surface whilst not so in the adiabatic shear band. Of course given the extreme amount of shear in the adiabatic shear band of the chip it is very difficult to ascertain whether any twins initially formed, however it is clear that if they did form they were isolated to the shear band and did not propagate to the surrounding region of the shear band unlike data points 1 and 2.

This experiment also showed very little machining induced SPD across the three data points, which is promising for industrial machining operations. It was predicted that only data point 1 would

satisfy the boundary conditions, however in reality all three points developed insufficient SPD to fail an inspection.

Of course a number of variables are likely to have played a part in the improvement in subsurface induced deformation including tool geometry, and coolant pressure. Tool geometry has previously been shown by Sharman et al. [9] to influence the level of plastic deformation. When investigating tool geometry edge radius, a smaller radius was found to produce lower depths of plastic deformation than a larger radius insert. This was attributed to a higher cutting edge to cutting thickness ratio, found with larger radius tools which increased the ploughing effect of the tool insert during machining, leading to greater plastic deformation. The cutting insert in Chapter 4 was a 4 mm flat edge, therefore of infinite radius, whereas in this experiment the cutting radius was 4 mm, however due to the curvature of the insert, the tool would have engaged sizeably less material. Therefore comparatively the edge of the insert in Chapter 4 would have generated a lot of ploughing. Coolant pressure has also been found to play a role in the subsurface induced deformation. Ezugwu [10] was able to show that the use of conventional flood coolant methods hardened the machined surface unlike high pressure coolant which did not.

Tool flank wear was measured for each of the tests to be less than the 16 μm , which was the determined boundary limit used in the machinability model. This limit was set on the basis of a continual turning operation requiring the tool to last in excess of 15 minutes without exceeding an average flank wear limit of 250 μm . Data point 1 predicted the greatest tool flank wear of the three tests, measured at 5 μm , compared to data point 2 and 3, which had negligible tool wear. Given the tests were 100 seconds, this suggests that the tools would survive a 15 minute continual machining operation at any of these parameters used. The machinability model assumed that the greatest tool wear would be achieved with data point 1 and the lowest tool wear for data point 3, suggesting that increasing the cutting speed directly correlates with an increase in tool flank wear rate and a shortening of the tool life.

The effect of cutting speed on cutting forces was not consistent from low to high cutting speeds. The average cutting force decreased between 70 $\text{m}\cdot\text{min}^{-1}$ and 100 $\text{m}\cdot\text{min}^{-1}$ from 617 N to 549 N respectively. However, the average cutting force increased between 40 $\text{m}\cdot\text{min}^{-1}$ and 70 $\text{m}\cdot\text{min}^{-1}$ from 577 N to 617 N. It has been well established that the cutting forces typically reduce as cutting speed increases due to the material softening and the chip thickness decreasing [11]. However in excess of speeds of 100 $\text{m}\cdot\text{min}^{-1}$ it has been found that the cutting forces can increase during the machining of titanium alloys [12]. The reason for the highest cutting forces of 617 N occurring at 70 $\text{m}\cdot\text{min}^{-1}$ cannot be explained by the author at this time. The standard deviation was calculated for each of the tests. The standard deviation relates to the serrated chip characteristics. A standard deviation of 66 N was calculated at the higher cutting speed of 100 $\text{m}\cdot\text{min}^{-1}$ whereas at 40 $\text{m}\cdot\text{min}^{-1}$ this was only 31 N. The relationship between tool fracture and chip serration is also well known. Chip serration has been linked,

to cyclic cutting forces, and furthermore to premature tool failure [13]–[15], therefore the lower standard deviation at $40 \text{ m}\cdot\text{min}^{-1}$ is beneficial for the overall tool life, both by reducing the range of the cyclic peaks in the cutting forces- which can lead to chip fracture, but by also lowering the tool tip temperature from machining at lower cutting speeds- which will help minimise diffusion wear and plastic deformation.

5.3.2 Validating the machinability map at a depth of cut of 0.3 mm

The second set of results presented were conducted at a depth of cut of 0.3 mm and their positions on the machinability map have been shown in Figure 5.6, the corresponding results are shown in Table 5.4. From the machinability map, it was predicted that either data point 4 or data point 7 would be the best set of conditions for machinability, followed by data point 6 then data point 5.

In terms of chip control it was predicted that data point 7 would produce chips that would have a good serrated morphology and no mechanical twins forming around the ASB. It would exhibit acceptable amounts of tool flank wear, but would incur excessive subsurface mechanical twins and the greatest depth of machining induced SPD of the data points used in this experiment.

Data point 4, similar to data point 7 was expected to induce low tool wear, however unlike data point 7 would not produce excessive machining induced SPD. These test parameters would fail to produce a good chips for handling due to the prominence of mechanical twins around the ASB and the amount of twins in the machined surface would also be excessive.

Data point 5 would form a promising chip morphology with serrated chips, however again mechanical twins which in the ASB would affect chip breakability. This data point was projected to exceed the tool wear limit, obtaining the most tool flank wear of the data points used in this experiment and would experience excessive deformation in the machined surface both through SPD as well as sustaining the largest depth of mechanical twins of all the data points.

Finally data point 6, which was predicted to produce the least controllable chips for two reasons: firstly it would form a chip in constant uniform shear and secondly would also generate mechanical twins in the chip. The parameters would generate too much machining induced SPD and mechanical twins in the machined surface. The only machinability characteristic that was predicted to be acceptable was the tool flank wear which should be the lowest of all of the tests conducted.

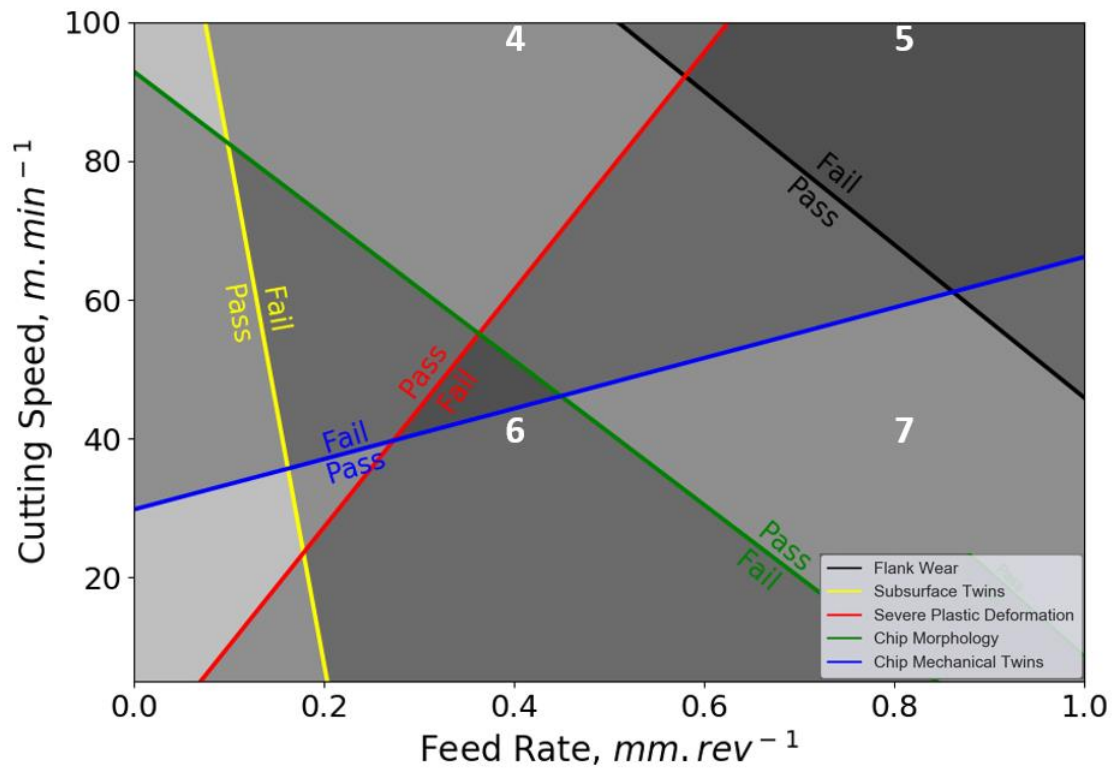


Figure 5.6: Shows the machinability map with the four points where machining experiments were conducted at a depth of cut of 0.3 mm. The results have been presented below in Table 5.4.

Table 5.4: Shows the results from the machining trials conducted at a depth of cut of 0.3 mm. The first column shows the chip form resulting from the experiments. The second column shows the chip geometry. The third column shows the adiabatic shear band, with filled white arrows to represent the thickness of the shear band and the unfilled white arrows representing the formation of mechanical twins. Fourth column shows the depth of mechanical twins. The fifth column shows the 3D scans of the tool edge. The sixth column presents the average cutting force and the standard deviation for the test.

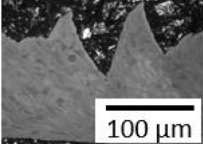
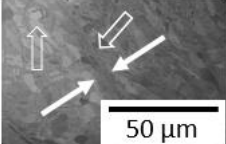
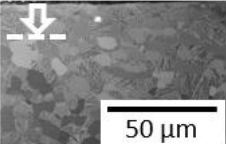
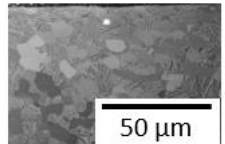
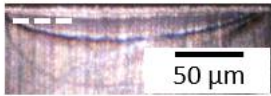
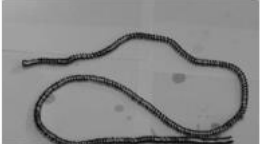
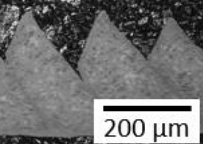
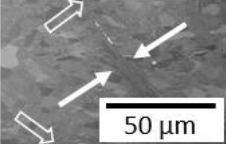
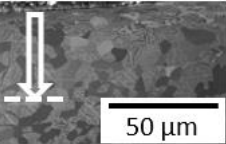
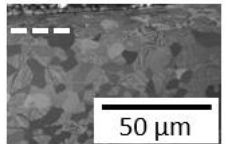
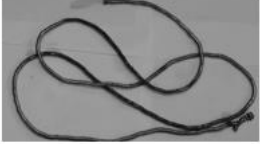
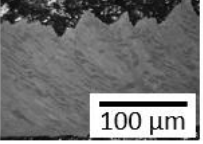
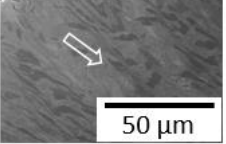
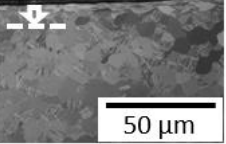
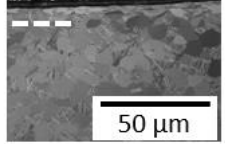
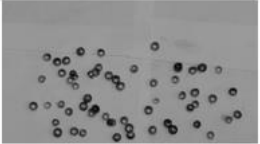
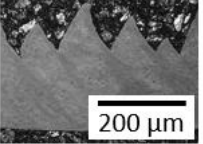
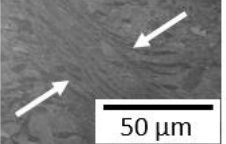
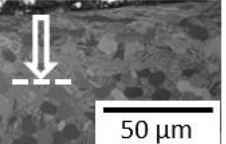
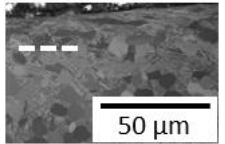
	Chip Form	Chip Morphology	Adiabatic Shear Band	Subsurface Mechanical Twins	Severe Plastic Deformation	Tool Flank Wear	Cutting Forces, N	
							Avg.	Std. Dev.
4							289	19
5							462	64
6							317	10
7							515	26

Figure 5.6 and Table 5.4 show the results for the tests conducted at a depth of cut of 0.3 mm.

The prediction of the chip form, was that data point 6 would produce the least controllable chip type and data point 7 would produce the most controllable chip type. From Table 5.4 it is clear that data point 6 forms the longest chips, which has been shown to be the effect of the near constant uniform shear across the chip- shown in column 2, and the prominence of mechanical twins within the chips- shown in column 3. Contrary to this, data point 7 as expected, produced the ideal chip form, i.e. short and controlled, forming serrated chips with no observable mechanical twins. Data point 4 and 5 both struggled to form short manageable chips given the prominence of mechanical twins around the ASB, despite the visible shear localisation. Again this underpins the importance of choosing parameters that do not form mechanical twins for the purpose of good chip management.

In relation to the subsurface mechanical twins, machining at data point 5, resulted in the greatest depth of mechanical twins of all the tests at 39 μm , whereas the cutting parameters of data point 6 caused the smallest depth of mechanical twins to form at 5 μm . The machinability map was able to correctly predict and identify the order of increasing depth of mechanical twins between the data points, however only correctly predicted data point 5 as failing to meet the 35 μm limit.

The results for the machining induced SPD in the machined surface, again referring to the machinability map, are correctly assigned for only data point 4. Data point 4 shows negligible SPD in the machined surface in agreement with the machinability map, whereas data point 7 which was expected to exceed the limit of SPD by the most only produced 10 μm of SPD, well within the 70 μm limit set by the boundary conditions. There is very little difference between the depth of SPD for data points 5 and 6, with only 4 μm of deformation to the machined surface. It is perhaps unsurprising that there is so little to differentiate these two data points as they run almost parallel to the red “Severe Plastic Deformation” line in Figure 5.6, and so would be expected to produce similar depths of deformation.

The results show that the average tool flank wear was highest for data points 4 and 5, which measured flank wear of 8 μm and 9 μm respectively. The machinability map predicts that data point 5 would exceed the 16 μm limit, however this is not the case. Data points 6 and 7 measured the lowest tool flank wear of less than 5 μm . Similar to the results in Table 5.3, the cutting parameters would be adequate for a continual turning operation of 15 minutes.

Looking across to the cutting forces in Table 5.4, increasing the cutting speed reduced the average cutting forces, both as a result of thinning chips and the increased material softening effects. Additionally, the increasing cutting speed increased the standard deviation, which as discussed previously in Chapter 4.1 is directly related to the cyclic nature of the serrated chips which can lead to premature tool failure. Importantly, the standard deviation is not the highest for the most controlled

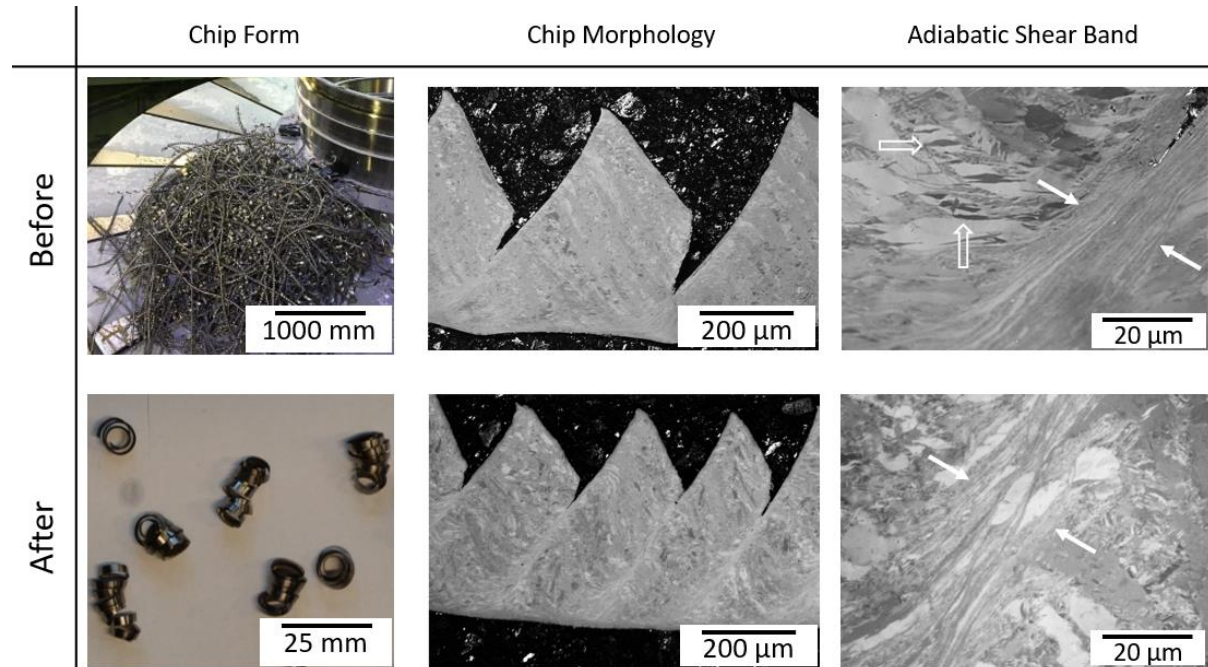
chips, which demonstrates that whilst serrated chips are imperative for good chip control, ensuring the cutting parameters do not exceed the boundary conditions of the mechanical twins is just as important. Control of chip formation can be accomplished with minimal cyclic force fluctuations, helping to extend the life of the tool.

These results demonstrate two things; firstly that regardless of the machining setup, the general material machinability trends revealed in this map are accurate and predictable, i.e. parameters can be best selected, to target improvements to specific factors of machinability. Secondly Ti-407 is an alloy which can be machined in an optimal region where all of the factors of machinability are acceptable.

5.3.3 Industrial outputs of this work

Table 5.5 shows the industrial output of this research, through the comparison of the chip control before and after this study began. There has been a great improvement in the chip breakability, reducing the chip length from in excess of 2 metres down to less than 20 mm. Understanding that the cause of the chip related problems was the proliferation of mechanical twins, allowing further accommodation of strain, ultimately delaying chip fracture, made it possible to make corrective measures to the cutting parameters to improve the chip control whilst simultaneously managing the other aspects of machinability. Through managing the chip form, it was also possible to reduce the machining time of these components by 43% during finishing operations by increasing the feed rate and allowing only a slight reduction in cutting speed resulting in significant cost and time savings for industry. The improvements to the chip management was responsible for also reducing cleaning downtime between parts and reducing required maintenance to fix issues with the chip swarf conveyor. The overall risks associated with component rework due to tool breakage or surface finish defects have been reduced, offering potential savings of 300 minutes per part for ‘on machine’ rework, or 480 minutes per part for ‘hand dressing’ by an operator. Due to these operational improvements, the flow of parts through manufacturing facilities has been improved, reducing inventory stock and work in progress.

Table 5.5: Series of photographs and micrographs of the chips before and after the completion of this PhD. The filled white arrows in c) and f) are indicating the width of the shear bands. The unfilled white arrows in c) are pointing to the formation of the mechanical twins surrounding adiabatic shear band



5.5 Conclusions

This chapter has been used to validate the development of the machinability map utilising a machining arrangement closely resembling that of industrial machining operations. This has led to the appreciation that a number of variables affect the accuracy of the map, however that the general trends are strongly related to material properties and so exist despite differences to the machining set up. It is therefore possible to use the machinability map to inform a machining operator prior to machining of a titanium alloy of the most important fundamental factors affecting machining outputs and encourage quick and efficient selection of parameters to increase productivity of components. The outputs of this work led to improvements to the chip management for industrial machine finishing operations and a 43% reduction of machining time.

References

- [1] M. Thomas, S. Turner, and M. Jackson, "Microstructural damage during high-speed milling of titanium alloys," *Scr. Mater.*, vol. 62, no. 5, pp. 250–253, 2010.
- [2] A. J. Makadia and J. I. Nanavati, "Optimisation of machining parameters for turning operations based on response surface methodology," *Measurement*, vol. 46, no. 4, pp. 1521–1529, 2013.
- [3] G. E. P. Box and K. B. Wilson, "On the Experimental Attainment of Optimum Conditions," *J. R. Stat. Soc. Ser. B*, vol. 13, no. 1, pp. 1–38, Jan. 1951.
- [4] N. C. Tsourveloudis, "Predictive Modeling of the Ti6Al4V Alloy Surface Roughness," *J. Intell. Robot. Syst.*, vol. 60, no. 3–4, pp. 513–530, Dec. 2010.
- [5] M. Nalbant, H. Gökkaya, and G. Sur, "Application of Taguchi method in the optimization of cutting parameters for surface roughness in turning," *Mater. Des.* vol. 28, no. 4, pp. 1379–1385, Jan. 2007.
- [6] J. Ribeiro, H. Lopes, L. Queijo, and D. Figueiredo, "Optimization of Cutting Parameters to Minimize the Surface Roughness in the End Milling Process Using the Taguchi Method," *Period. Polytech. Mech. Eng.*, vol. 61, no. 1, pp. 30–35, 2017.
- [7] L. B. Abhang and M. Hameedullah, "Optimization of Machining Parameters in Steel Turning Operation by Taguchi Method," *Procedia Eng.*, vol. 38, pp. 40–48, 2012.
- [8] Z. Kloenne, G. Viswanathan, M. Thomas, M. Loretto, and H. Fraser, "A Comparative Study on the Substructure Evolution and Mechanical Properties of TIMETAL 407 and Ti-64," in *The 14th World Conference on Titanium Proceedings*, 2019, pp. 1–6.
- [9] A. R. C. Sharman, J. I. Hughes, and K. Ridgway, "The effect of tool nose radius on surface integrity and residual stresses when turning Inconel 718TM," *J. Mater. Process. Technol.*, vol. 216, pp. 123–132, 2015.
- [10] E. O. Ezugwu, J. Bonney, R. B. Da Silva, and O. Çakir, "Surface integrity of finished turned Ti–6Al–4V alloy with PCD tools using conventional and high pressure coolant supplies," *Int. J. Mach. Tools Manuf.*, vol. 47, no. 6, pp. 884–891, 2007.
- [11] T. Childs, "Metal Machining Theory and Applications," *Mater. Technol.*, pp. 1–19, 2000.
- [12] J. Hou, W. Zhou, H. Duan, G. Yang, H. Xu, and N. Zhao, "Influence of cutting speed on cutting force, flank temperature, and tool wear in end milling of Ti-6Al-4V alloy," *Int. J. Adv. Manuf. Technol.*, vol. 70, no. 9–12, pp. 1835–1845, Feb. 2014.

- [13] E. O. Ezugwu and Z. M. Wang, "Titanium alloys and their machinability—a review," *J. Mater. Process. Technol.*, vol. 68, no. 3, pp. 262–274, Aug. 1997.
- [14] S. Zhang, J. Li, X. Zhu, and H. Lv, "Saw-tooth chip formation and its effect on cutting force fluctuation in turning of Inconel 718," *Int. J. Precis. Eng. Manuf.*, vol. 14, no. 6, pp. 957–963, Jun. 2013.
- [15] C. Gao and L. Zhang, "Effect of cutting conditions on the serrated chip formation in high-speed machining," *Mach. Sci. Technol.*, vol. 17, no. 1, pp. 26–40, Jan. 2013.

Summary and Future Work

6.1 Summary

This research project was undertaken to develop a low-cost methodology to predict the machining performance of emerging titanium alloys, and secondly to provide an explanation for the poor chip control for emerging alloy Ti-407 and how to improve it. The machining performance of Ti-407 was compared against Ti-64, which has long been considered as the workhorse alloy, as it is used for a broad range of applications. Both Ti-407 and Ti-64 are $\alpha+\beta$ type alloys which give them a good balance of strength and ductility necessary for applications in aerospace engines. Ti-407 was developed to replace Ti-64 in applications where energy absorption during fracture is important, such as large structural gas turbine engine components. The machinability of both alloys were compared based on the key attributes including: tool wear, chip formation, subsurface integrity and cutting forces. The combination of complementary experimental and modelling techniques proved successful in characterising the machinability of these two alloys and providing a fundamental understanding for the poor chip control of Ti-407. A summary of the key findings in this thesis have been split into two sections, each relating to the separate outcomes of this thesis.

The first section of this research looked at developing the small scale methodology to predict machining performance:

- The uniaxial compression test proved effective at screening titanium alloy compositions and heat treatment conditions at an early stage prior to expensive, large scale machinability trials. From a simple uniaxial compression test the chip form, subsurface damage and cutting force were directly characterised. From the stress-strain data, the area under the curve informed on the required energy to cause fracture for different alloys. Mechanical properties were extracted from the stress-strain curve, with the maximum stress relating to the resistance to deformation and the ease of forming a chip. Ti-64 produced higher stresses during the compression test, which showed that resistance to deformation was higher and as such the chip forming process was more force intensive. The ductility was extracted from the maximum strain achieved prior to fracture. The strain accommodation in Ti-407 during compression testing was significantly greater than Ti-64. This has previously been shown to make chip breakage more difficult to achieve and require higher feed rates and lower cutting speeds to aid chip breakage. The regions

of high strain in the compressed samples were analysed using microscopy techniques to understand the deformation mechanisms of each alloy, which again provided information on the chip forming characteristics of the titanium alloy. From the uniaxial compression test, it was found that Ti-64 forms narrow intense shear bands, whereas Ti-407 forms wider less intense shear bands. This is hypothesized due to Ti-407's greater thermal conductivity, which allows more heat to be dissipated and reduces the localised effects of thermal softening and work hardening.

- The stress-strain data from the compression test was inputted into DEFORMTM in order to model the chip forming process. The chip geometry was one metric for determining the chip breakability and was compared for both alloys. It was evident that Ti-64 easily formed a serrated chip whereas Ti-407 formed a chip of constant uniform shear. Chips in constant uniform shear were determined as problematic for chip breakability as the absence of thermoplastic instability hindered formation of ASBs resulting in long nested chips. Therefore, higher cutting speeds would have to be applied during the machining of Ti-407 in comparison to Ti-64, in order to produce serrated chips. In addition to chip geometry, the strain induced surface damage was also analysed, and showed that greater strain, to a greater depth was measured in Ti-407. Strain in a machined surface manifests as severe plastic deformation, which can have an effect on the longevity of the component. It is therefore necessary to consider the cutting parameters carefully so not to induce too much strain into the machined surface.
- A novel low-cost orthogonal testing approach utilising the Arbitrary Strain Path test rig was developed to investigate the machinability of small samples of titanium alloys. The samples would be lowered toward a cutting insert to create an orthogonal cut. Development of the orthogonal cutting rig led to drastic improvements to the accuracy and reliability of the testing compared to previous work, through designing a single sided tool holder and test piece which reduced the load and lateral movement of the tool and workpiece during the cutting.
- Small scale orthogonal cutting experiments revealed key machining characteristics of each material and agreed with data from the simple uniaxial compression test. The results showed that both alloys exhibited strengths and weaknesses when considering machinability from both a tooling and workpiece perspective. The Ti-407 produced chips more closely related to a continuous chip in constant uniform shear, whereas the Ti-64 produced serrated chips with narrow regions of localised shear - regarded as beneficial for chip breakage. Ti-407 shows better machinability when analysing tool wear and cutting forces, which validates the compression test data.

- Quantification of the twin volume density in a material can be validated from the work hardening rate curve. The normalised work hardening rate curve showed that Ti-407 has a greater saturation of mechanical twins during deformation than Ti-64.

As well as developing the low cost methodology to predict machining performance, high speed machining trials were completed to understand the issue of the poor chip control during the machining of Ti-407 and how this can be improved. The key findings from this section of work are summarised below:

- Poor chip control is due to two main conflicting mechanisms. Firstly is the insufficient thermoplastic instability, and secondly is the prevalence of mechanical twins. The reason these mechanisms are conflicting is because to induce thermoplastic instability, greater cutting speeds for a given feed rate must be used; to reduce the prevalence of mechanical twins, lower cutting speeds for a given feed rate must be utilised. Increasing the feed rate is the only effective practice for improving chip breakability of a titanium alloy. However this comes with issues of poor surface integrity, greater stress on the tool and higher cutting forces.
- Due to the thermal conductivity of Ti-407 the minimum cutting speed where the chip form transitions from a continuous chip to serrated chip is higher than Ti-64. In the tests that were conducted this transition did not occur until the cutting speed exceeded $40 \text{ m}\cdot\text{min}^{-1}$ at a feed rate of $0.3 \text{ m}\cdot\text{min}^{-1}$. The greater thermal conductivity allows more heat to dissipate, reducing the effect of heat localisation on the dominance of thermal softening and work hardening that is characteristic of titanium machining.
- Mechanical twins have been identified to form in and around the adiabatic shear band of the chip. Formation of twins is detrimental to the chip breakability as they increase the strain accommodation in the chip.
- Due to the low aluminium content of Ti-407 (0.85 wt. %) the alloy has a propensity to form deformation twins during machining both in the machined surface and in the chip. Twins in Ti-64 are less likely to form due to the increased ordering from the aluminium additions, however this work rejects early claims that twins do not form in titanium alloys with aluminium content of greater than 6 wt.%.

The overall industrial output was a 43% reduction in the machining time of large structural gas turbine engine components by moving to Ti-407 instead of Ti-64 as the alloy of choice for this application, which was complemented by a great improvement in chip management. The improved chip management led to a number of further benefits to the industrial partners in the form of reduced downtime for machine cleaning and maintenance, in addition to reduced risk of component rework due to tool breakage and surface finish defects.

6.2 Future Work

This research has developed the knowledge in machining titanium alloys through the development of the small scale machinability approaches discussed in Chapter 3, as well as a better understanding of the deformation characteristics of titanium alloys and how to apply this knowledge to an industrial application. Though there are key areas where further development should be focussed to maximise the potential of the results in this work.

Firstly, the range of alloys utilised in this work was limited, exploring only Ti-64 and Ti-407. To take advantage of the low cost machinability methodology as a future early stage predictor of machining performance, it is advised that a wider survey of alloys and materials (Inconel, Steel and Aluminium) should be tested to ensure adequate stress testing has been completed. It is suggested that repeats be conducted for tests in future to ensure validity of results and to rule out any discrepancies between tests. For future work using the uniaxial compression test, it is recommended that development of the technique be focussed around increasing data recording frequency. Due to the limited data recording frequency it was not possible to accurately or reliably gather data at high strain rates of 100 s^{-1} and higher. It would be advantageous to have greater resolution at high strain rates when comparing results to high strain rate environments such as machining. Equally it is known that microstructural variations have a great bearing on the machining performance. There is very little understood about the broader effects of microstructures on machinability. Certain questions surrounding why the oil quenched Ti-407 workpiece did not follow the expected pattern, are not yet understood. Both further testing of the different microstructures are necessary and further analysis of the material in relating to textural analysis and material properties would be valuable in answering some of these questions.

The machinability map has joined the effects of machining outputs from a narrow range of cutting parameters. Further testing is required to become a more comprehensive guide to optimising machining output. To create the machinability map only six data points were utilised. Although the trends within this work were strong, it was clear that a greater number of data points would help strengthen the machinability maps reliability. Further to this, the research only focussed on a small array of machining outputs. Subsurface deformation was merely split into two categories: severe plastic deformation and mechanical twinning. It is well acknowledged that other possible variables such as white layer and residual stress can have a grave effect on the potential longevity of a component and must either be limited or removed entirely. In this case extending the bounds of analysis to incorporate other factors would provide greater confidence in the key regions of a machinability map which are considered “optimal” for machining.

With these machinability maps further collaborations would be recommended between members of the supply chain including, tool manufacturers, materials suppliers and machining end-users to investigate the effects of tool coatings, geometries, chip-breakers and compositions to gain an understanding for the specific machinability nuances of the materials when exposed to different cutting tool variations.

Additional mechanical testing would be recommended by the author to assess the effects of machining optimisation and surface condition on fatigue performance, i.e. what are the effects of machining on the HCF and LCF properties of a material?

The future work focusses on stress testing the small scale machinability techniques and the robustness of the machinability map to improve confidence and enhance the commercial potential in this work. This work and any follow on research will support the long term goals of: 1) reducing the time to market for future titanium alloys through efficient and effective small scale machinability assessments, 2) identification of the optimal cutting parameters for current and future alloys through the use of machinability maps, as well as 3) assessing the effects of machining on the fatigue performance of the materials.